CONDENSATION AND MOBILITY STUDIES OF FLUID INTERFACES

Paul L. Barclay

A DISSERTATION

in

Mechanical Engineering and Applied Mechanics

Presented to the Faculties of the University of Pennsylvania

in

Partial Fulfillment of the Requirements for the

Degree of Doctor of Philosophy

2018

Supervisor of Dissertation:

_____

Dr. Jennifer R. Lukes
Professor, Mechanical Engineering and Applied Mechanics

Graduate Group Chairperson:

_____

Dr. Kevin Turner
Professor, Mechanical Engineering and Applied Mechanics

Dissertation Committee:

Dr. Portonovo S. Ayyaswamy, Asa Whitney Professor of Dynamical Engineering, Mechanical Engineering and Applied Mechanics
Dr. John L. Bassani, Richard H. and S. L. Gabel Professor, Mechanical Engineering and Applied Mechanics
Dr. Ravi Radhakrishnan, Professor, Bioengineering

For my dad, mom, brother, and sisters.

Acknowledgements

First, I would like to thank my advisor Professor Jennifer R. Lukes for her guidance, support, and encouragement. Her energetic attitude toward research kept me motivated throughout my entire dissertation. I have learned a lot from her and am grateful to have been one of her students. I would also like to thank Professors Portonovo S. Ayyaswamy, John L. Bassani, and Ravi Radhakrishnan for taking time and care to serve on my dissertation committee. Their discussions, guidance, and advice have been thought provoking and have had a positive impact on this dissertation.

I am very thankful for my research group and office mates, both past and present: Ruiyuan Ma, Joseph Cooke, Ian Cosden, Mehdi Zanjani, Drew Cheney, Yuejun Yan, Jin Xu, Masahiro Narasaki, Jake Floyd, and Rossiny Beaucejour. I have learned a lot from each of you, and you have had a positive impact on my experience at Penn. I would also like to thank the department staff being ever willing to help with any requests I made, specifically Peter Litt, Maryeileen Banford Griffith, and Sue Waddington-Pilder.

I would like to acknowledge the funding and computational resources that made this work possible in part from the Department of Education and the National Science Foundation's XSEDE computing environment.

Finally and most importantly, I would like to extend my sincerest thanks and gratitude toward my family and friends. Your support and encouragement for me through the whole process has helped motivate me, and I would not be where I am today without you. Thank you for all the enjoyable times, keeping me sane, and helping me de-stress while working toward my degree.

ABSTRACT

CONDENSATION AND MOBILITY STUDIES OF FLUID INTERFACES

Paul L. Barclay

Jennifer R. Lukes

Condensation is of central importance in a broad range of areas in nature and industry. Aerosol-cloud interactions, a currently a significant open question in climate modeling, and water harvesting mechanisms on organisms such as cacti, beetles, and spiders, are natural processes that are rely on condensation. Condensation is an effective method for transferring heat due to the latent heat required for a fluid to change phase from a gas to a liquid. Improvements in condensation processes would have an impact in a variety of industrial areas such as thermal management, environmental control, microelectronics, desalination, and power generation. Dropwise condensation is preferable over filmwise condensation because it has a significantly higher heat transfer coefficient. Nanopatterned surfaces are of interest because they have experimentally demonstrated higher heat transfer than their smooth counterparts, but recent heat transfer measurements on individual droplets have revealed discrepancies between theoretical predictions and experimental measurements for the smallest droplets. Interfacial properties on small length scales are often difficult to measure experimentally and are often used as fitting parameters in condensation models. The common assumptions used when modeling dropwise condensation are that (1) the condensing droplets are thermodynamically quasi-static and that (2) the heat and mass transport are uncoupled, that is, droplet motion and heat transfer are modeled independently of one another. In this dissertation, several continuum properties including the mass accommodation coefficient and interfacial mobility are

computed allowing for the physical parameters to be known *a priori* for continuum scale models such as the Navier-Stokes-Cahn-Hilliard equations or interfacial resistances in condensation models. Furthermore, the two fundamental assumptions used in condensation models are examined in an attempt to resolve the theoretical and experimental discrepancies. This will be done by leveraging microscopic and non-equilibrium thermodynamic approaches to determine the validity of the condensation assumptions for planar and highly curved systems.

Contents

List of Tables

List of Figures

xvi

xviii

1   Introduction

Much work has been performed over the past several years investigating fluid flow and heat transfer at the micro- and nano-scale. Improvements due to these studies have touched a variety of fields ranging from robotics to biotechnology, mainly due to the impact of fluid flow and heat transfer in devices and processes ranging from nanosensors to desalination [5–19]. Consequently the decreasing sizes of these devices further increases the importance of heat transfer due to the higher heat fluxes in modern devices. Heat fluxes in these devices reach almost 10^7W/m^2 [20] and are expected to exceed these values in the near future [21]. Effective methods to remove this heat are needed, and phase change heat transfer offers an alternative to standard conduction or convective heat transfer as phase change heat transfer may be capable of meeting the predicted demand. Latent heat is the key to unlocking the higher heat transfer coefficients of phase change methods due to the energy required for a fluid to transition between the liquid and vapor phases [22]. Engineering and further improving these devices and processes will require having a complete understanding of the heat and mass transfer as well as the fluid motion in order to allow for better thermal management to meet the expected thermal demands [5, 6, 21].

Many industrial processes utilize condensation such as thermal management [23, 24] where a condenser is used to reject heat, desalination [19, 25] where condensation is used to produce purified water, environmental control [26, 27] where condensation removes excess or unwanted water vapor from surrounding air, and power generation [28–30] where heat is rejected at low temperature causing the working fluid to condense. Knowing and having complete understanding about condensation is crucial in heating and air conditioning systems, which account for approximately one fifth of the energy consumption in developed nations [23]. If unwanted condensa-

tion occurs in turbines it can cause mechanical damage [30], and condensation within buildings can lead to dampness and mold if humidity is not properly controlled which negatively effect the health of occupants [27]. Main avenues for condensation are filmwise condensation where a liquid layer condenses across the entire condensing surface and dropwise condensation where condensation occurs at individual locations forming drops of various sizes on the condensing surface. In dropwise condensation the heat transfer coefficient is significantly higher (often more than 10 times greater) than filmwise condensation due to the thermal barrier created by the condensed film in filmwise condensation [22]. Still most practical applications assume or use filmwise condensation because it is difficult to maintain hydrophobic (nonwetting conditions) for an extended period of time because drops are not able to efficiently be removed from the condensing surface and eventually flood the surface causing a transition to filmwise condensation.

A recent study by Miljkovic *et al.* [31] has shown a six fold increase in the heat transfer coefficient due to nano- and micro-patterned surfaces sparking interest in modeling condensation on these surfaces [31–34]. With surface patterning the heat transfer is enhanced because it makes the surfaces superhydrophobic, enabling dropwise condensation instead of filmwise condensation, and enables reduced droplet sizes relative to those found on flat surfaces causing increased fluxes because small droplets have higher heat transfer compared with larger droplets [35]. Even more exciting is the possibility that these surfaces may be designed to prevent the onset of surface flooding allowing for the more effective dropwise condensation to potentially be used in industrial applications. Several experimental and theoretical studies have been performed examining dropwise condensation [31, 32, 34–41], but the theoretical and experimental results only agree for droplets with radii larger than roughly $10\mu m$

[31, 32]. On these small length scales, the surface features further complicate the studies of the early stages of droplet growth [31–35, 41] due to the frequent switching between constant contact angle (CCA) growth and constant base (CB) area growth. Most commonly CCA growth is assumed for droplet growth where the contact angle of the drops remains constant as the droplet grows while CB growth occurs when the triple line, the location where the liquid-vapor interface meets the surface, is pinned due to a surface feature such as a pillar edge or defect. Effective use of surface patterning to prevent the transition from dropwise to filmwise condensation has the potential to obtain the expected heat fluxes of future devices but will require a robust understanding of dropwise condensation and droplet motion on small length scales.

2 Literature Review and Modeling Approaches

2.1 Modeling Overview

When modeling dropwise condensation two main avenues exist; one for capturing heat transfer and the other for capturing motion, growth, transition (constant contact angle to constant base area or vice versa), and coalescence. Quasi-static models are employed for capturing heat transfer while multiphase Navier-Stokes equations are solved to study fluid motion. The majority of work in this area decouples the heat transfer and droplet motion [31,33–69] ignoring any transient effects from growth, transition, or internal fluid motion on thermal transport. This may be valid for large slowly growing drops but may not hold for small rapidly growing drops. The theoretical predictions and experimental measurements differ at radii below 10 μm [31,32], bringing into question the validity of these models at small length scales. The aim of this chapter is to explain the commonly used models and highlight some of the key assumptions made.

2.2 Quasi-static Heat Transfer Models

A first approach to model condensed droplet heat transfer can be done with a thermal resistor network for an individual droplet as shown in Fig. 2.1. The heat transfer through an individual droplet, $\dot{Q}_D$, is given by

$$\dot{Q}_D = \frac{\Delta T}{R_{total}} \tag{2.1}$$

where ΔT is the temperature drop from the surrounding vapor to the surface and R_{total} is the equivalent resistance from the resistor network. A very simple resistor

network is shown in Fig. 2.1, where the individual resistances depend on both physical properties and the geometry of the system. These networks can be modified to include geometric effect due to nano- or micro-pillars, hydrophobic coatings, and/or curvature effects [31–33,36–38,41] and have been able to reasonably match experimental results for large droplets ($> 10 \ \mu$m) [31,32].

The energy flowing through an individual droplet is then combined with the droplet size distribution on the surface, $N(r)$, and integrated over a range of radii, r, in order to find the heat flux, $\dot{q}''$, for a surface,

$$\dot{q}'' = \int\limits_{r_{min}}^{r_{max}} \dot{Q}_D(r)N(r)dr, \tag{2.2}$$

where either the classical Rose model [70], which stems from geometric arguments for spherical droplet growth, the Kim and Kim model [35], which stems from a population balance of direct condensation for small (nano- to micro-scale) droplets, or a combination of the two [31,33,35] is used for the distribution. In these models it is typically assumed that the energy transfer to the droplet comes solely from condensation (mass transport) onto the liquid, ignoring any thermal energy transport (due to a temperature gradient) resulting in

$$\dot{E} \approx \dot{q}''A = H_{LV}\dot{m} \tag{2.3}$$

where $\dot{E}$, $\dot{m}$, and H_{LV} are the total energy transfer, mass transfer, and latent heat.

Derivations for the equations used for the individual resistances can be found in the literature [31–33,36–38,41] and depend on both the physical properties of the system as well as the geometry and state of the droplet (Cassie-Baxter or Wenzel).
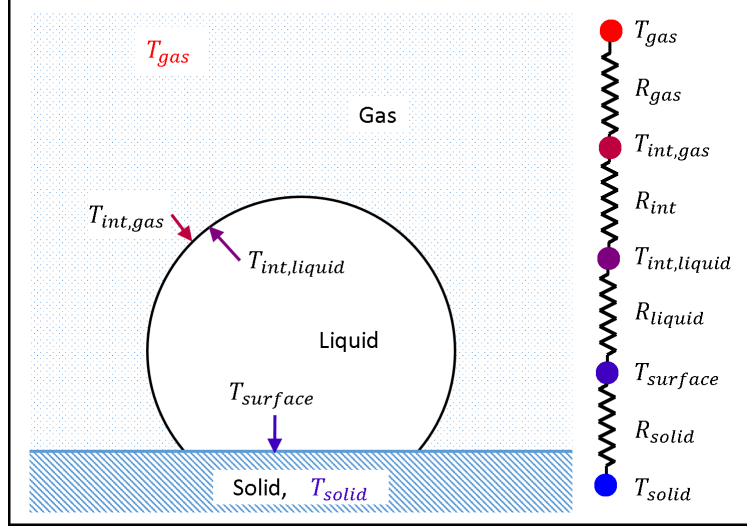
Fig. 2.1: Cartoon and resistor network for droplet condensation.

One commonly used result [32–35, 37, 71] for the resistance network is the interfacial heat transfer coefficient, h_i, given by

$$h_i = \frac{2\alpha}{2 - \alpha} \sqrt{\frac{m_p}{2\pi k_B}} \frac{\rho_V H_{LV}^2}{T_V} \tag{2.4}$$

where m_p and k_B are the mass of a condensing molecule and Boltzmann constant, ρ_V and T_V are the vapor density and temperature at the interface, and α is the accommodation coefficient. The above result is derived from Schrage's classical [72] result for the mass flux across a planar interface which was derived using kinetic theory [40] along with the Clausius-Claperyon equation. The accommodation coefficient is defined as the probability that a vapor particle will condense onto the liquid if it comes in contact with the liquid interface. Marek [73] adapted h_i by reworking the kinetic theory for a curved surface, $r = const$ instead of the planar $z = const$, but the droplet curvature (or radius) does not appear until the heat transfer coefficient is integrated over the droplet surface area. This detracts from Marek's correction because it is common to use α as a tuning parameter which make Schrage's and Marek's results

6

identical with just altered values for α. Furthermore, Eq. 2.4 does not depend on any liquid properties, such as temperature or pressure, which goes against experimental results by Fang and Ward [74–76] where a temperature jump across a liquid-vapor interface was seen and confirmed in molecular simulations by Røsjorde [77, 78] and Wilhelmsen [79, 80]. The temperature jump was also not insignificant, being on the order of 10°C, which is of the same order of magnitude as typical subcooling ranges and could have a significant impact on condensation heat transfer.

2.3   Continuum Motion Models

The following section will layout the continuum foundation for the remainder of this work. First conservation equations for a single phase system will be derived in section 2.3.1, then conservation equations for a two phase system will be derived in section 2.3.2. Derivation of these results are by no means original and can be found elsewhere [81–84] but are included for completeness.

2.3.1   Single Phase System

From the first law of thermodynamics, the total energy of a single phase system, $E = U + K$, is conserved therefore

$$\frac{dE}{dt} = \frac{dU}{dt} + \frac{dK}{dt} = \frac{dQ}{dt} + \frac{dW}{dt} \tag{2.5}$$

where t, U, K, Q, and W are time, total internal energy, total kinetic energy, total heat exchanged with the external environment, and work done on the system by both

body and traction forces. E, U, and K can be written as

$$E = \int_{V(t)} \rho e \ dV \tag{2.6a}$$

$$U = \int_{V(t)} \rho u \ dV \tag{2.6b}$$

$$K = \int_{V(t)} \rho ke \ dV = \frac{1}{2} \int_{V(t)} \rho \mathbf{v} \cdot \mathbf{v} \ dV \tag{2.6c}$$

where ρ, e, u, ke, $\mathbf{v}$, V are the mass density, specific energy, specific internal energy, specific kinetic energy, velocity, and volume of the system. The derivatives of heat and work can be written as

$$\frac{dQ}{dt} = -\int_{A(t)} \boldsymbol{q} \cdot \hat{\boldsymbol{n}} dA \tag{2.7a}$$

$$\frac{dW}{dt} = \int_{A(t)} \boldsymbol{T} \cdot \mathbf{v} dA + \int_{V(t)} \rho \boldsymbol{F} \cdot \mathbf{v} dV \tag{2.7b}$$

where $\boldsymbol{q}$, $\hat{\boldsymbol{n}}$, A, $\boldsymbol{T}$, and $\boldsymbol{F}$ are the total heat flux vector, surface normal, surface area, surface traction, and body force. Due to the small size of the systems being considered in this dissertation, gravitational body forces are assumed to be negligible. Furthermore, it will be assumed that the system is not in the presence of an external electric, magnetic, or any other type of field, and $\boldsymbol{F}$ will be assumed to be negligible for the remainder of this derivation. Utilizing Cauchy relations the traction can be related to the pressure tensor $\boldsymbol{P}$ by $\boldsymbol{T} = -\boldsymbol{P} \cdot \hat{\boldsymbol{n}}$. Combining Eqs. 2.5, 2.6, and 2.7 and using the divergence theorem to convert the surface integral to a volume integral, the local energy equation becomes

$$\rho \dot{e} = \rho(\dot{u} + \mathbf{v} \cdot \dot{\mathbf{v}}) + (u + \frac{1}{2}\mathbf{v} \cdot \mathbf{v})(\dot{\rho} + \rho \nabla \cdot \mathbf{v}) = -\nabla \cdot \boldsymbol{q} - \mathbf{v} \cdot (\nabla \cdot \boldsymbol{P}) - \boldsymbol{P} : \nabla \mathbf{v} \tag{2.8}$$

where $\dot{a} = \partial a/\partial t + \mathbf{v} \cdot \nabla a$ and noting that the Cauchy pressure tensor is symmetry, $\boldsymbol{P} = \boldsymbol{P}^T$. From the Galilean invariant principle, Eq. 2.8 should still hold in a transformation $\mathbf{v} \to \mathbf{v}_0 + \mathbf{v}$ where $\mathbf{v}_0$ is a constant, therefore

$$
\begin{aligned}
\rho(\dot{u} + (\mathbf{v}_0 + \mathbf{v}) \cdot \dot{\mathbf{v}}) + (u + \frac{1}{2}(\mathbf{v}_0 + \mathbf{v}) \cdot (\mathbf{v}_0 + \mathbf{v}))(\dot{\rho} + \rho\nabla \cdot \mathbf{v}) = \\
-\nabla \cdot \boldsymbol{q} - (\mathbf{v}_0 + \mathbf{v}) \cdot (\nabla \cdot \boldsymbol{P}) - \boldsymbol{P} : \nabla\mathbf{v}.
\end{aligned} \tag{2.9}
$$

Subtracting Eq. 2.8 from Eq. 2.9 and rearranging results in

$$
\frac{1}{2}\mathbf{v}_0 \cdot \mathbf{v}_0(\dot{\rho} + \rho\nabla\mathbf{v}) + \mathbf{v}_0 \cdot (\mathbf{v}(\dot{\rho} + \rho\nabla\mathbf{v}) + \rho\dot{\mathbf{v}} + \nabla \cdot \boldsymbol{P}) = 0. \tag{2.10}
$$

Since $\mathbf{v}_0$ is arbitrary this implies that

$$
\dot{\rho} + \rho\nabla \cdot \mathbf{v} = 0 \tag{2.11a}
$$

$$
\rho\mathbf{v} = -\nabla \cdot \mathbf{P}, \tag{2.11b}
$$

which can be used to simplify the local conservation of energy equation (Eq. 2.8) to

$$
\rho\dot{e} = \rho(\dot{u} + \mathbf{v} \cdot \dot{\mathbf{v}}) = -\nabla \cdot \boldsymbol{q} - \mathbf{v} \cdot (\nabla \cdot \boldsymbol{P}) - \boldsymbol{P} : \nabla\mathbf{v}. \tag{2.12}
$$

If $\mathbf{v}\cdot$ is taken on both sides of the conservation of momentum equation (Eq. 2.11b) and compared with the simplified energy equation, the local internal energy equation becomes apparent,

$$
\rho\dot{u} = -\nabla \cdot \boldsymbol{q} - \boldsymbol{P} : \nabla\mathbf{v}. \tag{2.13}
$$

Now that the Lagrangian forms of the conservation of mass, momentum, and energy equations have been derived, the equivalent Euler form of the conservation equations

9

are

$$\frac{D\rho}{Dt} = 0 \tag{2.14a}$$

$$\frac{D(\rho\mathbf{v})}{Dt} = -\nabla \cdot \boldsymbol{P} \tag{2.14b}$$

$$\frac{D(\rho e)}{Dt} = -\nabla \cdot \boldsymbol{q} - \mathbf{v} \cdot (\nabla \cdot \boldsymbol{P}) - \boldsymbol{P} : \nabla\mathbf{v} \tag{2.14c}$$

$$\frac{D(\rho u)}{Dt} = -\nabla \cdot \boldsymbol{q} - \boldsymbol{P} : \nabla\mathbf{v} \tag{2.14d}$$

where $Da/Dt = \partial a/\partial t + \nabla \cdot (a\mathbf{v})$.

2.3.2   Two Phase System

With the derivation for a single phase complete, conservation equations will be derived for a binary system consisting of fluids A and B. These fluids are as general as possible where A and B could be either liquid or gas phases of different fluids. These results also include the simpler system of interest in this work which is a single fluid in both the liquid and vapor phase. Following a similar derivation to the single phase system, two-phase equations can be derived

$$\frac{D_k\rho_k}{D_kt} = \sigma_k^\rho \tag{2.15a}$$

$$\frac{D_k(\rho_k\mathbf{v}_k)}{D_kt} = -\nabla \cdot \boldsymbol{P}_k + \boldsymbol{\sigma}_k^{\mathbf{v}} \tag{2.15b}$$

$$\frac{D_k(\rho_k e_k)}{D_kt} = -\nabla \cdot \boldsymbol{q}_k - \mathbf{v}_k \cdot (\nabla \cdot \boldsymbol{P}_k) - \boldsymbol{P}_k : \nabla\mathbf{v}_k + \sigma_k^e \tag{2.15c}$$

with $D_k a/D_k t = \partial a/\partial t + \nabla \cdot (a\mathbf{v}_k)$. Here a k subscript denotes a particular fluid phase A or B, the σ's represents source terms due to conversion of mass, momentum, or energy between A and B with $\sigma_A^\rho = -\sigma_B^\rho$, $\boldsymbol{\sigma}_A^{\mathbf{v}} = -\boldsymbol{\sigma}_B^{\mathbf{v}}$, $\sigma_A^e = -\sigma_B^e$ in order to maintain global conservation. The total density ρ and velocity of the center of mass

v are defined as

$$\rho = \rho_A + \rho_B \tag{2.16a}$$

$$\rho \mathbf{v} = \rho_A \mathbf{v}_A + \rho_B \mathbf{v}_B. \tag{2.16b}$$

It would be convenient to form similar conservation equations to the single phase system, Eqs. 2.14. This allows for general conclusions to be made relating quantities between a single component and multi-component system. Before that is done, it will be helpful to define the mass fraction c_k, the diffusive velocity $\mathbf{w}_k$, and diffusive flux $\boldsymbol{J}_k^\rho$ as

$$c_k = \frac{\rho_k}{\rho} \tag{2.17a}$$

$$\mathbf{w}_k = \mathbf{v}_k - \mathbf{v} \tag{2.17b}$$

$$\boldsymbol{J}_k^\rho = \rho_k \mathbf{w}_k. \tag{2.17c}$$

Combining the density equations for species A and B, Eq. 2.15a, results in the exact density conservation equation for a single phase system, Eq. 2.14a, with the updated definitions of ρ and $\mathbf{v}$, Eqs. 2.16a and 2.16b. Combining the momentum equations of species A and B yields

$$\frac{D_A(\rho_A \mathbf{v}_A)}{D_A t} + \frac{D_B(\rho_B \mathbf{v}_B)}{D_B t} = -\nabla \cdot (\boldsymbol{P}_A + \boldsymbol{P}_B). \tag{2.18}$$

In order for the left hand side of the equation to be of the single phase form, $\nabla \cdot (\rho_A \mathbf{w}_A \mathbf{w}_A + \rho_B \mathbf{w}_B \mathbf{w}_B)$ needs to be added to both sides of the equation. Defining $\boldsymbol{P}_k^* = \mathbf{P}_k + \rho_k \mathbf{w}_k \mathbf{w}_k$ and $\boldsymbol{P}^* = \boldsymbol{P}_A^* + \boldsymbol{P}_B^*$, where $\boldsymbol{ab}$ represent the dyadic product of

two vectors, results in

$$\frac{D(\rho\mathbf{v})}{Dt} = -\nabla \cdot \boldsymbol{P}^*, \tag{2.19}$$

which mirrors the forms of the single phase equation, Eq. 2.14b.

Previously, the velocity was combined with the momentum equation and compared with the energy equation to obtain the internal energy equation. However, $e_k = u_k + ke_k$ where ke_k is the kinetic energy associated with the center of mass of species k. Therefore, it is convenient to partition the energy by

$$e_k = u_k + \frac{1}{2}\mathbf{v}_k \cdot \mathbf{v}_k = u_k + \frac{1}{2}(\mathbf{w}_k - \mathbf{v}) \cdot (\mathbf{w}_k - \mathbf{v}) = u_k^* + ke_k^* - \mathbf{w}_k \cdot \mathbf{v} \tag{2.20}$$

where u_k^* takes the kinetic energy associated with $\mathbf{w}_k$ and ke_k^* is the kinetic energy associated with the center of mass motion of the system. The total energy of the system is can now be written as

$$\rho e = \rho u^* + \rho ke^* \tag{2.21}$$

because the extra terms $\mathbf{w}_k \cdot \mathbf{v}$ sum to 0. Combining the energy equations results in

$$\frac{D(\rho_A e_A)}{D_A t} + \frac{(D\rho_B e_B)}{D_B t} = -\nabla \cdot (\boldsymbol{q}_A + \boldsymbol{q}_B) - \mathbf{v}_A \cdot (\nabla \cdot \boldsymbol{P}_A) - \mathbf{v}_B \cdot (\nabla \cdot \boldsymbol{P}_B)$$
$$-\boldsymbol{P}_A : \nabla\mathbf{v}_A - \boldsymbol{P}_B : \nabla\mathbf{v}_B. \tag{2.22}$$

Similar to the momentum equation, the left hand side of the combined energy equation differs from $D(\rho e)/Dt$ by $\nabla \cdot (\rho_A e_A \mathbf{w}_A + \rho_B e_B \mathbf{w}_B)$; therefore

$$\frac{D(\rho e)}{Dt} = -\nabla \cdot (\boldsymbol{q}_A + \boldsymbol{q}_B) - \nabla \cdot (\boldsymbol{P}_A\mathbf{v}_A + \boldsymbol{P}_B\mathbf{v}_B) - \nabla \cdot (\rho_A u_A^* \mathbf{w}_A + \rho_B u_B^* \mathbf{w}_B)$$
$$-\nabla \cdot (\rho_A(\mathbf{v} \cdot \mathbf{w}_A)\mathbf{w}_A + \rho_B(\mathbf{v} \cdot \mathbf{w}_B)\mathbf{w}_B) \tag{2.23}$$

12

noting that the ke_k^* terms vanish due to $\boldsymbol{J}_A^\rho + \boldsymbol{J}_B^\rho = 0$. In order to form a single internal energy equation, $\mathbf{v}\cdot$ is applied to the momentum equation and compared with the total energy equation. However the two-phase momentum equation has $\boldsymbol{P}^*$, noting that $\boldsymbol{P}_A\mathbf{v}_A + \boldsymbol{P}_B\mathbf{v}_B = \boldsymbol{P}^*\mathbf{v} + \boldsymbol{P}_A\mathbf{w}_A + \boldsymbol{P}_B\mathbf{w}_B - (\rho_A\mathbf{w}_A\mathbf{w}_A + \rho_B\mathbf{w}_B\mathbf{w}_B)\mathbf{v}$, the total energy equation becomes

$$\frac{D(\rho e)}{Dt} = -\nabla \cdot (\boldsymbol{q}_A + \boldsymbol{q}_B) - \mathbf{v} \cdot (\nabla \cdot \boldsymbol{P}^*) - \boldsymbol{P}^* : \mathbf{v} - \nabla \cdot (\rho_A u_A^* \mathbf{w}_A + \rho_B u_B^* \mathbf{w}_B)$$
$$-\nabla \cdot (\boldsymbol{P}_A\mathbf{w}_A + \boldsymbol{P}_B\mathbf{w}_B)$$

$$(2.24)$$

which when compared with $\mathbf{v}\cdot$ of the momentum equation results in

$$\frac{D(\rho u^*)}{Dt} = -\nabla \cdot \boldsymbol{q}^* - \boldsymbol{P}^* : \nabla\mathbf{v} \qquad (2.25)$$

where $\boldsymbol{q}^*$ absorbed all extra terms, similar to $\boldsymbol{P}^*$ in the momentum equation.

In addition to the mass, momentum, and internal energy equations, an additional equation needs to be formed in order to completely define the system. Either A or B's individual mass equation could be used, but often concentration equations using the definition of the diffusive flux, $\boldsymbol{J}_k$ are formed such that

$$\frac{D(\rho c_k)}{Dt} = -\nabla \cdot \boldsymbol{J}_k^\rho + \sigma_k^\rho. \qquad (2.26)$$

It does not matter which equation is solved, and it is common to write the equations as phase fractions with $\alpha = c_B$ or $\phi = c_B - c_A$ causing $\alpha \in [0, 1]$ or $\phi \in [-1, 1]$ and

transforming the phase equations to

$$\frac{D(\rho\alpha)}{Dt} = -\nabla \cdot \boldsymbol{J}_\alpha^\rho + \sigma_\alpha^\rho. \tag{2.27a}$$

$$\frac{D(\rho\phi)}{Dt} = -\nabla \cdot \boldsymbol{J}_\phi^\rho + \sigma_\phi^\rho. \tag{2.27b}$$

with $\boldsymbol{J}_\alpha^\rho = \boldsymbol{J}_B^\rho$, $\boldsymbol{J}_\phi^\rho = \boldsymbol{J}_B^\rho - \boldsymbol{J}_A^\rho$, $\sigma_\alpha^\rho = \sigma_B^\rho$, and $\sigma_\phi^\rho = \sigma_B^\rho - \sigma_A^\rho$.

General conservation equations for a binary system have be derived that mirror the single phase system with slightly modified definitions of the heat flux vector and pressure tensor. In summary, the conservation equations for a binary system are

$$\frac{D\rho}{Dt} = 0 \tag{2.28a}$$

$$\frac{D(\rho\mathbf{v})}{Dt} = -\nabla \cdot \boldsymbol{P}^* \tag{2.28b}$$

$$\frac{D(\rho u^*)}{Dt} = -\nabla \cdot \boldsymbol{q}^* - \boldsymbol{P}^* : \nabla\mathbf{v} \tag{2.28c}$$

$$\frac{D(\rho\alpha)}{Dt} = -\nabla \cdot \boldsymbol{J}_\alpha^\rho + \sigma_\alpha^\rho \qquad \text{or} \qquad \frac{D(\rho\phi)}{Dt} = -\nabla \cdot \boldsymbol{J}_\phi^\rho + \sigma_\phi^\rho \tag{2.28d}$$

or in Lagrangian form

$$\dot{\rho} = -\rho\nabla \cdot \mathbf{v} \tag{2.29a}$$

$$\rho\dot{\mathbf{v}} = -\nabla \cdot \boldsymbol{P}^* \tag{2.29b}$$

$$\rho\dot{u}^* = -\nabla \cdot \boldsymbol{q}^* - \boldsymbol{P}^* : \nabla\mathbf{v} \tag{2.29c}$$

$$\rho\dot{\alpha} = -\nabla \cdot \boldsymbol{J}_\alpha^\rho + \sigma_\alpha^\rho \qquad \text{or} \qquad \rho\dot{\phi} = -\nabla \cdot \boldsymbol{J}_\phi^\rho + \sigma_\phi^\rho \tag{2.29d}$$

14

with

$$\boldsymbol{P}^* = \boldsymbol{P}_A + \boldsymbol{P}_B + \rho \mathbf{w}_A \mathbf{w}_A + \rho \mathbf{w}_B \mathbf{w}_B \tag{2.30a}$$

$$\boldsymbol{q}^* = \boldsymbol{q}_A + \boldsymbol{q}_B + \rho_A u_A^* \mathbf{w}_A + \rho_B u_B^* \mathbf{w}_B + \boldsymbol{P}_A \mathbf{w}_A + \boldsymbol{P}_B \mathbf{w}_B. \tag{2.30b}$$

This concludes the section of governing equations due to global conservation laws of mass, momentum, and energy.

2.4 Non-equilibrium Thermodynamics

The following section will discuss the thermodynamic background for this work. Similar derivations to this section can also be found in [81–84]. A key assumption of non-equilibrium thermodynamics is the local equilibrium hypothesis. The local equilibrium hypothesis states that a non-equilibrium system can be decomposed into small domains such that the instantaneous thermodynamic and mechanical properties of the domains are the same as a system that is in uniform equilibrium. These small domains still contain a large number of molecules in the classical sense such that each sub domain can still be treated as a continuum.

As with energy, Eq 2.6, the total entropy S of a system can be written in specific form as

$$S = \int_{V(t)} \rho s \, dV. \tag{2.31}$$

The time derivate of S can be decomposed into an external and internal portion

$$\frac{dS}{dt} = \frac{dS_e}{dt} + \frac{dS_i}{dt}. \tag{2.32}$$

15

with

$$\frac{dS_e}{dt} = -\int_{A(t)} \boldsymbol{J}_s \cdot \hat{\boldsymbol{n}} \, dA = -\int_{V(t)} \nabla \cdot \boldsymbol{J}_s \, dV \qquad (2.33a)$$

$$\frac{dS_i}{dt} = \int_{V(t)} \sigma^s \, dV \qquad (2.33b)$$

where $\boldsymbol{J}_s$ and σ^s represent the entropy flowing through the boundaries of the system and the entropy generation within the system. Taking the time derivative of Eq. 2.31 and using Eq. 2.33, the local form of the entropy equation is

$$\rho\dot{s} = -\nabla \cdot \boldsymbol{J}_s + \sigma^s. \qquad (2.34)$$

From the thermodynamic postulate, the internal energy u of a binary system is a function of the entropy density s, specific volume $\nu = \rho^{-1}$, and concentrations c_A and c_B, $u = f(s(\boldsymbol{r}, t), \nu(\boldsymbol{r}, t), c_A(\boldsymbol{r}, t), c_B(\boldsymbol{r}, t))$, where $\boldsymbol{r}$ and t denote the spatial vector with respect to a global reference frame and time. The total derivative of the internal energy is given by

$$du = \frac{\partial u}{\partial s}ds + \frac{\partial u}{\partial \nu}d\nu + \frac{\partial u}{\partial c_A}dc_A + \frac{\partial u}{\partial c_B}dc_B \qquad (2.35)$$

where the partial derivatives are taken at constant values of the remaining three variables. Using the standard definition for temperature $T = \partial u/\partial s$, pressure $P = -\partial u/\partial \nu$, and chemical potential $\mu_k = \partial u/\partial c_k$ yields

$$du = Tds - Pd\nu + \mu_A dc_A + \mu_B dc_B. \qquad (2.36)$$

Noting that $c_A + c_B = 1 \rightarrow dc_A = -dc_B$ (see Sec. 2.3.2 $\alpha \equiv c_B$), and defining excess

16

chemical potential $\mu \equiv \mu_B - \mu_A$, Eq. 2.36 can be rearranged to

$$du = Tds - Pd\nu + \mu d\alpha. \tag{2.37}$$

Converting the total derivatives to time derivatives and rearranging the equation to solve for $\dot{s}$ yields

$$\dot{s} = \frac{\dot{u}}{T} + \frac{P\dot{\nu}}{T} - \frac{\mu\dot{\alpha}}{T}. \tag{2.38}$$

Replacing $\dot{u}$, $\dot{\nu}$, and $\dot{\alpha}$ with the results from Eq. 2.29 and rearranging to a form similar to Eq. 2.34, results in

$$\rho\dot{s} = -\nabla \cdot \left(\frac{\boldsymbol{q}^*}{T} - \frac{\mu\boldsymbol{J}_\alpha^\rho}{T}\right) + \boldsymbol{q}^* \cdot \nabla\frac{1}{T} - \frac{1}{T}\boldsymbol{\tau}^* : \nabla\mathbf{v} - \boldsymbol{J}_\alpha^\rho \cdot \nabla\left(\frac{\mu}{T}\right) + \sigma_\alpha^\rho\frac{\mu}{T} \tag{2.39}$$

with $\boldsymbol{\tau}^* = \boldsymbol{P}^* - P\boldsymbol{I}$ where $\boldsymbol{I}$ is the identity tensor, and $\boldsymbol{q}^*$ and $\boldsymbol{J}_\alpha^\rho$ are the modified total heat flux and diffusive phase flux defined by Eqs. 2.17c and 2.30b. Comparing with Eq. 2.34, it can readily be seen that

$$\boldsymbol{J}_s = \frac{\boldsymbol{q}^*}{T} - \frac{\mu\boldsymbol{J}_\alpha^\rho}{T} \tag{2.40a}$$

$$\sigma^s = \boldsymbol{q}^* \cdot \nabla\frac{1}{T} - \frac{1}{T}\boldsymbol{\tau}^* : \nabla\mathbf{v} - \boldsymbol{J}_\alpha^\rho \cdot \nabla\left(\frac{\mu}{T}\right) + \sigma_\alpha^\rho\frac{\mu}{T}, \tag{2.40b}$$

and if $\phi \in [-1, 1]$ is used instead of $\alpha \in [0, 1]$ then

$$\boldsymbol{J}_s = \frac{\boldsymbol{q}^*}{T} - \frac{\mu_\phi\boldsymbol{J}_\phi^\rho}{T} \tag{2.41a}$$

$$\sigma^s = \boldsymbol{q}^* \cdot \nabla\frac{1}{T} - \frac{1}{T}\boldsymbol{\tau}^* : \nabla\mathbf{v} - \boldsymbol{J}_\phi^\rho \cdot \nabla\left(\frac{\mu_\phi}{T}\right) + \sigma_\phi^\rho\frac{\mu_\phi}{T} \tag{2.41b}$$

with $\mu_\phi = (\mu_B - \mu_A)/2$. The entropy generation, σ^s, presents itself as the sum of

Table 2.1: Forces X_i and fluxes J_i for entropy generation.

α	X_i	$\nabla(1/T)$	$-\nabla(\mu/T)$	$-\nabla\mathbf{v}/T$	μ/T
	J_i	$\boldsymbol{q}^*$	$\boldsymbol{J}_\alpha^\rho$	$\boldsymbol{\tau}^*$	σ_α^ρ
ϕ	X_i	$\nabla(1/T)$	$-\nabla(\mu_\phi/T)$	$-\nabla\mathbf{v}/T$	μ_ϕ/T
	J_i	$\boldsymbol{q}^*$	$\boldsymbol{J}_\phi^\rho$	$\boldsymbol{\tau}^*$	σ_ϕ^ρ

forces X_i multiplied by fluxes J_i,

$$\sigma^s = \sum_i J_i X_i. \tag{2.42}$$

The breakdown of what is a force and what constitutes a flux is somewhat arbitrary, but for this work, the breakdown is shown in Table 2.1.

The forces are known functions of the state variables and potentially their gradients, T, P, and α (or ϕ). Experimentally the fluxes and forces have been show to have dependent relations such that $J_i = f(X_1, ..., X_n; T, P, \alpha)$ with both vanishing when the system is in equilibrium. The relationships between the forces and fluxes are often known as constitutive equations. If a linear expansion is made about the fluxes then

$$J_i = \sum_j L^{ij} X_j \tag{2.43}$$

where $L^{ij} = (\partial J_i/\partial X_j)$ are expected to be physical scalar coefficients such as thermal conductivity, shear viscosity, or the diffusion coefficients. Onsager postulated the symmetry of these coefficients such that $L^{ij} = L^{ji}$, and L^{ij} are often called the Onsager coefficients.

2.5 Molecular Dynamics

The following section will give a brief overview of molecular dynamics simulations in Sec 2.5.1, however, more detailed discussions on molecular dynamics can be found elsewhere [85–88]. Connections linking molecular dynamics to the continuum models of Secs. 2.3 and 2.4 will be made in section 2.5.2. Section 2.5.3 will discuss the calculation of some physical quantities using molecular dynamics while section 2.5.4 will discuss controlling the temperature and chemical potential in molecular dynamics.

2.5.1   Overview of Molecular Dynamics

Molecular dynamics (MD) is a simulation method used which models the behavior of a system by modeling every molecule or atom in a system explicitly. It assumes that the particles interact in the classical sense, ignoring any quantum effects. Newton's equation of motion can be written for each individual particle as

$$\frac{d^2 \boldsymbol{r}_i}{dt^2} = \frac{\boldsymbol{F}_i}{m_i} \tag{2.44}$$

where m_i, $\boldsymbol{r}_i$, and $\boldsymbol{F}_i$, denote particle i's mass, position, and net force while t denotes time. The force on each particle is related to the potential energy of the particle, $\mathcal{V}_i$, by

$$\boldsymbol{F}_i = \nabla \mathcal{V}_i(\boldsymbol{r}_1, ..., \boldsymbol{r}_N) \tag{2.45}$$

where N is the number of particles consider in the system. This result couples the N equations of motion for the system. Due to the large number of equations the system is often solved numerically with a time integration scheme such as the velocity-Verlet algorithm.

In order to integrate Eq. 2.44, an interaction potential between particles is needed. A commonly used interaction potential between particles is the two-body Lennard-Jones potential given by

$$\mathcal{V}^{LJ}(r) = 4\epsilon \left(\frac{\sigma^{12}}{r^{12}} - \frac{\sigma^6}{r^6} \right) \tag{2.46}$$

where ϵ and σ are energetic well depth and zero potential distance between particles i and j while $r = |\boldsymbol{r}_{ij}| = |\boldsymbol{r}_i - \boldsymbol{r}_j|$ is the distance between particles i and j. The Lennard-Jones potential has shown excellent correlation with the experiment results for argon in both the liquid and vapor phase. The parameters ϵ, σ, and m for argon are 0.3405 nm, 0.01032 eV, and 39.948 amu respectively [85].

2.5.2 Connection to Continuum Models

In order for MD to be meaningful in a continuum sense properties such as velocity, mass, temperature, energy, and pressure must be calculated in the system. The energy of an MD system E is defined as

$$E = U + K^{com} = \mathcal{V} + K^{mic} + K^{com}. \tag{2.47}$$

where U, K^{com}, $\mathcal{V}$, and K^{mic} is the internal energy, kinetic energy related to bulk or center of mass motion, potential energy due to atomic interactions, and kinetic energy due to thermal motion. However in sections 2.3 and 2.4 the internal energy for a two phase system was decomposed as

$$E = U_A + K_A^{com} + U_B + K_B^{com} = \mathcal{V}_A + K_A^{mic} + K_A^{com} + \mathcal{V}_B + K_B^{mic} + K_B^{com}. \tag{2.48}$$

In order for the MD simulations to be meaningful both of these energy definitions should be the same which is not readily apparent. Since the potential energy is due solely to particle positions

$$\mathcal{V} = \sum_{i=1}^{N} \mathcal{V}_i = \sum_{i=1}^{N_A} \mathcal{V}_i + \sum_{i=1}^{N_B} \mathcal{V}_i = \mathcal{V}_A + \mathcal{V}_B \qquad (2.49)$$

where $N = N_A + N_B$ is the total number of particles while N_A and N_B are the number of particles in species A and B. What remains to be shown is that the kinetic energy terms in Eqs. 2.47 and 2.48 are equal with each term being defined as

$$K_k^{com} = \frac{1}{2} m_k \mathbf{v}_k^2, \qquad K^{com} = \frac{1}{2} m \mathbf{v}^2 \qquad (2.50a)$$

$$K_k^{mic} = \sum_{i=1}^{N_k} \frac{m_i}{2} (\mathbf{v}_i - \mathbf{v}_k)^2, \qquad K^{mic} = \sum_{i=1}^{N} \frac{m_i}{2} (\mathbf{v}_i - \mathbf{v})^2 \qquad (2.50b)$$

where k denotes phase A or B. The masses and velocities are defined as

$$m_k = \sum_{i=1}^{N_k} m_i, \qquad m = \sum_{i=1}^{N} m_i = m_A + m_B \qquad (2.51a)$$

$$\mathbf{v}_k = \sum_{i=1}^{N_k} \frac{m_i}{m_k} \mathbf{v}_i, \qquad \mathbf{v} = \sum_{i=1}^{N} \frac{m_i}{m} \mathbf{v}_i = \frac{m_A \mathbf{v}_A + m_B \mathbf{v}_B}{m}. \qquad (2.51b)$$

If the quadratic terms in Eq. 2.50b are expanded and combined with the center of mass terms in Eq. 2.50a along with the definitions of velocity, it can be shown that

$$K_k^{mic} + K_k^{com} = \sum_{i=1}^{N_k} \frac{m_i}{2} \mathbf{v}_i^2 = K_k^{part} \qquad (2.52a)$$

$$K^{mic} + K^{com} = \sum_{i=1}^{N} \frac{m_i}{2} \mathbf{v}_i^2 = K^{part}. \qquad (2.52b)$$

Now it can be readily seen that the kinetic energy terms in Eqs. 2.47 and 2.48 are indeed equal because

$$K^{mic} + K^{com} = K^{part} = K_A^{part} + K_B^{part} = K_A^{mic} + K_A^{com} + K_B^{mic} + K_B^{com}. \quad (2.53)$$

Equation 2.47 and Eq. 2.48 representing the same total energy E allows for a connection between the continuum models of sections 2.3-2.4 and MD. It should be noted that the averages of the molecular simulations should contain a sufficient number of particle in order to accurately represent a continuum fluid. This can be done by spatial and/or time averaging to increase the number of particles sampled.

The microscopic energies in Eq. 2.50b define the thermal energy of a particular system which allows for a microscopic definition of temperature T using the equipartition of energy as

$$dk_B T = 2K^{mic} \quad (2.54)$$

where d is the dimensionality of the system. This definition allows for only variations in the motion of the fluid to be captured because the bulk velocity of the system is not contained in K^{mic}. The pressure P for a system is defined as

$$P = -\rho k_B T - \frac{1}{3V} \sum_{i=1}^{N} \sum_{j \neq i}^{N} \boldsymbol{r}_{ij} \cdot \boldsymbol{F}_{ij} \quad (2.55)$$

while the pressure tensor $\boldsymbol{P}$ is defined as

$$\boldsymbol{P} = -\frac{m}{V} \sum_{i=1}^{N} \mathbf{v}_i \mathbf{v}_i - \frac{1}{2V} \sum_{i=1}^{N} \sum_{j \neq i}^{N} \boldsymbol{r}_{ij} \boldsymbol{F}_{ij}. \quad (2.56)$$

The second term in P and $\boldsymbol{P}$ is often called the viral (or excess) pressure as it is the contribution from molecular interactions while the first term is the ideal gas

contribution. The total heat flux for a molecular region is

$$q = \frac{1}{V} \sum_{i=1}^{N} \left[(K_i + \mathcal{V}_i)\mathbf{v}_i - \boldsymbol{P}_i\mathbf{v}_i \right] \tag{2.57}$$

where K_i and $\mathcal{V}$ are the kinetic and potential energies of particle i. With these molecular definitions of $\boldsymbol{P}$ and q it is now possible to calculate the quantities in section 2.3.

2.5.3 Additional Physical Properties

Viscosity: The dynamic viscosity η can be calculated from the Green-Kubo formula is [85]

$$\eta = \frac{V}{k_B T} \int_0^\infty \langle P_{\alpha\beta}(0)P_{\alpha\beta}(t) \rangle dt \tag{2.58}$$

where $P_{\alpha\beta}$ are the off diagonal elements of $\boldsymbol{P}$ and α and β refer to the x, y, or z coordinates with the condition that $\alpha \neq \beta$.

Planar Surface Tension: The planar surface tension σ_{ST} between two fluids is related to the normal pressure P_N and transverse pressure P_T spanning the interface of the fluids and is given by [85]

$$\sigma_{ST} = \int P_N(x) - P_T(x)dx. \tag{2.59}$$

Here the interface is assumed to be in the yz plane, and the integral is evaluated sufficiently far into the bulk regions of the two distinct fluids.

Chemical Potential: Formally the chemical potential μ is the derivative of the Helmholtz free energy F at constant volume and temperature [85, 86]. From a statistical mechanics perspective $F = -k_B T \ln Q(N, V, T)$ where $Q(N, V, T)$ is the classical partition function for a system of N molecules in a volume V at temperature T. It is common to separate, $F = F_{id} + F_{ex}$, where F_{id} and F_{ex} are the contributions from an ideal gas and the excess contribution resulting in

$$\mu = \mu_{id} + \mu_{ex} \tag{2.60a}$$

$$\mu_{id} = k_B T \ln(\rho \Lambda^3) \tag{2.60b}$$

$$\mu_{ex} = -k_B T \ln \left[\int \langle \exp(-\Delta \mathcal{V}/k_B T) \rangle d\boldsymbol{r}_{N+1} \right] \tag{2.60c}$$

where ρ is the number density, Λ is the de Broglie wavelength, and $\Delta \mathcal{V} \equiv \mathcal{V}(\boldsymbol{r}_{N+1}) - \mathcal{V}(\boldsymbol{r}_N)$ is the energetic difference by adding one molecule to the system. The ideal gas contribution is readily calculable if the density is known, and in molecular simulations, the excess portion can be sampled by placing test particles and calculating the energy change in the system. This is commonly referred to as the test particle method or Widom sampling [85, 86, 89]. Furthermore the chemical potential in Sec. 2.4 is the difference between species A and B, $\mu_{BA} = \mu_B - \mu_A$, therefore $\mu_{BA} = \mu_{B_{id}} + \mu_{B_{ex}} - \mu_{A_{id}} - \mu_{A_{ex}}$. Utilizing the phase fraction α and assuming that the excess chemical potential is split between the two species based on α the excess chemical potential $\mu_{BA_{ex}}$ is

$$\mu_{BA_{ex}} = (2\alpha - 1)\mu_{ex}. \tag{2.61}$$

Dimensionless Units: The three primary units for MD simulations are the energetic well depth between particles ϵ, the zero potential distance σ, and the particle mass m. Due to the small values of ϵ, σ, and m in SI units for physical systems it

Table 2.2: Dimensionless parameters for MD simulations.

Quantity	Dimensionless Relation
Length	$L^* = \dfrac{L}{\sigma}$
Energy	$E^* = \dfrac{E}{\epsilon}$
Mass	$M^* = \dfrac{M}{m}$
Number Density	$\rho^* = \dfrac{N}{V/\sigma^3} = \rho\sigma^3$
Mass Density	$\rho^* = \dfrac{mN}{V/\sigma^3} = \rho\sigma^3$
Temperature	$T^* = \dfrac{k_B T}{\epsilon}$
Pressure	$P^* = \dfrac{P}{\epsilon/\sigma^3}$
Time	$t^* = \dfrac{t}{\sqrt{m\sigma^2/\epsilon}}$
Surface Tension	$\gamma^* = \dfrac{\gamma}{\epsilon/\sigma^2}$
Viscosity	$\eta^* = \dfrac{\eta}{\sqrt{m\epsilon/\sigma^4}}$

is often convenient to run simulations using dimensionless parameters where physical properties have been appropriately scaled so that they are dimensionless using ϵ, σ, m, and other physical constants namely the Boltzmann constant k_B. Table 2.2 shows the dimensionless properties denoted with a "$*$" and how they are scaled. Unless otherwise noted MD simulations throughout the remainder of this dissertation are run in dimensionless units and can be converted to real units for argon using $\sigma = 3.405$ Å, $\epsilon/k_B = 120.96$ K, and $m = 39.948$ amu [85], and m is the mass of one particle.

2.5.4 Controlling Temperature and Chemical Potential

It is often desirable to control certain physical properties in MD simulations to mirror experimental conditions. In this dissertation the two parameters that are controlled during the simulations are the temperature T and chemical potential μ. Based upon Eq. 2.54, the temperature is computed through the particle velocities in the system. There are several thermostatting methods in MD simulations known as rescaling [85], Berendsen [90], Langevin [91], and Nosé-Hoover [92] thermostats. These thermostats each have various benefits and drawbacks both physically and computationally which can be found in the literature. The thermostats used in this dissertation are the rescaling, Berendsen, and Langevin thermostats. Briefly, rescaling thermostats alter the particle velocities at the end of the time integration stage of MD such that the temperature is the desired value from Eq. 2.54, while the Berendsen and Langevin thermostats apply forces (often small in magnitude compared to other forces) to the particles in the system such that T will return to its desired value in a time τ_T. Rescaling thermostats abruptly change the particle trajectories and lack physical justification but are computationally efficient while the remaining thermostats have various levels of physical justification based on how the restoring forces are applied but are computationally more expensive.

In order to control the chemical potential in MD simulations, molecular dynamics is coupled to grand canonical Monte Carlo (GCMC) [93–100] and is often referred to as grand canonical molecular dynamics (GCMD). Briefly GCMD has a control volume (or volumes) within the simulation domain where GCMC is performed between the MD timesteps. GCMC attempts individual particle translations (and rotations in molecular systems), insertions, and deletions all with an acceptance criteria based on the desired value of μ. The insertion and deletion of particles is based on the idea

of connecting the GCMC region to a large bath at chemical potential μ. The particle insertion and deletion idea is similar to the idea of calculating the excess chemical potential via the test particle method, but rather than calculate the chemical potential the particles are inserted or removed to control the chemical potential. A more detailed discussion of GCMC can be found in the literature [85].

3 Curvature Dependence of the Mass Accommodation Coefficient

3.1 Introduction

Condensation is of central importance in a broad range of areas in both nature [101–109] and industry [19, 25, 28–30, 110–115]. Aerosol-cloud interactions, currently a significant open question in climate modeling, are driven by the condensation of atmospheric water vapor onto cloud condensation nuclei [101–104]. Water harvesting which occurs in living organisms including cacti [106, 109], beetles [107, 108], and spiders [105], and in engineered systems for irrigation [111], supplementation of domestic water supply [111–113], and power plant cooling tower steam recovery [112], relies heavily on droplet condensation from the surrounding air or fog. Vapor chambers [114], useful for cooling microelectronics, are a practical application where dropwise condensation is pertinent, and experimental results have shown that adding nano-scale topographical [116–120] or surface energy [121–123] patterning to the condensing surfaces can greatly improve the overall heat transfer coefficient. Power generation [28–30] and desalination [19, 25, 30, 115] both rely heavily on condensers within the plant cycles that can have significant inefficiencies [28], offering a viable avenue where improvement to condensation processes can have a significant impact on the energetic requirements of these facilities.

Theoretical models are often used to predict the rates of liquid water and latent heat production during condensation processes [116–120, 124, 125]. A key component in many condensation models is the liquid-vapor interfacial thermal resistance. This resistance depends upon the mass accommodation coefficient, α, which represents the

likelihood that a vapor molecule that impinges upon a liquid-gas interface condenses into the bulk liquid. This interfacial resistance increases as droplet radius decreases, and dominates the condensation heat and mass transfer for droplets with radii below 1 μm [118, 119]. In these models, the value for α is often assumed or estimated from computer simulations as it is difficult to obtain experimentally [116, 117, 124–129].

Molecular dynamics (MD) simulations, which track condensation and evaporation processes at the molecular level, are well suited for mass accommodation studies and have been used to calculate α for a wide range of simple fluids and for more complex systems including binary liquid mixtures, non-condensable gases, and surface monolayer coatings [1–4, 130–140]. All but one of the previous studies in the literature focused on planar liquid-gas interfaces. The applicability of planar accommodation coefficients to the high-curvature interfaces of very small droplets, for example the submicron droplets produced on advanced condenser surfaces [117–120] and the critical water nuclei responsible for cloud formation [134], is unclear. Curvature effects are known to be important for other interfacial properties such as surface tension [141–147], and may also be relevant for mass accommodation. Julin *et al.* [134] performed the only previous study of the effect of curvature on α. For water droplets with radii of approximately 2 nm and 4 nm at 273.15 K, they found that α slightly increased with radius, but that it did not significantly deviate from its planar value. In the present work, a systematic MD study of the mass accommodation coefficient at equilibrium liquid-vapor interfaces is presented for a variety of pure fluids at a range of temperatures. In contrast to previous work, this work shows that α is size-dependent, varying from the bulk value for larger droplets down to zero for the smallest droplets, and that its bulk value is not generally equal to one. In addition, scaling reveals a universal curvature dependence for all fluids and temperatures considered.

3.2 Molecular Dynamics Simulations

To compute α, stable spherical equilibrium droplets of varying sizes were first prepared in MD using cubic domains with periodic boundary conditions. Lennard-Jones, Buckingham, benzene, n-butane, methane, methanol, and water droplets were simulated at multiple temperatures (Table 3.9). Lennard-Jones fluids with repulsive forces proportional to r^{-k}, where $k = \{12, 9\}$, and Buckingham fluids with repulsive forces proportional to $e^{6k(1-r)}$, where $k = \{3, 2\}$, were studied. Benzene, butane, methane, and methanol were modeled using transferable potentials for phase equilibria [148–151] while water was modeled using the TIP4P/2005 potential [152]. Figure 3.1 shows a continuum representation of the entire liquid-vapor simulation domain and a zoomed-in atomistic snapshot of a stable Lennard-Jones droplet. The radius of each droplet, indicated by the blue line in Fig. 3.1, is defined as the location where the fluid density is the average of the bulk liquid and vapor densities, $\rho(R) = (\rho_L + \rho_V)/2$. At temperatures for which the coexisting phases are well described as incompressible liquid and ideal gas, the MD-obtained droplet radii were found to agree well with Kelvin equation predictions.

3.2.1 Interaction Potentials

This section briefly describes the energetic potentials used in this work. The numerical values for all parameters can be found in Tables 3.1, 3.2, 3.3, 3.4, and 3.5.
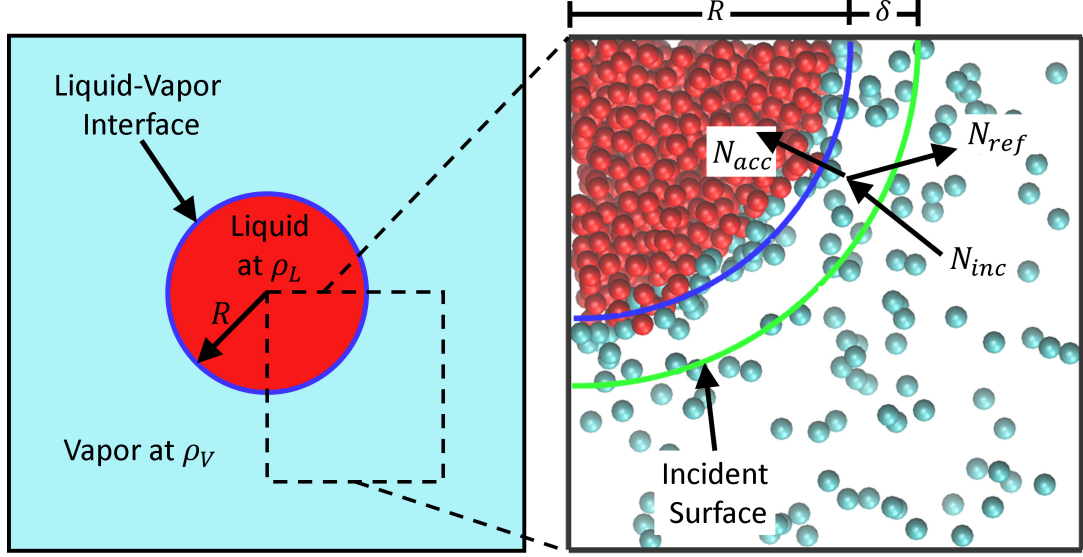
Fig. 3.1: Continuum (left) and atomistic (right) representations of a Lennard-Jones droplet. N_{inc}, N_{acc}, and N_{ref} refer to the number of incident, accommodated, and reflected molecules. The solid green line indicates the incident surface. The blue line indicates the liquid-vapor interface, defined as the location where the density is midway between the bulk liquid and vapor densities.

Lennard-Jones and Buckingham Potentials: Molecular dynamics simulations were first performed with a simple particle potentials. The Lennard-Jones,

$$U_{k,6}^{LJ}(r_{ij}) = 4\epsilon_{ij}\left(\left(\frac{\sigma_{ij}}{r_{ij}}\right)^k - \left(\frac{\sigma_{ij}}{r_{ij}}\right)^6\right), \tag{3.1}$$

and Buckingham potentials,

$$U_{k,6}^{B}(r_{ij}) = 4\epsilon_{ij}\left(\frac{e^{6k(1-r_{ij}/\sigma_{ij})}}{k} - \left(\frac{\sigma_{ij}}{r_{ij}}\right)^6\right), \tag{3.2}$$

were used where r_{ij}, ϵ_{ij}, and σ_{ij} denote the distance, potential well depth, and zero potential distance between particles i and j, while k denotes the strength of the repulsive force. For the Lennard-Jones potentials values of $k = 12$ and $k = 9$ were used while values of $k = 3$ and $k = 2$ were used for the Buckingham potential. The

above potentials were truncated and shifted at a cutoff radius of r_c. Dimensionless values were used for all Lennard-Jones and Buckingham simulations, and parameters can be converted to real units for argon using $\sigma = 3.405$ Å, $\epsilon/k_B = 120.96$ K, and $m = 39.948$ amu [85], where k_B is the Boltzmann constant and m is the mass of one particle.

Water, TIP4P/2005: Water simulations were performed using the TIP4P/2005 potential [152]. The TIP4P/2005 model was chosen because it is a commonly used water model that has coexistence densities that agree well with experimental values [153, 154]. TIP4P/2005 models the intermolecular interactions with a Lennard-Jones potential along with a Coulombic interactions

$$U_W(r_{ij}) = U_{12,6}^{LJ}(r_{ij}) + \frac{q_i q_j}{4\pi\epsilon_0 r_{ij}} \tag{3.3}$$

where q_i and q_j denotes the charge of particles i and j and ϵ_0 is the electric constant. In the TIP4P/2005 model, only the O-O interactions have non-zero ϵ_{ij}. In the TIP4P/2005 model, the charge for the O atom is placed at a massless location 0.1546 Å from the O atom along the bisecting angle between the H atoms. The Lennard Jones portion of the potential has a cutoff of r_c while the long range Coulombic interactions were handled with a particle-particle particle-mesh solver (PPPM) [85]. The O-H bond length and H-O-H bond angle were constrained with the SHAKE algorithm [155]. Further details of the TIP4P/2005 model can be found in the literature [152].

Methane and Butane, TraPPE: Simulations modeling alkanes, methane (CH_4) and butane (n-butane, C_4H_{10}), were simulated using the transferable potentials for

phase equilibria (TraPPE) [148,149]. Methane was modeled using the explicit hydrogen model (TraPPE-EH) [149]. The carbon and hydrogen from different molecules interact through a smoothed Lennard Jones potential

$$
U_{ALK}(r_{ij}) = \begin{cases} U_{12,6}^{LJ}(r_{ij}) & \text{if } r_{ij} \leq r_{in} \\ U^S(r_{ij}) & \text{if } r_{in} < r_{ij} \leq r_c \\ 0 & \text{else} \end{cases} \tag{3.4}
$$

where r_{in} is the inner cutoff radius and $U^S(r_{ij})$ is a quartic polynomial such that $U_{ALK}(r_{ij})$ and $\nabla U_{ALK}(r_{ij})$ vary smoothly to zero between the inner and outer cutoff radii. The motivation for using a smoothed potential as opposed to a simple truncated potential for alkanes can be found in the literature [156,157]. Non-bonded interactions between the carbon and hydrogen atoms were computed with the Lorentz-Berthelot mixing rules [158, 159],

$$
\epsilon_{ij} = \sqrt{\epsilon_{ii}\epsilon_{jj}} \qquad \sigma_{ij} = \frac{\sigma_{ii} + \sigma_{jj}}{2}. \tag{3.5}
$$

The C-H bond energy U_{Bo} and H-C-H angle energy U_θ within a molecule were modeled with harmonic potentials,

$$
U_{Bo}(r_{ij}) = \frac{k_0}{2}(r_{ij} - r_0)^2 \tag{3.6a}
$$

$$
U_\theta(\theta_{ijk}) = \frac{k_\theta}{2}(\theta_{ijk} - \theta_0)^2, \tag{3.6b}
$$

where k_0 and k_θ are the strengths of the bonds, r_0 and θ_0 are the equilibrium bond values, and θ_{ijk} is the angle between atoms i, j, and k. Note that TraPPE-EH places the hydrogen atoms at a distance of half the realistic bond length. Further details of

the methane model can be found in the literature [149].

Butane was modeled using the united atom TraPPE (TraPPE-UA) potential [149] which is a four particle model with two CH_3 pseudo particles at the edges of the hydrocarbon chain and two CH_2 pseudo particles in the center of the hydrocarbon chain. The CH_3 and CH_2 particles from different molecules interact through a smoothed Lennard Jones potential, Eq. 3.4, with Lorenz-Berthlot mixing rules, Eq. 3.5. The bond lengths and bending angles between the CH_j particles are also modeled with harmonic potentials, Eq. 3.6. The dihedral angle energy U_{di} in butane is modeled with the OPLS potential [160],

$$U_{di}(\phi) = c_1(1 + \cos(\phi)) - c_2(1 - \cos(2\phi)) + c_3(1 + \cos(3\phi)), \qquad (3.7)$$

where ϕ is the dihedral angle and c_1, c_2, and c_3 are energetic coefficients. Further details of the butane model can be found in the literature [148].

Methanol, TraPPE Methanol (CH_3OH) was simulated using TraPPE-UA potential [151]. This is a three particle model which explicitly models the O and H in the hydroxyl group and models the methyl group as a pseudo atom. The atoms and pseudo atoms from different molecules interact through a Lennard Jones potential and Coulombic potential

$$U_{ALC}(r_{ij}) = U_{12,6}^{LJ}(r_{ij}) + \frac{q_i q_j}{4\pi\epsilon_0 r_{ij}} \qquad (3.8)$$

with Lorentz-Berthelot mixing rules, Eq. 3.5. Both the bond lengths and angles are modeled with harmonic potentials, Eq. 3.6. The Lennard-Jones portion of the potential is truncated and shifted at r_c, and the long range Coulumbic interactions

are handled with the PPPM method. A more detailed discussion of the methanol model can be found in the literature [151].

Benzene, TraPPE Benzene (C_6H_6) modeled using TraPPE-EH potential [150]. The carbon and hydrogen from different molecules interact through a Lennard Jones potential and Coulombic potential

$$U_B(r_{ij}) = U_{12,6}^{LJ}(r_{ij}) + \frac{q_i q_j}{4\pi\epsilon_0 r_{ij}} \tag{3.9}$$

with Lorentz Berlthot mixing rules. The bond lengths and bond angles for benzene are harmonic, Eq. 3.6. The Lennard-Jones portion of the potential is truncated and shifted at r_c, and long range Coulumbic interactions are handled with a PPPM method. A more detailed discussion of the benzene model can be found in the literature [150].

3.2.2 Simulation Initialization

In order to verify the method to calculate α, planar simulations were run for each fluid and temperature simulated, but the overall initializing procedure for the planar liquid-vapor interfaces and the droplet liquid-vapor interfaces was similar. For all systems N molecules where placed in a simulation box of size $L \times W \times W$ for the planar interfaces simulations and $L \times L \times L$ for spherical interface simulations. Domain sizes for simulations are found in Tables 3.10 - 3.24. The number of molecules N and the domain sizes L and W were chosen based on the bulk densities of the fluids [148–150,154,154,162,163] such that a liquid region would be stable in the simulations (note that this method required some trial and error). A portion of the particles were placed in a simple lattice corresponding to the bulk liquid density ρ_L in the center of the

Table 3.1: Parameters used for inter-molecular potentials. Values for the Lennard Jones (LJ) and Buckingham (B) potentials are dimensionless.

Fluid	ϵ/k_B	σ	r_c	–	–	–
LJ $k = 12$	1	1	3	–	–	–
LJ $k = 9$	1.6875	1	3	–	–	–
B $k = 3$	0.375	1	3	–	–	–
B $k = 2$	0.5	1	3	–	–	–
Fluid	ϵ/k_B [K]	σ [Å]	r_c [Å]	r_{in} [Å]	q [e]	Model
Benzene, C	30.7	3.60	14	–	-0.095	TraPPE-EH [150]
Benzene, H	25.5	2.36	14	–	0.095	
Butane, CH_3	98.0	3.75	15	14	–	TraPPE-UA [148]
Butane, CH_2	46.0	3.95	15	14	–	
Methane, C	0.01	3.31	15	9	–	TRaPPE-EH [149]
Methane, H	15.3	3.31	15	9	–	
Methanol, CH_3	98.0	3.75	14	–	0.265	
Methanol, O	46.0	3.95	14	–	-0.700	TraPPE-UA [151]
Methanol, H	0	0	–	–	0.435	
Water, O	93.2	3.1589	10	–	-1.1128	TIP4P/2005 [152]
Water, H	0	0	–	–	0.5564	

domain while the remaining molecules were placed in a simple lattice corresponding to the bulk vapor density ρ_V throughout the remainder of the domain. The system was then run, melting the lattices and forming distinct liquid and vapor regions. Note that during the first portion of initialization a smaller Δt was used due to the highly unfavorable initial configuration. The simulations continued equilibration at a normal time step Δt until the interface stabilized such that the interface position was not changing with time. The number of time steps needed for the interface to stabilize depended on the droplet size and fluid being modeled. In order to ensure the droplet were at an equilibrium position, the radius was monitored during the initialization. Figure 3.2 shows the stable interfaces for a select few systems. Once

Table 3.2: Bond length and bond stiffness for intra-molecular energies. The bond stretching energy is modeled with a harmonic potential, $U_{Bo}(r_{ij}) = k_0(r_{ij} - r_0)^2/2$.

Fluid	Bond	r_0 [Å]	Source	k_0/k_B [K/Å²]	Source
Benzene	C-C	1.392	[150]	236010	[161]
Benzene	C-H	1.08	[150]	184681	[161]
Butane	CH_3-CH_2	1.54	[148]	155998	[148]
Methane	C-H	0.55	[149]	171094	[161]
Methanol	CH_3-O	1.43	[151]	226449	[161]
Methanol	O-H	0.945	[151]	278280	[161]
Water	O-H	0.9572	[152]	rigid (∞)	[152]

Table 3.3: Bond angles and bond angle stiffness for intra-molecular energies. The bond angle energy is modeled with a harmonic potential, $U_\theta(\theta_{ijk}) = k_\theta(\theta_{ijk} - \theta_0)^2/2$.

Fluid	Bond	θ_0 [°]	Source	k_θ/k_B [K/rad²]	Source
Benzene	C-C-C	120	[150]	17613	[161]
Benzene	C-C-H	120	[150]	31703	[161]
Butane	CH_3-CH_2-CH_2	114.0	[148]	62500	[148]
Methane	H-C-H	109.47	[149]	17613	[161]
Methanol	CH_3-O-H	108.5	[151]	55400	[161]
Water	H-O-H	104.52	[152]	rigid (∞)	[152]

Table 3.4: Dihedral angle coefficients for butane. The dihedral angle is modeled using $U_{di}(\phi) = c_1(1 + \cos(\phi)) - c_2(1 - \cos(2\phi)) + c_3(1 + \cos(3\phi))$. Units for each coefficient are in [K].

c_1/k_B	c_2/k_B	c_3/k_B	Source
355.03	68.19	791.32	[148]

Table 3.5: Time step Δt, total run time after equilibration t_{total}, number of particles/molecules in thermostatted regions N_T, damping constant for Langevin thermostat τ_T, PPPM tolerance, and SHAKE tolerance. Values for the Lennard Jones (LJ) and Buckingham (B) potentials are in dimensionless units.

	Δt	t_{total}	N_T	–	–	–
LJ $k = 12$	0.005	25000	100	–	–	–
LJ $k = 9$	0.005	25000	100	–	–	–
B $k = 3$	0.005	8500†	100	–	–	–
B $k = 2$	0.005	12500†	100	–	–	–
	Δt [fs]	t_{total} [ns]	N_T	τ_T [ns]	PPPM Tol.	SHAKE Tol.
Benzene	2	1.9†	100	0.1	10^{-5}	–
Butane	2	9.0†	100	0.1	–	–
Methane	2	4.2†	100	0.1	–	–
Methanol	2	3.0†	100	0.1	10^{-5}	–
Water	2	3.4†	100	0.1	10^{-5}	10^{-4}

† Minimum run time, several simulations were run longer.

the average radius fluctuated about a constant value, calculations for α began. The interface position is defined as the location where the density is the average of the bulk liquid and vapor density, $\rho(x_{int}) = (\rho_L + \rho_V)/2$.
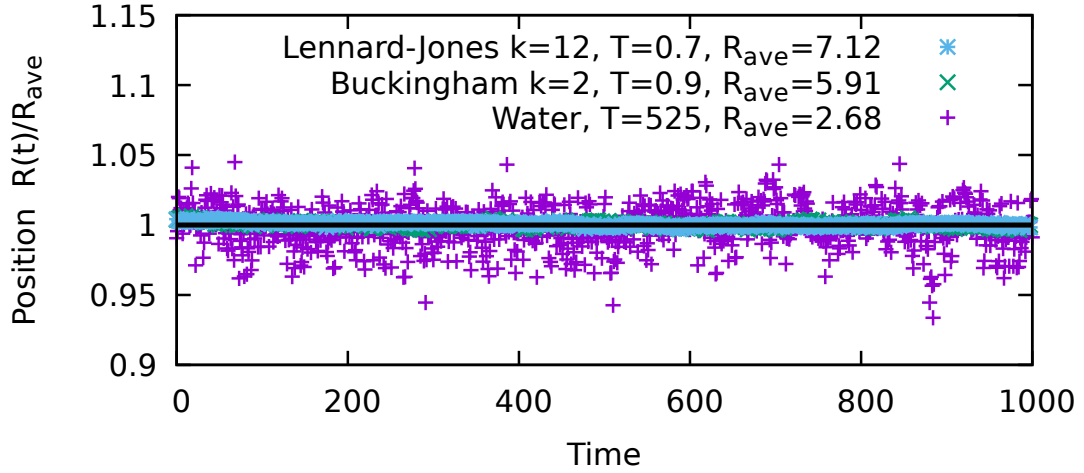
Fig. 3.2: Normalized droplet radius versus time for a select few systems. Values for the Lennard-Jones and Buckingham systems are dimensionless while the values of water for time, temperature, and radius are in [ps], [K], and [nm] respectively.

Velocity rescaling thermostats were used to maintain the temperature T of the domain for the Lennard-Jones and Buckingham fluids while Langevin thermostats [91] with damping constant τ_T were used for the remaining systems. Local thermostats were used to control the temperature far from the interface (center of the liquid film/droplet and edges of the vapor region) such that the thermostats would have minimal impact on interfacial dynamics. The size of the local thermostats were such that roughly N_T molecules were being thermostatted. To prevent the liquid from slowly translating throughout the domain the position of every particle was shifted at the end of every time step such that the center-of-mass of the liquid was at the origin. If a molecule's instantaneous pairwise potential energy $U_i(t)$ was less than $(U_L + U_V)/2$ it was tagged as a liquid particle otherwise it was tagged as vapor. Here U_L and U_V are the average potential energy per molecule of the bulk liquid and vapor. Thermostat information, time step, and run time information can be found in Table 4.2 while bulk liquid and bulk vapor densities can be found in Tables 3.6 and 3.7.

Table 3.6: Bulk liquid and vapor densities for the Lennard Jones and Buckingham potentials. Values are in dimensionless units.

Fluid	T	ρ_L	ρ_V
LJ $k = 12$	0.6	0.8601 ± 0.0152	0.0010 ± 0.0002
LJ $k = 12$	0.7	0.8150 ± 0.0151	0.0039 ± 0.0004
LJ $k = 12$	0.8	0.7669 ± 0.0151	0.0112 ± 0.0007
LJ $k = 12$	0.9	0.7132 ± 0.0150	0.0257 ± 0.0011
LJ $k = 12$	1.0	0.6500 ± 0.0151	0.0528 ± 0.0021
LJ $k = 9$	0.9	0.7606 ± 0.0152	0.0092 ± 0.0006
LJ $k = 9$	1.2	0.6178 ± 0.0151	0.0612 ± 0.0023
B $k = 3$	0.7	1.0768 ± 0.0167	0.0131 ± 0.0007
B $k = 3$	0.8	0.9897 ± 0.0168	0.0395 ± 0.0240
B $k = 2$	0.9	1.1099 ± 0.0170	0.0237 ± 0.0280
B $k = 2$	1.1	0.9596 ± 0.0173	0.0883 ± 0.0537

To further confirm that the droplets are in an expected equilibrium state, the droplet radius can be calculated as a function of the actual vapor density ρ_V by [164]

$$R = \frac{2\sigma_\infty}{k_B T} \left(\rho_L^\infty \ln \left(\frac{\rho_V}{\rho_V^\infty} \right) - (\rho_V - \rho_V^\infty) \right)^{-1} \qquad (3.10)$$

where σ_∞, ρ_L^∞, and ρ_V^∞ are the surface tension and saturation bulk densities for the liquid and vapor phases. Equation 3.10 is derived from the Gibbs-Duhem equation at constant temperature, $\rho d\mu = dP$ where μ and P are the chemical potential and pressure, with the assumptions that the fluid is incompressible and the gas is ideal. Furthermore the Kelvin equation can be recovered from Eq. 3.10 under the assumption $\rho_L^\infty \gg \rho_V^\infty$. Figure 3.3 compares Eq. 3.10 with the MD data for the Lennard Jones and Buckingham fluids while Fig. 3.4 compares the real fluids. Note that the lower temperatures tend to agree with the analytical equation. This is expected because as the system approaches the critical point the liquid density decreases and the

Table 3.7: Bulk liquid and vapor densities for the benzene, butane, methane, methanol, and water.

Fluid	T [K]	ρ_L [g/cm^3]	ρ_V [g/cm^3]
Benzene	365	0.7538 ± 0.0296	0.0109 ± 0.0036
Benzene	415	0.6716 ± 0.0358	0.0395 ± 0.0182
Butane	295	0.5560 ± 0.0254	0.0122 ± 0.0021
Butane	325	0.5117 ± 0.0286	0.0265 ± 0.0060
Butane	360	0.4457 ± 0.0351	0.0604 ± 0.0157
Methane	120	0.3850 ± 0.0128	0.0089 ± 0.0009
Methane	135	0.3510 ± 0.0146	0.0212 ± 0.0026
Methane	150	0.3029 ± 0.0176	0.0497 ± 0.0087
Methanol	325	0.6612 ± 0.0269	0.0012 ± 0.0001
Methanol	375	0.5996 ± 0.0296	0.0089 ± 0.0023
Water	500	0.7952 ± 0.0365	0.0092 ± 0.0020
Water	525	0.7562 ± 0.0389	0.0156 ± 0.0040
Water	550	0.7087 ± 0.0423	0.0262 ± 0.0077
Water	575	0.6507 ± 0.0476	0.0460 ± 0.0170
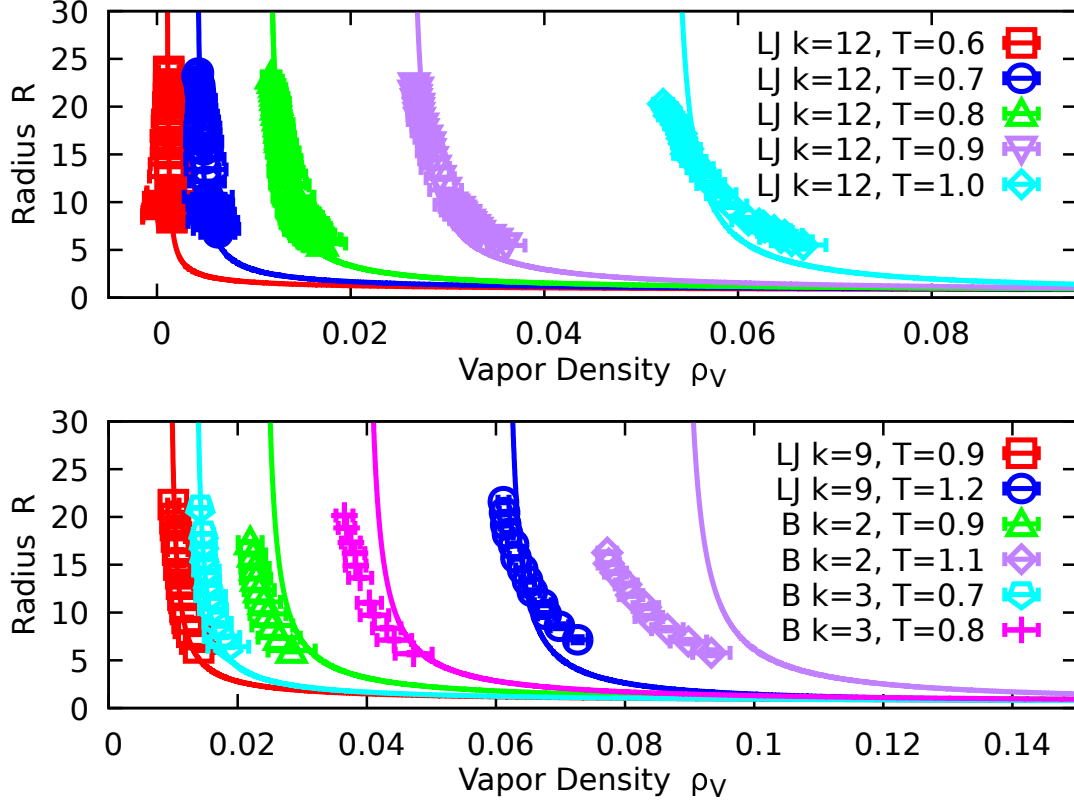
Fig. 3.3: Droplet radius versus vapor density for (top) Lennard Jones with $k = 12$ (bottom) Lennard Jones with $k = 9$ and Buckingham potentials. Solid lines are Eq. 3.10 where the values for σ_∞, ρ_L^∞, and ρ_V^∞, are taken from planar simulations. All values are given in dimensionless units.

vapor density increases, making the liquid more compressible and the gas less ideal, violating the assumptions in Eq. 3.10.
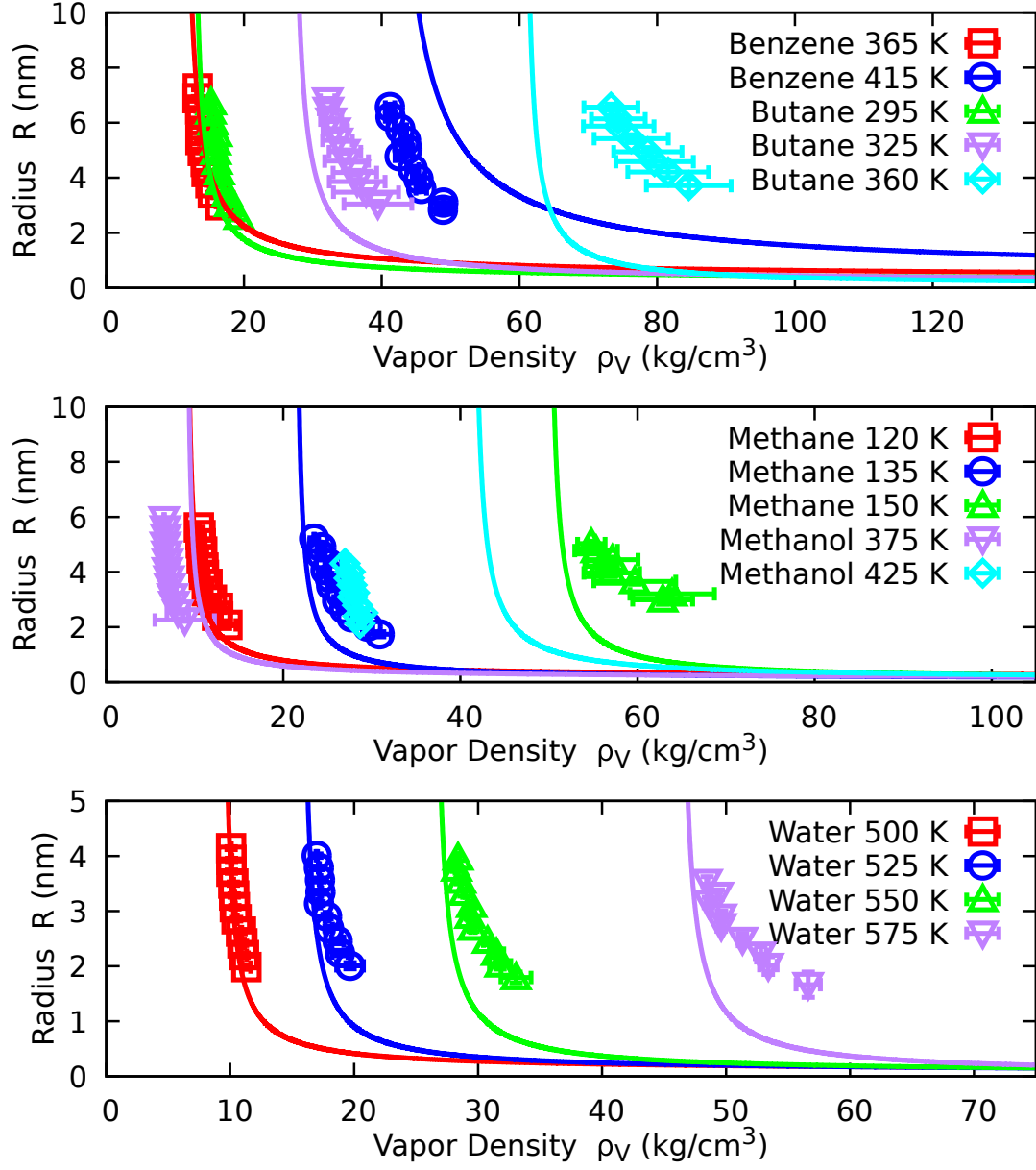
Fig. 3.4: Droplet radius versus vapor density for (top) benzene and butane, (middle) methane and methanol, and (bottom) water. Solid lines are Eq. 3.10 where the values for σ_∞, ρ_L^∞, and ρ_V^∞, are taken from planar simulations.

3.2.3   Mass Accommodation Coefficient Calculation Method

After establishing stable droplets, canonical ensemble MD simulations were then run to calculate α. Formally α is the ratio of the number of accommodated molecules N_{acc} to the number of incident molecules N_{inc},

$$\alpha = \frac{N_{acc}}{N_{inc}} = \frac{1 - N_{ref}}{N_{inc}} \tag{3.11}$$

where N_{ref} is the number of reflected molecules. Here, N_{inc} was determined by calculating the number of molecules moving toward the droplet that crossed a hypothetical surface denoted the 'incident surface'. As in previous accommodation coefficient studies [4, 130, 131], the incident surface was placed at a distance $\delta = r_c$ beyond the liquid-vapor interface, where r_c is the MD cutoff radius (Table 3.9). The cutoff radius was chosen for δ because that is when the liquid begins to have an energetic impact on the vapor molecule and the when the "collision" between the vapor molecule and liquid droplet begins. After the center of mass of a molecule crossed the incident surface it was monitored until it recrossed the incident surface or was accommodated by the liquid. If the center of mass of the incident molecule remained inside the liquid region, defined as the interior of the droplet radius (inside blue circle in Fig. 3.1), for a time τ_{acc} it was marked as accommodated. Similar to the method of Liang *et al.* [4], τ_{acc} is the time it would take a molecule of mass m to travel 2δ if it were traveling at the thermal speed $v_{th} = \sqrt{k_B T / 2\pi m}$ [72]. The values for τ_{acc} are in Table 3.9.

3.2.4 Interface Width Calculation

A common interface profile for molecular fluids is [165]

$$\rho(x) = \frac{\rho_L + \rho_V}{2} - \frac{\rho_L - \rho_V}{2} \tanh\left(\frac{2(x - x_0)}{\sqrt{2}L_{int}}\right) \tag{3.12}$$

where ρ_L and ρ_V are the bulk liquid and vapor density, L_{int} is a measure of the interface width, and x_0 is the interface location. The values for L_{int} were found by fitting Eq. 4.6 to the planar liquid-vapor interfaces.

3.2.5 Calculation of the Critical Temperatures

The most common method to extract the critical temperature T_c from molecular simulations is to use the rectilinear diameter equation [166–168]

$$\rho_L - \rho_V = k_T \left(1 - \frac{T}{T_c}\right)^b \tag{3.13}$$

where ρ_L and ρ_V are the liquid and vapor densities of the fluids for a planar interface, k_T is a fitting parameter, and $b = 0.32$ is the critical exponent. Similarly the the critical density ρ_c can be found using

$$\rho_L + \rho_V = 2\rho_c + k_\rho \left(1 - \frac{T}{T_c}\right) \tag{3.14}$$

where k_ρ is a fitting parameter. Table 3.8 shows the calculated critical properties using Eqs. 3.13 and 3.14 where the values are fit to the data in the least squares sense [169]. Figure 3.5 shows the coexistence curves calculated by combining Eq. 3.13 and Eq. 3.14 (lines) along with the MD data (markers).
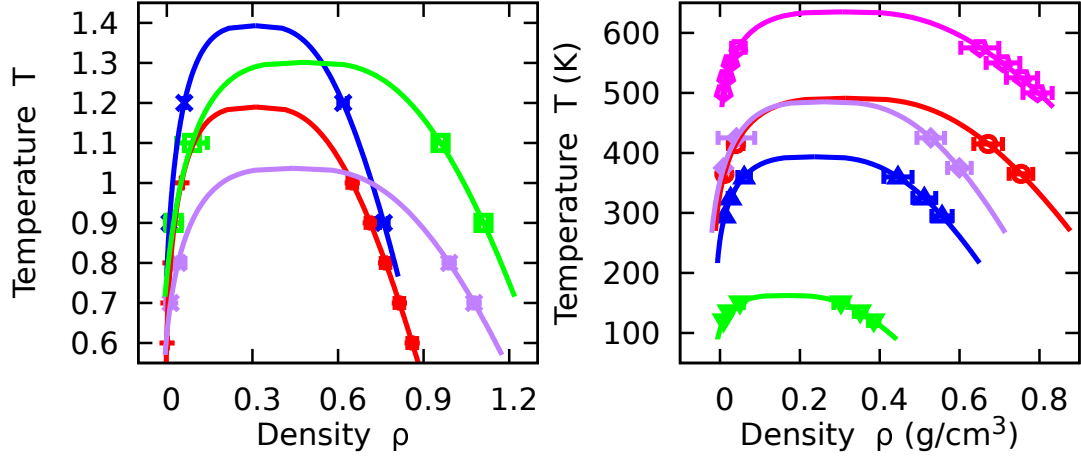
Fig. 3.5: (Left) Coexistence curves for the Lennard Jones $k = 12$ (red), Lennard Jones $k = 9$ (blue), Buckingham $k = 3$ (purple), and Buckingham $k = 2$ (green) fluids. Values are in dimensionless units. (Right) Coexistence curves for the benzene (red), butane (blue), methane (green), methanol (purple), and water (magenta).

Table 3.8: Critical parameters for fluids from Eqs. 3.13 and 3.14. Note that the values for Lennard-Jones (LJ) and Buckingham (B) potentials are dimensionless. No errors are estimated for several fluids because the number of free parameters was the same as the number of data points.

Fluid	T_c	ρ_c	k_T	k_ρ
LJ $k = 12$	1.190 ± 0.003	0.312 ± 0.001	1.078 ± 0.002	0.473 ± 0.008
LJ $k = 9$	1.393	0.310	1.048	0.422
B $k = 3$	1.302	0.481	1.583	0.558
B $k = 2$	1.037	0.443	1.525	0.630
Fluid	T_c [K]	ρ_c [g/cm^3]	k_T [g/cm^3]	k_ρ [g/cm^3]
Benzene	491.2	0.315	1.148	0.526
Butane	393.6 ± 0.5	0.236 ± 0.001	0.847 ± 0.002	0.380 ± 0.010
Methane	162.4 ± 0.8	0.167 ± 0.001	0.579 ± 0.005	0.226 ± 0.006
Methanol	485.3	0.261	0.949	0.383
Water	635.1 ± 2.9	0.307 ± 0.002	1.294 ± 0.010	0.905 ± 0.024

3.2.6 Surface Tension and Tolman Length Calculations

It is a well known phenomena that the surface tension for small droplets differs from the bulk planar value and can be corrected by the Tolman length δ_T [141–147]. The size dependence surface tension becomes

$$\sigma(R) = \sigma_\infty \left(1 - \frac{2\delta_T}{R} \right) \tag{3.15}$$

where σ_∞ is the surface tension for a planar interface. The Young-Laplace equation becomes

$$\Delta P \equiv P_L - P_V = \frac{2\sigma_\infty}{R} \left(1 - \frac{\delta_T}{R} \right) \tag{3.16}$$

where P_L and P_V are the bulk liquid and vapor pressures. Figure 3.6 plots Eq. 3.16 where δ_T was fit in the least squares senses [169] and shows excellent agreement between Eq. 3.16 and the MD data. The fitted values of δ_T compared well with values found in the literature [142–144, 146, 147]. The surface tension σ_∞ was found by integrating the pressure profiles on the planar interfaces [85],

$$\sigma_\infty = \int P_N(x) - P_T(x) dx \tag{3.17}$$

where P_N and P_T are the normal and transverse pressures, and the limits of the integral are taken far into the bulk regions.
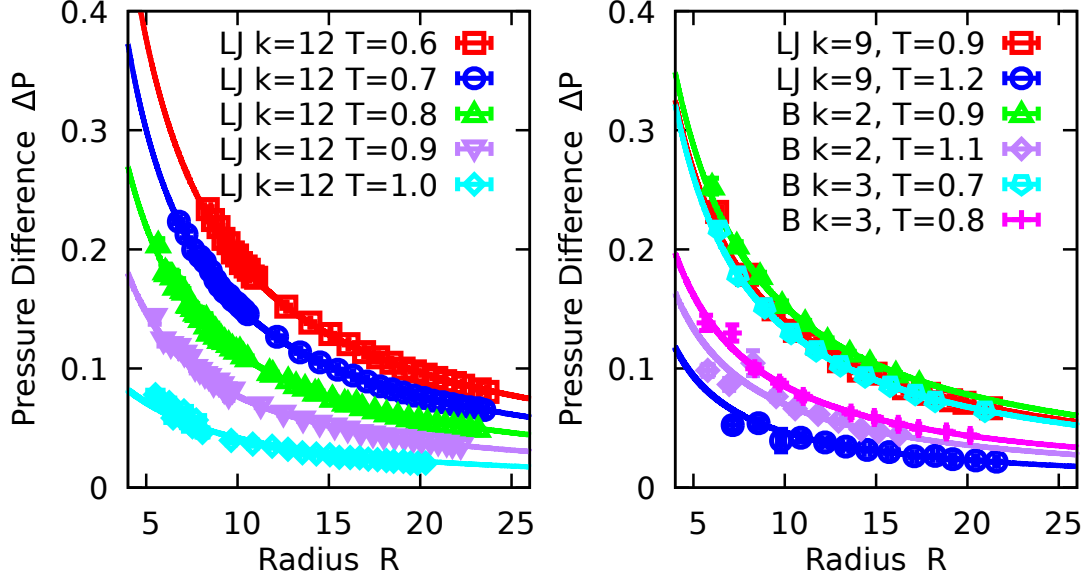
Fig. 3.6: Pressure difference ΔP versus droplet radius for the (left) Lennard-Jones potential with $k = 12$ and (right) the Lennard-Jones potential with $k = 9$ and the Buckingham potentials. Markers are MD data, while solid lines are Eq. 3.16 with the fitted value of δ_T. All values are in dimensionless units and the value for σ_∞ is taken from planar simulations.

3.3   Results

3.3.1   Planar Validation

In order to verify the viability of the method used to calculate α, it was first applied to planar liquid-vapor interfaces to calculate α_{pla}. Molecules not tagged as accommodated molecules as described previously are tagged as reflected. A typical ratio of N_{acc}/N_{inc} and N_{ref}/N_{inc} as a function of time are shown in Fig. 3.7(left). The probability of a molecule accommodating or reflecting as of function of time, P_{acc} and P_{ref}, can be found by integrating N_{acc}/N_{inc} and N_{ref}/N_{inc} respectively, Fig. 3.7(right). The method of marking accommodated molecules allows for the number of reflected molecules as a function to time to reach zero even with a finite sized liquid region. This removes the need for the somewhat arbitrary integration time seen in
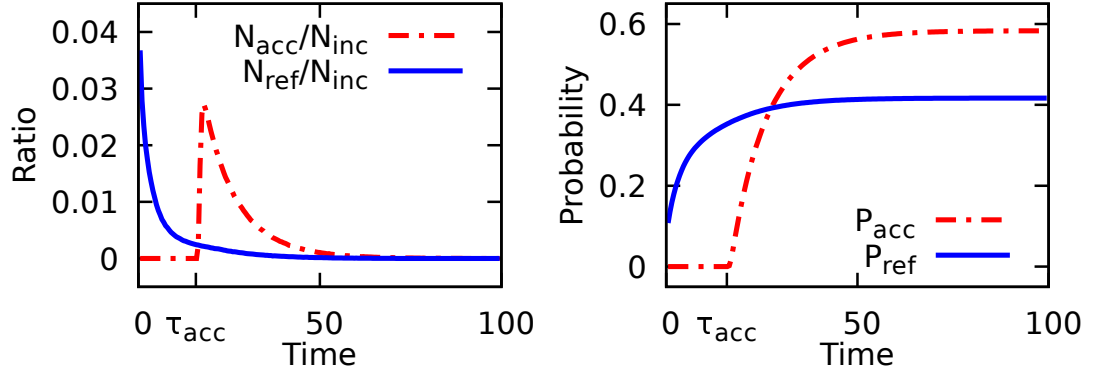
Fig. 3.7: Ratio of the (left) number of accommodated and reflected particles of the number of incident particles and (right) probabilities corresponding to the integral of N_{acc}/N_{inc} and the integral of N_{ref}/N_{inc} for the Lennard Jones system with $k = 12$ and $T = 0.9$. The time is given in dimensionless units.

Liang *et al.* [4]. The probabilities were integrated in order to calculate α and the results agree well with previous literature [1–4] as seen in Fig. 3.8. Note that using N_{ref} as opposed to N_{acc} in Eq. 3.11 yields similar results.

3.3.2 Curvature Results

With the validity of the method established, it was then applied to calculate α for spherical droplets. Figure 3.9(a) shows α as a function of droplet radius for the Lennard-Jones $k = 12$ potential at $T = 96.8$ K, which clearly shows that α decreases as droplet radius decreases. This decreasing trend is due to several effects both physical and geometric in nature. Physically vapor density increases as the droplet size decreases, in agreement with the Kelvin equation for incompressible liquid and ideal gas, resulting in an increased number of incident particles since $N_{inc} \sim \rho_V$ [1, 4, 134]. Figure 3.9(b) shows that the inverse of the normalized vapor density, $\rho_V^* = \rho_V/\rho_V^\infty$ where ρ_V^∞ is the vapor density for a planar interface, decreases with droplet size contributing to the decrease in α. The vapor density in Fig. 3.9(b)

49
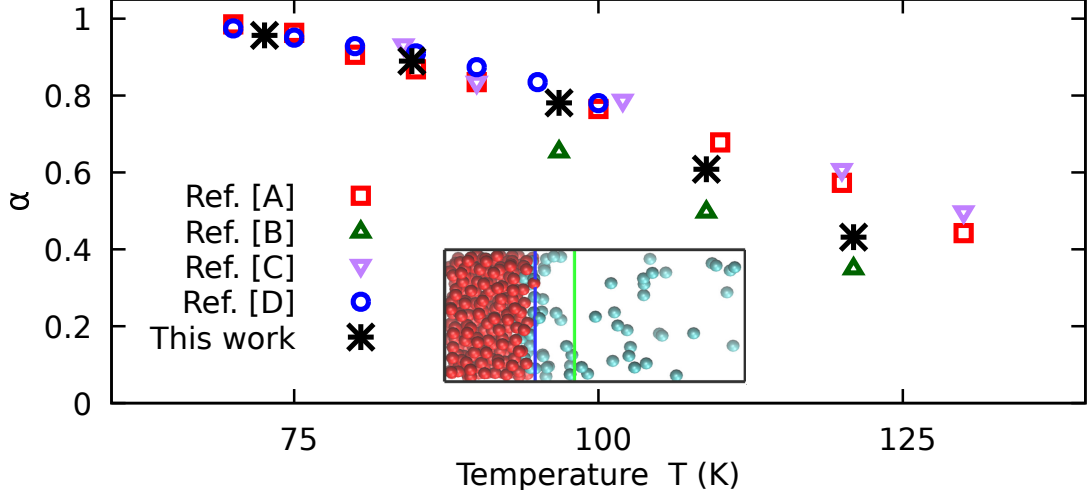
Fig. 3.8: (a) Mass accommodation coefficient calculated in planar simulations versus temperature for the Lennard-Jones potential with $k = 12$. References are Ref. [A] is Ref. [1], Ref. [B] is Ref. [2], Ref. [C] is Ref. [3], and Ref. [D] is Ref. [4].

agrees well with the Kelvin equation prediction (solid line), but this was not the case for all fluids simulated.

Furthermore, the number of accommodated molecules N_{acc} is expected to scale with the energetic attraction between an incident vapor molecule and the liquid drop U_D which was found by averaging the effective vapor-droplet interaction energy from Yasuoka *et al.* [170] within the incident region. Assuming the attractive portion of the Lennard-Jones potential with $k = 12$, the interaction U_d of a liquid droplet of radius R at uniform density ρ_L and a vapor molecule at a distance r from the center of the drop is [170]

$$U_d(r, R) = -\frac{16\pi\rho_L}{3}\frac{R^3}{(R^2 - r^2)^3}.$$ (3.18)

Integrating this equation from the incident surface to the molecular separation between the vapor molecule and the liquid droplet is how the average energetic potential U_D was found,

$$U_D(R) = \frac{1}{\delta - \sigma}\int_{R+\sigma}^{R+\delta} U_d(r, R)dr.$$ (3.19)

50
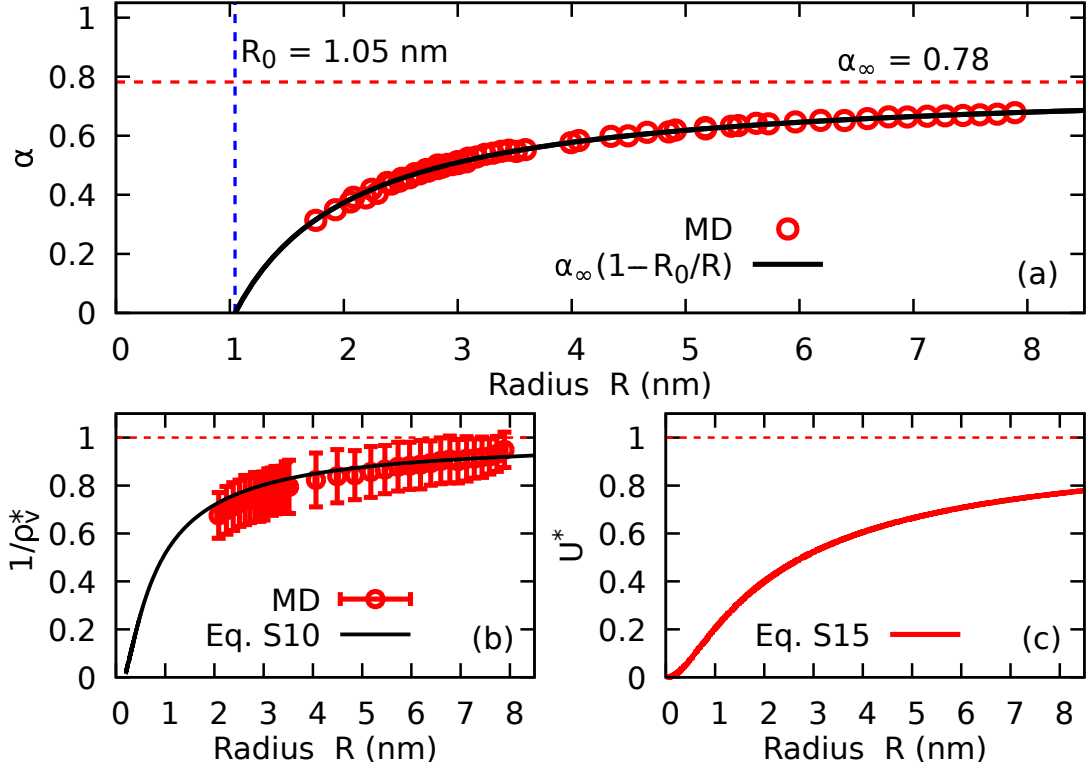
Fig. 3.9: (a) Inverse of normalized vapor density ρ_V^*, (b) normalized droplet attraction energy U^*, and (c) mass accommodation coefficient α versus droplet radius for the Lennard-Jones potential with $k = 12$ and $T = 96.8$ K. Dashed horizontal lines are limiting values for a planar interface. Error bars that are not shown are similar to marker size.

This result was then normalized by the value for a planar interface in order to calculate U^* with

$$U^*(R) = \frac{U_D(R)}{U_D(\infty)}. \tag{3.20}$$

Note that using this above approach for the realistic fluids would be more challenging due to the multiple inverse sixth power potentials for a given molecule [171]. Figure 3.9(c) shows that the normalized attraction U^* decreases with droplet size further contributing to the diminishing value for α with decreasing droplet radius.

The trend of the MD data based on the combined physical and geometric effects

in Fig. 3.9(a), suggests a functional form for α as follows,

$$\alpha(R) = \alpha_\infty \left(1 - \frac{R_0}{R} \right) \tag{3.21}$$

where α_∞ is the accommodation coefficient for an infinitely large drop and R_0 is a normalizing radius. This functional form was seen for all fluids and temperatures simulated in this study and the MD data collapses onto a master curve in Fig. 3.10. Note that the data in Fig. 3.10 is normalized for each fluid and temperature, and the normalizing values for α_∞ and R_0 can be found in Table 3.9. The physical meaning of α_∞ is simple to understand as it is the accommodation coefficient for a planar interface, which was confirmed in planar simulations. For an infinitely large droplet (a planar interface) the Eq. 3.21 reduces to α_∞ implying that the fitted α_∞ and calculated value α_{pla} should be consistent. Figure 3.11 confirms that within error the fitted value of α_∞ and the calculated value of α_{pla} are indeed consistent. Similar to the decreasing temperature trend seen in Fig. 3.9(a), a decreasing trend with temperature was seen for α_∞ which is consistent with the literature [1–4, 136–138].

The physical intuition for R_0, however, is harder to grasp. From Eq. 3.21, R_0 is the droplet radius at which no particles will accommodate onto the droplet. Figure 3.12(a) shows that R_0 increases as the temperature approaches the critical temperature T_c. This indicates that R_0 increases as thermal fluctuations cause larger deformations of the interface causing an effective increase in the droplet radius, making droplets appear larger than they actually are. Figure 3.12(b) shows that R_0 increases fairly linearly with interfacial width L_{int} which supports that R_0 is a measure of the effective "shadow" that a droplet of a particle fluid at a given temperature casts.

Table 3.9: Parameters for curved droplet simulations. Value in (.) indicates uncertainty in the preceding digit(s), i.e. $1.23(4) = 1.23 \pm 0.04$.

Fluid	T [K]	δ [nm]	τ_{acc} [ps]	α_∞ [-]	R_0 [nm]
Lennard-Jones $k = 12$	72.6	1.02	41.67	1.019(7)	0.82(3)
Lennard-Jones $k = 12$	84.7	1.02	38.58	0.919(1)	0.843(6)
Lennard-Jones $k = 12$	96.8	1.02	36.09	0.782(1)	1.045(5)
Lennard-Jones $k = 12$	108.9	1.02	34.02	0.595(1)	1.242(6)
Lennard-Jones $k = 12$	121.0	1.02	32.28	0.418(2)	1.62(2)
Lennard-Jones $k = 9$	108.9	1.02	34.02	0.848(2)	0.977(8)
Lennard-Jones $k = 9$	145.1	1.02	29.46	0.395(2)	1.68(1)
Buckingham $k = 3$	84.7	1.02	38.58	0.801(1)	0.98(5)
Buckingham $k = 3$	96.8	1.02	36.09	0.593(3)	1.18(1)
Buckingham $k = 2$	108.9	1.02	34.02	0.783(1)	1.012(4)
Buckingham $k = 2$	133.1	1.02	30.77	0.453(3)	1.42(1)
Benzene	365	1.40	35.61	0.756(7)	1.49(2)
Benzene	415	1.40	33.39	0.43(2)	2.15(7)
n-Butane	295	1.50	36.61	0.395(7)	1.82(4)
n-Butane	325	1.50	34.88	0.327(9)	2.2(6)
n-Butane	360	1.50	33.14	0.152(5)	2.79(7)
Methane	120	1.50	30.15	0.621(8)	1.53(2)
Methane	135	1.50	28.43	0.37(1)	1.63(5)
Methane	150	1.50	26.97	0.166(4)	2.29(4)
Methanol	375	1.40	22.50	0.631(5)	0.81(2)
Methanol	425	1.40	21.13	0.408(6)	1.15(3)
Water	500	1.00	10.44	0.278(5)	1.04(3)
Water	525	1.00	10.18	0.228(3)	1.04(2)
Water	550	1.00	9.95	0.169(4)	1.24(3)
Water	575	1.00	9.73	0.101(2)	1.28(3)
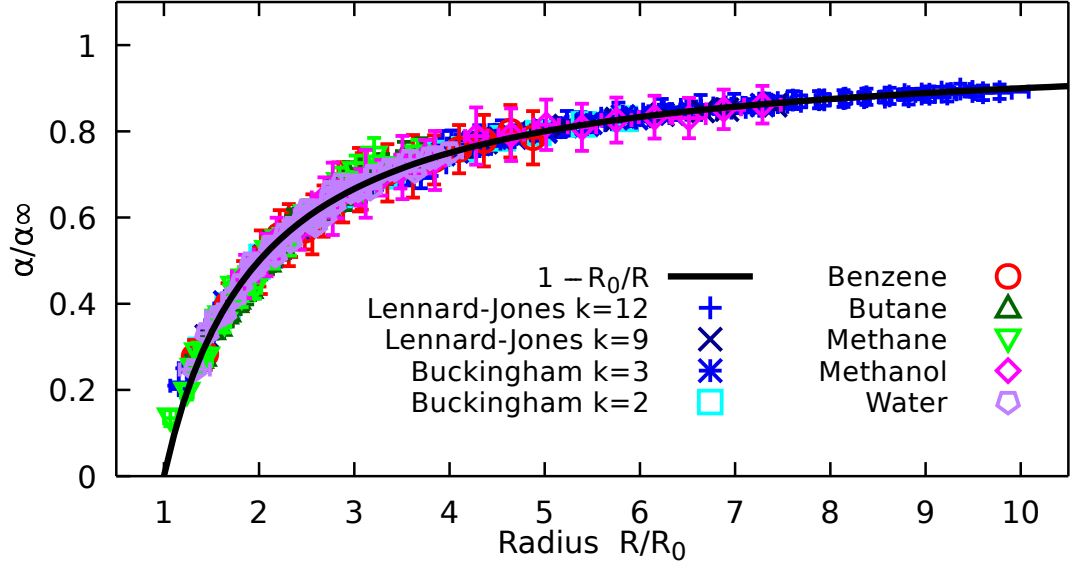
Fig. 3.10: Normalized radius versus normalized mass accommodation coefficient. Data is normalized by α_∞ and R_0, Table 3.9. Error bars not shown are similar to marker size.

The size dependent surface tension equation, Eq. 3.15, and the accommodation coefficient equation, Eq. 3.21, have similar forms. Therefore, there could be a potential link between δ_T and R_0. Figure 3.13 shows the R_0 as a function of δ_T for the Lennard-Jones and Buckingham fluids, and no clear relationship exists between δ_T and R_0. With no clear relation between δ_T and R_0, correlation between with the surface tension were examined and are shown in Fig. 3.14 for all fluids modeled. A lose decreasing trend in R_0 is seen with increasing surface tension and is similar to the trend seen for with T/T_c because surface tension decreases with increasing temperature [2, 148–154, 157, 162, 163].
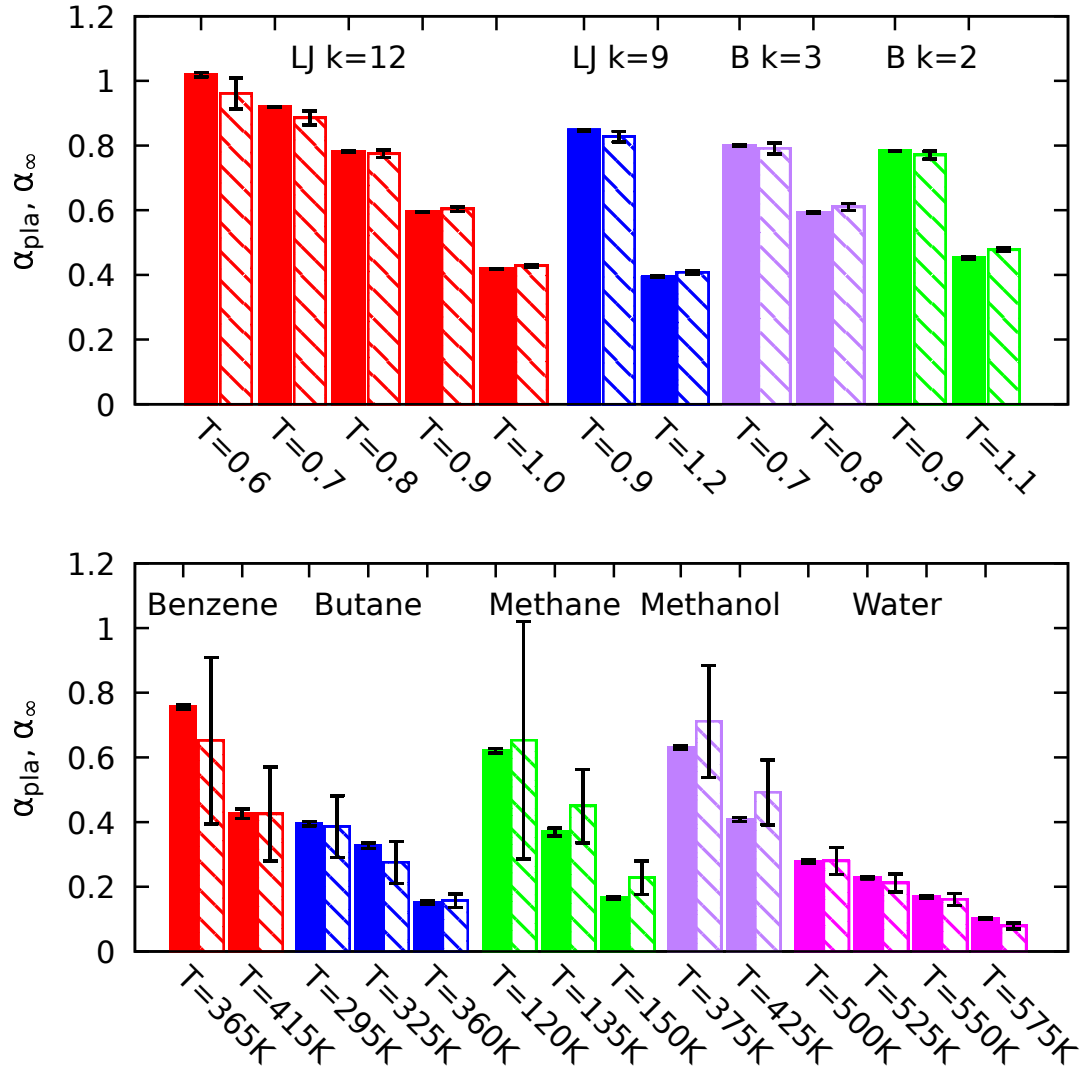
Fig. 3.11: Mass accommodation coefficient from the fitted value of α_∞ (solid) and calculated in the planar simulations α_{pla} (lines). Temperatures for the Lennard-Jones (LJ) and Buckingham (B) potentials (top) are given in dimensionless units.
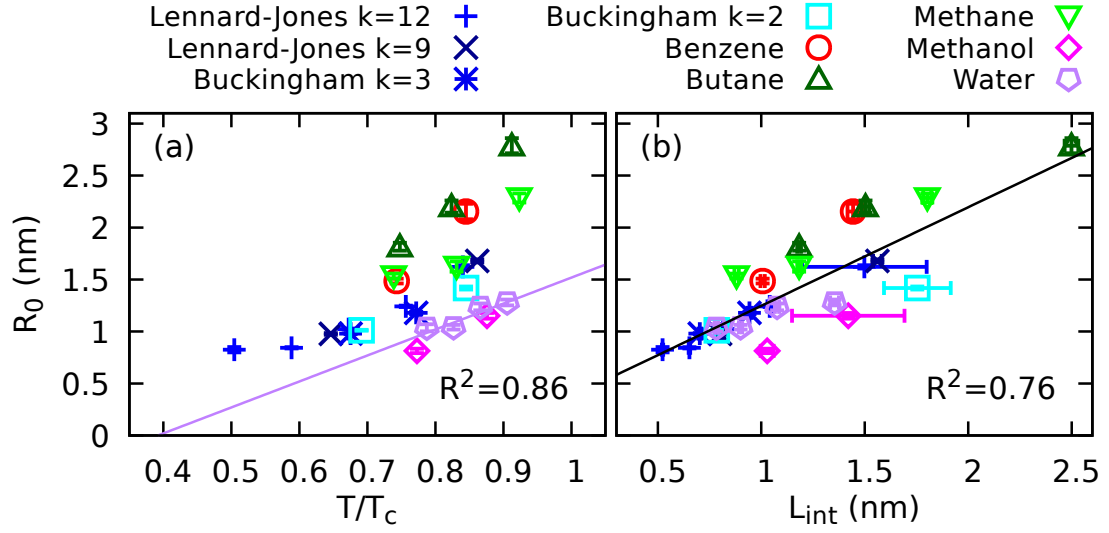
Fig. 3.12: Normalizing droplet radius versus (a) fraction of critical temperature and (b) interface width. Error bars that are not shown are similar to marker size. Solid line in (a) is a linear fit of water data with slope and intercept of 2.50 ± 0.71 nm and -0.98 ± 0.61 nm respectively. Solid line in (b) is a linear fit to all of the data with slope and intercept of 0.95 ± 0.14 and 0.30 ± 0.13 nm respectively. R^2 values are shown in figure.
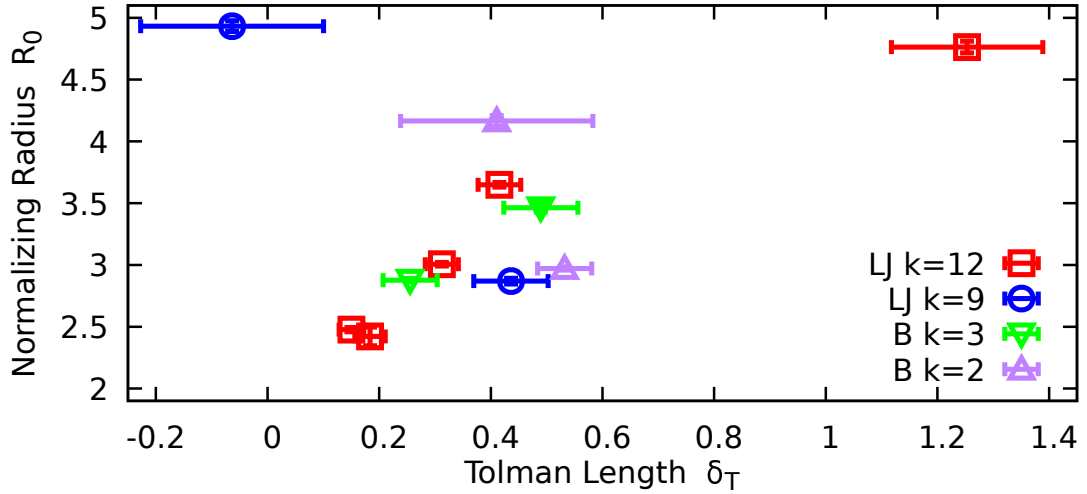
Fig. 3.13: Normalizing radius R_0 as a function of Tolman length δ_T for the Lennard Jones and Buckingham fluids. Values are in dimensionless units.
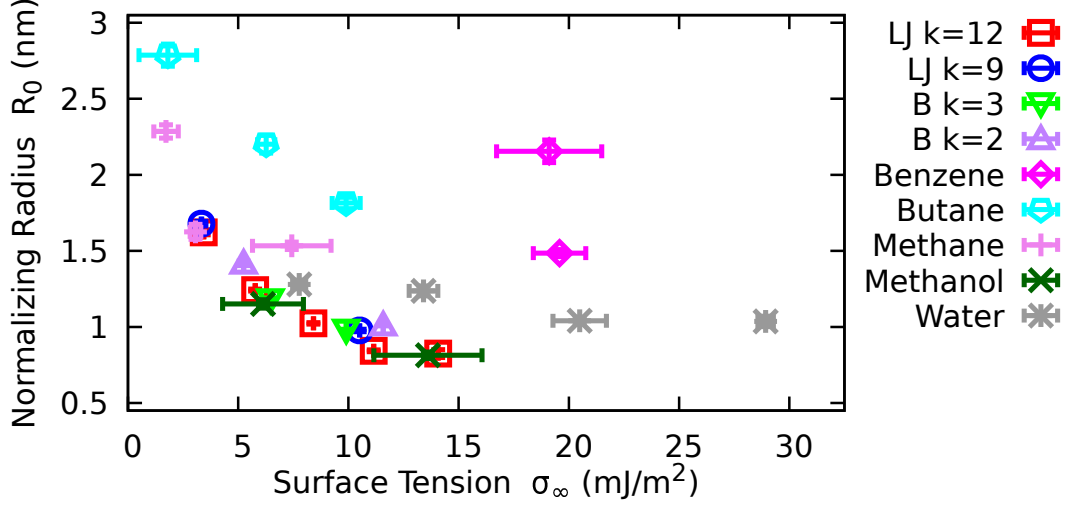
Fig. 3.14: Normalizing radius R_0 as a function of bulk surface tension σ_∞.

From Eq. 3.21 the accommodation coefficient for large droplets approaches the planar value α_∞. Defining R^* as the droplet radius where the accommodation coefficient is 95% of its planar value allows conclusions to be made about when the curvature dependence of α can be safely neglected. Values for R_0 range from 0.82 nm to 2.79 nm for the fluids in this work, resulting in values of $R^* = 16.4$ nm and $R^* = 55.8$ nm respectively. Therefore for droplets of the fluids modeled in this work with radii larger than ~ 55 nm, the curvature effect on α can be safely ignored. Furthermore this offers an explanation for why Julin *et al.* did not see curvature dependence for their 2 nm and 4 nm droplets for water at 273.15 K. Extrapolating the linear fit for the normalizing radius for water, solid line in Fig. 3.12(a), results in $R^* = 1.91$ nm for water at 273.15 K. The radii simulated by Julin *et al.* were equal to or larger than R^*, thereby offering an explanation the lack of curvature dependence in their work.

Summarizing, molecular dynamics simulations have shown that for a variety of fluids ranging from simple point particles to complex fluids the mass accommodation

coefficient is dependent on droplet size. This decreasing trend in α is supported by the increased vapor density for small droplets and the decreased attraction between an incident vapor molecule and the liquid droplet as the droplet radius decreases. This size dependence appears to be universal when the droplet size is scaled by the appropriate normalizing radius R_0 and planar mass accommodation coefficient α_∞. The dependence on droplet radius is of importance for droplets with radii smaller than ~ 55 nm for the fluids and temperature modeled in this work. The dependence mirrors the curvature dependence of surface tension but the normalizing radius found for the mass accommodation coefficient does not correlate with the Tolman length. Incorporating this curvature dependence into continuum models for the liquid-vapor interfacial resistance for small droplets could lead to increased accuracy in these models allowing for better agreement between analytical models and experimental results for small droplets. Future work could be to examine whether this curvature dependence holds in the presence of non-condensible gases, for fluid mixtures, if surface surfactants are present, or for actively condensing droplets.

3.4 Data Tables

Table 3.10: Number of particles N, domain length L, domain width W for planar simulations. Values for the Lennard-Jones and Buckingham potentials are dimensionless.

Fluid	T	N	L	W
Lennard-Jones $k = 12$	0.6	180000	12599.7	81.1
Lennard-Jones $k = 12$	0.7	180000	3648.8	81.1
Lennard-Jones $k = 12$	0.8	180000	1164.4	81.1
Lennard-Jones $k = 12$	0.9	180000	508.9	81.1
Lennard-Jones $k = 12$	1.0	180000	267.1	81.1
Lennard-Jones $k = 9$	0.9	80000	1682.6	54.1
Lennard-Jones $k = 9$	1.2	80000	248.1	54.1
Buckingham $k = 3$	0.7	80000	1002.8	54.1
Buckingham $k = 3$	0.8	80000	391.4	54.1
Buckingham $k = 2$	0.9	80000	649.3	54.1
Buckingham $k = 2$	1.1	80000	190.0	54.1
Fluid	T [K]	N	L [Å]	W [Å]
Benzene	365	2400	1908.4	50.0
Benzene	415	2400	658.9	50.0
Butane	295	4000	4364.8	50.0
Butane	325	4000	1769.6	50.0
Butane	360	4000	1174.8	50.0
Methane	120	4000	1573.7	50.0
Methane	135	4000	729.3	50.0
Methane	150	4000	355.0	50.0
Methanol	325	4000	2595.2	50.0
Methanol	375	4000	574.5	50.0
Water	500	4000	2506.84	37.5
Water	525	4000	1315.5	37.5
Water	550	4000	853.5	37.5
Water	575	4000	524.0	37.5

Table 3.11: Number of particles N, domain size L, droplet radius R and accommodation coefficient α for Lennard Jones potential with $k = 12$ for $T = 0.6$ and $T = 0.7$.

	$T = 0.6$			$T = 0.7$		
N	L	R	α	L	R	α
1800	–	–	–	47.83	6.79 ± 0.08	0.576 ± 0.025
2100	–	–	–	50.35	7.21 ± 0.06	0.595 ± 0.024
2400	–	–	–	52.65	7.57 ± 0.10	0.614 ± 0.023
2700	70.98	8.37 ± 0.17	0.715 ± 0.028	54.75	7.94 ± 0.08	0.630 ± 0.023
3000	73.52	8.65 ± 0.18	0.714 ± 0.026	56.71	8.21 ± 0.06	0.643 ± 0.023
3300	75.89	8.96 ± 0.20	0.705 ± 0.024	58.54	8.53 ± 0.09	0.654 ± 0.022
3600	78.12	9.23 ± 0.24	0.730 ± 0.020	60.26	8.79 ± 0.06	0.658 ± 0.022
3900	80.23	9.51 ± 0.08	0.784 ± 0.032	61.89	9.01 ± 0.07	0.669 ± 0.022
4200	82.24	9.74 ± 0.08	0.786 ± 0.031	63.44	9.29 ± 0.06	0.675 ± 0.021
4500	84.15	9.97 ± 0.13	0.782 ± 0.026	64.92	9.53 ± 0.06	0.685 ± 0.021
4800	85.98	10.18 ± 0.14	0.787 ± 0.024	66.33	9.74 ± 0.08	0.689 ± 0.021
5100	87.74	10.45 ± 0.09	0.800 ± 0.029	67.68	9.97 ± 0.06	0.700 ± 0.021
5400	89.43	10.62 ± 0.16	0.785 ± 0.022	68.98	10.16 ± 0.07	0.700 ± 0.020
5700	91.05	10.83 ± 0.16	0.808 ± 0.021	70.24	10.36 ± 0.07	0.702 ± 0.020
6000	92.62	11.02 ± 0.03	0.809 ± 0.031	71.45	10.56 ± 0.05	0.702 ± 0.020
9000	106.03	12.67 ± 0.04	0.834 ± 0.028	81.79	12.16 ± 0.05	0.732 ± 0.018
12000	116.70	13.99 ± 0.03	0.857 ± 0.026	90.02	13.42 ± 0.04	0.748 ± 0.017
15000	125.71	15.09 ± 0.02	0.867 ± 0.025	96.97	14.52 ± 0.04	0.765 ± 0.016
18000	133.59	16.08 ± 0.03	0.878 ± 0.023	103.05	15.48 ± 0.05	0.777 ± 0.015
21000	140.63	16.93 ± 0.02	0.881 ± 0.022	108.48	16.32 ± 0.04	0.779 ± 0.014
24000	147.03	17.70 ± 0.03	0.883 ± 0.021	113.42	17.09 ± 0.03	0.788 ± 0.014

27000	152.92	18.42 ± 0.02	0.889 ± 0.020	117.96	17.79 ± 0.04	0.791 ± 0.013
30000	158.38	19.09 ± 0.02	0.890 ± 0.020	122.18	18.45 ± 0.03	0.797 ± 0.013
33000	163.50	19.71 ± 0.04	0.893 ± 0.019	126.12	19.05 ± 0.04	0.799 ± 0.013
36000	168.31	20.30 ± 0.04	0.897 ± 0.018	129.83	19.66 ± 0.05	0.803 ± 0.012
39000	172.86	20.88 ± 0.03	0.899 ± 0.018	133.34	20.21 ± 0.06	0.806 ± 0.012
42000	177.18	21.37 ± 0.04	0.897 ± 0.018	136.68	20.69 ± 0.05	0.807 ± 0.012
45000	181.30	21.90 ± 0.03	0.903 ± 0.017	139.86	21.23 ± 0.06	0.809 ± 0.012
48000	185.25	22.35 ± 0.06	0.904 ± 0.017	142.90	21.74 ± 0.08	0.814 ± 0.011
–	–	–	–	145.82	22.19 ± 0.10	0.815 ± 0.011
54000	192.66	23.26 ± 0.06	0.906 ± 0.016	148.62	22.71 ± 0.14	0.819 ± 0.011
57000	196.17	23.68 ± 0.05	0.909 ± 0.016	151.33	23.19 ± 0.18	0.826 ± 0.011
–	–	–	–	153.94	23.51 ± 0.14	0.820 ± 0.011

Table 3.12: Number of particles N, domain size L, droplet radius R and accommodation coefficient α for Lennard Jones potential with $k = 12$ for $T = 0.8$.

N	L	R	α
		$T = 0.8$	
1500	35.09	6.13 ± 0.11	0.392 ± 0.015
1800	37.29	6.59 ± 0.11	0.419 ± 0.015
1800	41.95	5.15 ± 0.26	0.314 ± 0.014
2100	39.26	7.00 ± 0.11	0.442 ± 0.015
2100	44.16	5.66 ± 0.27	0.350 ± 0.014
2400	41.04	7.37 ± 0.12	0.456 ± 0.014
2400	46.17	6.04 ± 0.27	0.376 ± 0.014
2700	42.69	7.71 ± 0.15	0.472 ± 0.014
2700	48.02	6.44 ± 0.41	0.389 ± 0.013
3000	44.21	8.00 ± 0.15	0.485 ± 0.014
3000	49.74	6.73 ± 0.40	0.405 ± 0.013
3300	45.64	8.30 ± 0.08	0.501 ± 0.014
3300	51.34	7.10 ± 0.20	0.436 ± 0.014
3600	46.98	8.55 ± 0.11	0.503 ± 0.014
3600	52.85	7.30 ± 0.20	0.446 ± 0.014
3900	48.25	8.80 ± 0.07	0.513 ± 0.014
3900	54.28	7.57 ± 0.22	0.458 ± 0.014
4200	49.46	9.08 ± 0.12	0.524 ± 0.013
4200	55.64	7.83 ± 0.18	0.471 ± 0.014
4500	50.61	9.29 ± 0.15	0.528 ± 0.013
4500	56.94	8.05 ± 0.27	0.480 ± 0.013

4800	51.71	9.51 ± 0.14	0.537 ± 0.013
4800	58.17	8.29 ± 0.30	0.489 ± 0.013
5100	52.77	9.72 ± 0.17	0.541 ± 0.013
5100	59.36	8.43 ± 0.29	0.495 ± 0.013
5400	53.78	9.93 ± 0.14	0.547 ± 0.013
5400	60.50	8.66 ± 0.33	0.502 ± 0.012
5700	54.76	10.13 ± 0.10	0.551 ± 0.013
5700	61.60	8.82 ± 0.47	0.506 ± 0.011
6000	55.70	10.32 ± 0.07	0.547 ± 0.012
6000	62.67	9.03 ± 0.47	0.512 ± 0.010
9000	63.76	11.93 ± 0.06	0.584 ± 0.011
9000	71.73	10.55 ± 0.07	0.553 ± 0.012
12000	70.18	13.20 ± 0.06	0.599 ± 0.011
12000	78.95	11.73 ± 0.08	0.576 ± 0.014
15000	75.60	14.25 ± 0.05	0.613 ± 0.010
15000	85.05	12.76 ± 0.05	0.598 ± 0.015
18000	80.34	15.20 ± 0.06	0.623 ± 0.010
18000	90.38	13.69 ± 0.07	0.612 ± 0.016
21000	84.57	16.04 ± 0.04	0.634 ± 0.009
21000	95.15	14.42 ± 0.05	0.619 ± 0.016
24000	88.42	16.82 ± 0.05	0.640 ± 0.009
24000	99.48	15.19 ± 0.05	0.628 ± 0.017
27000	91.96	17.52 ± 0.06	0.647 ± 0.009
27000	103.46	15.86 ± 0.06	0.632 ± 0.017
30000	95.25	18.16 ± 0.05	0.652 ± 0.009

30000	107.16	16.51 ± 0.05	0.642 ± 0.018
33000	98.33	18.78 ± 0.05	0.652 ± 0.008
36000	101.22	19.37 ± 0.04	0.658 ± 0.008
39000	103.96	19.92 ± 0.04	0.664 ± 0.008
42000	106.56	20.40 ± 0.04	0.663 ± 0.008
45000	109.04	20.91 ± 0.05	0.666 ± 0.008
48000	111.41	21.37 ± 0.06	0.667 ± 0.008
51000	113.68	21.84 ± 0.05	0.669 ± 0.007
54000	115.87	22.27 ± 0.09	0.671 ± 0.007
57000	117.97	22.72 ± 0.09	0.673 ± 0.007
60000	120.01	23.17 ± 0.09	0.678 ± 0.007

Table 3.13: Number of particles N, domain size L, droplet radius R and accommodation coefficient α for Lennard Jones potential with $k = 12$ for $T = 0.9$ and $T = 1.0$.

	$T = 0.9$			$T = 1.0$		
N	L	R	α	L	R	α
1500	29.84	5.47 ± 0.23	0.209 ± 0.008	–	–	–
1800	31.71	5.94 ± 0.20	0.235 ± 0.008	–	–	–
2100	33.39	6.35 ± 0.21	0.255 ± 0.008	–	–	–
2400	34.91	6.76 ± 0.24	0.274 ± 0.008	–	–	–
2700	36.30	7.08 ± 0.25	0.286 ± 0.008	–	–	–
3000	37.60	7.38 ± 0.24	0.300 ± 0.008	33.46	5.50 ± 0.42	0.088 ± 0.003
3300	38.81	7.68 ± 0.21	0.312 ± 0.008	34.54	5.91 ± 0.40	0.105 ± 0.003
3600	39.96	7.93 ± 0.16	0.320 ± 0.008	35.55	6.26 ± 0.29	0.118 ± 0.004
3900	41.04	8.21 ± 0.18	0.331 ± 0.008	36.51	6.47 ± 0.39	0.123 ± 0.004
4200	42.06	8.43 ± 0.15	0.338 ± 0.008	37.43	6.58 ± 0.43	0.125 ± 0.004
4500	43.04	8.69 ± 0.15	0.348 ± 0.008	38.30	6.90 ± 0.36	0.137 ± 0.004
4800	43.98	8.89 ± 0.18	0.350 ± 0.008	39.13	7.07 ± 0.41	0.141 ± 0.004
5100	44.88	9.12 ± 0.16	0.359 ± 0.008	39.93	7.35 ± 0.43	0.152 ± 0.004
5400	45.74	9.27 ± 0.20	0.361 ± 0.008	40.70	7.53 ± 0.49	0.156 ± 0.004
5700	46.57	9.51 ± 0.23	0.371 ± 0.008	41.44	7.74 ± 0.45	0.163 ± 0.004
6000	47.37	9.72 ± 0.11	0.366 ± 0.008	42.15	8.08 ± 0.30	0.170 ± 0.004
9000	54.23	11.27 ± 0.09	0.398 ± 0.007	48.25	9.65 ± 0.22	0.208 ± 0.004
12000	59.69	12.51 ± 0.10	0.417 ± 0.007	53.11	10.83 ± 0.23	0.230 ± 0.004
15000	64.30	13.59 ± 0.08	0.436 ± 0.006	57.21	11.89 ± 0.18	0.247 ± 0.004
18000	68.32	14.49 ± 0.09	0.444 ± 0.006	60.79	12.76 ± 0.14	0.258 ± 0.004
21000	71.93	15.32 ± 0.07	0.452 ± 0.006	64.00	13.55 ± 0.15	0.268 ± 0.004

24000	75.20	16.03 ± 0.08	0.459 ± 0.006	66.91	14.31 ± 0.14	0.277 ± 0.003
27000	78.21	16.74 ± 0.07	0.465 ± 0.006	69.59	15.05 ± 0.14	0.286 ± 0.003
30000	81.01	17.41 ± 0.08	0.473 ± 0.005	72.08	15.57 ± 0.12	0.289 ± 0.003
33000	83.62	18.00 ± 0.07	0.476 ± 0.005	74.41	16.16 ± 0.13	0.296 ± 0.003
36000	86.08	18.60 ± 0.06	0.481 ± 0.005	76.60	16.69 ± 0.12	0.298 ± 0.003
39000	88.41	19.12 ± 0.06	0.483 ± 0.005	78.67	17.16 ± 0.14	0.302 ± 0.003
42000	90.62	19.61 ± 0.05	0.485 ± 0.005	80.64	17.67 ± 0.11	0.306 ± 0.003
45000	92.73	20.07 ± 0.06	0.488 ± 0.005	82.51	18.15 ± 0.10	0.309 ± 0.003
48000	94.75	20.56 ± 0.06	0.491 ± 0.005	84.31	18.54 ± 0.10	0.310 ± 0.003
51000	96.68	20.98 ± 0.06	0.493 ± 0.005	86.03	19.08 ± 0.09	0.317 ± 0.003
54000	98.54	21.45 ± 0.05	0.493 ± 0.005	87.68	19.46 ± 0.09	0.317 ± 0.003
57000	100.33	21.76 ± 0.07	0.492 ± 0.005	89.28	19.86 ± 0.11	0.320 ± 0.003
60000	102.06	22.22 ± 0.07	0.498 ± 0.005	90.82	20.30 ± 0.10	0.321 ± 0.003

Table 3.14: Number of particles N, domain size L, droplet radius R and accommodation coefficient α for Lennard Jones potential with $k = 9$. Value in (.) in the uncertainty.

$T = 0.9$			
N	L	R	α
4800	65.82	6.29 ± 0.26	0.458 ± 0.015
6900	74.28	7.93 ± 0.16	0.540 ± 0.014
9600	82.93	9.39 ± 0.12	0.589 ± 0.013
12600	90.80	10.56 ± 0.12	0.620 ± 0.012
16500	99.34	11.79 ± 0.10	0.644 ± 0.011
21000	107.65	12.96 ± 0.09	0.664 ± 0.011
26100	115.74	14.05 ± 0.07	0.676 ± 0.010
30000	121.24	14.97 ± 0.06	0.688 ± 0.010
39000	132.32	16.52 ± 0.05	0.702 ± 0.009
48000	141.81	17.89 ± 0.07	0.711 ± 0.008
57000	150.17	19.11 ± 0.11	0.718 ± 0.008
63000	155.26	19.84 ± 0.12	0.721 ± 0.008
75000	164.55	21.29 ± 0.17	0.729 ± 0.007
$T = 1.2$			
N	L	R	α
3900	34.15	7.15 ± 0.31	0.128 ± 0.003
5700	38.75	8.56 ± 0.25	0.167 ± 0.003
7800	43.02	9.80 ± 0.19	0.193 ± 0.003
10200	47.05	10.88 ± 0.17	0.212 ± 0.003
13500	51.66	12.20 ± 0.16	0.233 ± 0.003
17100	55.89	13.34 ± 0.17	0.247 ± 0.003
21300	60.14	14.51 ± 0.16	0.260 ± 0.003
26100	64.35	15.72 ± 0.13	0.273 ± 0.003
33000	69.58	17.09 ± 0.13	0.281 ± 0.003
39000	73.57	18.24 ± 0.15	0.290 ± 0.002
45000	77.16	19.20 ± 0.12	0.295 ± 0.002
54000	82.00	20.46 ± 0.12	0.300 ± 0.002
63000	86.32	21.59 ± 0.10	0.306 ± 0.002

Table 3.15: Number of particles N, domain size L, droplet radius R and accommodation coefficient α for Buckingham potential with $k = 3$.

$T = 0.7$			
N	L	R	α
1800	31.06	6.42 ± 0.07	0.443 ± 0.016
2700	35.55	7.44 ± 0.07	0.489 ± 0.015
4500	42.15	8.90 ± 0.06	0.541 ± 0.014
6900	48.60	10.35 ± 0.05	0.580 ± 0.013
9900	54.82	11.72 ± 0.04	0.603 ± 0.012
13500	60.79	13.05 ± 0.04	0.626 ± 0.011
18000	66.91	14.40 ± 0.04	0.642 ± 0.011
23400	73.02	15.76 ± 0.04	0.656 ± 0.010
30000	79.33	17.14 ± 0.03	0.665 ± 0.011
36000	84.30	18.23 ± 0.03	0.673 ± 0.012
54000	96.50	20.95 ± 0.02	0.689 ± 0.014
$T = 0.8$			
N	L	R	α
1500	24.32	5.69 ± 0.12	0.239 ± 0.008
2700	29.58	7.13 ± 0.10	0.302 ± 0.008
4200	34.27	8.36 ± 0.09	0.340 ± 0.008
6300	39.23	9.71 ± 0.08	0.379 ± 0.008
9000	44.18	11.01 ± 0.07	0.406 ± 0.007
16500	54.08	13.63 ± 0.06	0.443 ± 0.006
21300	58.88	14.90 ± 0.05	0.457 ± 0.006
27300	63.96	16.22 ± 0.05	0.466 ± 0.006
33000	68.13	17.33 ± 0.05	0.474 ± 0.005
42000	73.84	18.85 ± 0.05	0.484 ± 0.005
51000	78.77	20.16 ± 0.05	0.495 ± 0.006

Table 3.16: Number of particles N, domain size L, droplet radius R and accommodation coefficient α for Buckingham potential with $k = 2$.

		$T = 0.9$	
N	L	R	α
3000	40.91	6.02 ± 0.13	0.398 ± 0.012
4800	47.85	7.37 ± 0.09	0.467 ± 0.011
7200	54.78	8.65 ± 0.07	0.513 ± 0.010
10200	61.52	9.85 ± 0.08	0.545 ± 0.010
14100	68.53	11.11 ± 0.08	0.575 ± 0.009
18600	75.16	12.35 ± 0.07	0.594 ± 0.008
24000	81.83	13.56 ± 0.05	0.614 ± 0.008
30000	88.14	14.66 ± 0.04	0.624 ± 0.007
39000	96.20	16.08 ± 0.05	0.639 ± 0.007
48000	103.09	17.36 ± 0.04	0.649 ± 0.009
		$T = 1.1$	
N	L	R	α
4200	33.11	5.78 ± 0.31	0.133 ± 0.004
6000	37.29	6.96 ± 0.23	0.180 ± 0.004
8700	42.20	8.26 ± 0.18	0.220 ± 0.004
12000	46.98	9.53 ± 0.17	0.253 ± 0.004
15900	51.60	10.57 ± 0.17	0.271 ± 0.004
20700	56.34	11.82 ± 0.13	0.292 ± 0.004
26400	61.10	8.26 ± 0.18	0.220 ± 0.004
33000	65.82	14.17 ± 0.10	0.322 ± 0.003
39000	69.58	15.13 ± 0.09	0.332 ± 0.003
48000	74.57	16.27 ± 0.09	0.339 ± 0.003

Table 3.17: Number of molecules N, domain size L, droplet radius R and accommodation coefficient α for benzene.

		$T = 365$ K	
N	L [Å]	R [Å]	α
686	140.23	22.26 ± 0.94	0.277 ± 0.054
1024	160.26	26.55 ± 0.57	0.354 ± 0.053
1458	180.30	29.97 ± 0.54	0.401 ± 0.054
2000	200.33	34.35 ± 0.51	0.447 ± 0.052
2662	220.36	38.01 ± 0.73	0.475 ± 0.051
3456	240.40	42.09 ± 0.51	0.523 ± 0.050
4394	260.43	45.74 ± 0.66	0.539 ± 0.048
5488	280.46	49.73 ± 0.56	0.556 ± 0.048
6750	300.50	53.71 ± 0.51	0.579 ± 0.053
8192	320.53	57.01 ± 0.62	0.589 ± 0.042
9826	340.56	60.90 ± 0.50	0.608 ± 0.041
11664	360.60	64.78 ± 0.66	0.621 ± 0.043
13718	380.63	68.91 ± 0.61	0.638 ± 0.044
16000	400.66	72.45 ± 0.50	0.634 ± 0.046
		$T = 415$ K	
N	L [Å]	R [Å]	α
2000	155.60	28.37 ± 1.19	0.136 ± 0.017
2662	171.16	31.01 ± 1.55	0.140 ± 0.014
3456	186.72	35.96 ± 1.05	0.192 ± 0.021
4394	202.28	39.48 ± 1.14	0.219 ± 0.023
5488	217.84	43.18 ± 0.98	0.241 ± 0.019
6750	233.40	47.77 ± 1.22	0.276 ± 0.025
8192	248.96	50.34 ± 1.07	0.281 ± 0.021
9826	264.53	53.44 ± 1.17	0.297 ± 0.018
11664	280.09	57.69 ± 1.10	0.317 ± 0.025
13718	295.65	62.11 ± 1.46	0.336 ± 0.030
16000	311.21	65.71 ± 0.97	0.353 ± 0.031

Table 3.18: Number of molecules N, domain size L, droplet radius R and accommodation coefficient α for butane at $T = 295$ K and $T = 325$ K.

$T = 295$ K			
N	L [Å]	R [Å]	α
1024	151.97	20.74 ± 1.19	0.065 ± 0.010
1458	170.97	25.66 ± 0.99	0.111 ± 0.012
2000	189.96	30.32 ± 0.60	0.153 ± 0.014
2662	208.96	34.02 ± 0.80	0.174 ± 0.013
3456	227.96	38.35 ± 0.42	0.206 ± 0.014
4394	246.95	41.85 ± 0.60	0.222 ± 0.014
5488	265.95	45.65 ± 0.36	0.241 ± 0.013
6750	284.94	49.24 ± 0.56	0.252 ± 0.013
8192	303.94	52.72 ± 0.40	0.264 ± 0.013
9826	322.94	55.73 ± 0.31	0.267 ± 0.012
11664	341.93	59.95 ± 0.40	0.286 ± 0.012
13718	360.93	63.92 ± 0.31	0.296 ± 0.012
16000	379.93	67.27 ± 0.30	0.304 ± 0.011
$T = 325$ K			
N	L [Å]	R [Å]	α
1458	136.17	24.85 ± 1.84	0.055 ± 0.007
2000	151.30	30.46 ± 1.00	0.090 ± 0.007
2662	166.43	34.73 ± 0.91	0.110 ± 0.008
3456	181.56	38.60 ± 0.79	0.136 ± 0.008
4394	196.69	41.90 ± 0.76	0.145 ± 0.008
5488	211.82	46.08 ± 0.57	0.173 ± 0.009
6750	226.95	49.48 ± 0.59	0.184 ± 0.008
8192	242.08	53.57 ± 0.61	0.202 ± 0.009
9826	257.21	57.28 ± 0.57	0.211 ± 0.008
11664	272.34	60.93 ± 0.50	0.228 ± 0.008
13718	287.47	64.80 ± 0.68	0.236 ± 0.008
16000	302.60	68.23 ± 0.57	0.243 ± 0.008

Table 3.19: Number of molecules N, domain size L, droplet radius R and accommodation coefficient α for butane at $T = 360$ K.

N	L [Å]	R [Å]	α
4394	160.05	37.15 ± 2.56	0.046 ± 0.003
5488	172.36	42.07 ± 1.97	0.043 ± 0.003
6750	184.68	45.85 ± 1.72	0.057 ± 0.003
8192	196.99	49.41 ± 1.58	0.071 ± 0.003
9826	209.30	54.22 ± 1.43	0.076 ± 0.003
11664	221.61	58.74 ± 1.12	0.086 ± 0.003
13718	233.92	61.39 ± 1.20	0.088 ± 0.003
16000	246.23	65.67 ± 1.10	0.098 ± 0.003

Table 3.20: Number of molecules N, domain size L, droplet radius R and accommodation coefficient α for methane at $T = 120$ K and $T = 135$ K.

$T = 120$ K			
N	L [Å]	R [Å]	α
1024	94.68	20.76 ± 0.30	0.180 ± 0.015
1458	106.52	24.10 ± 0.29	0.230 ± 0.016
2000	118.36	26.96 ± 0.34	0.270 ± 0.017
2662	130.19	29.95 ± 0.20	0.300 ± 0.017
3456	142.03	33.03 ± 0.30	0.330 ± 0.016
4394	153.86	35.66 ± 0.21	0.352 ± 0.016
5488	165.70	38.94 ± 0.20	0.378 ± 0.016
6750	177.53	41.61 ± 0.21	0.397 ± 0.015
8192	189.37	44.69 ± 0.16	0.415 ± 0.015
9826	201.20	47.43 ± 0.25	0.424 ± 0.014
11664	213.04	50.38 ± 0.18	0.443 ± 0.015
13718	224.87	53.39 ± 0.19	0.453 ± 0.016
16000	236.71	56.18 ± 0.15	0.468 ± 0.021
$T = 135$ K			
N	L [Å]	R [Å]	α
1024	84.54	17.35 ± 0.93	0.050 ± 0.007
1458	95.11	20.18 ± 0.81	0.073 ± 0.006
2000	105.68	23.53 ± 0.62	0.106 ± 0.007
2662	116.24	26.59 ± 0.54	0.136 ± 0.008
3456	126.81	29.53 ± 0.39	0.157 ± 0.008
4394	137.38	31.75 ± 0.55	0.167 ± 0.008
5488	147.95	35.01 ± 0.37	0.194 ± 0.011
6750	158.52	37.76 ± 0.38	0.210 ± 0.010
8192	169.08	40.62 ± 0.38	0.228 ± 0.009
9826	179.65	43.04 ± 0.45	0.236 ± 0.009
11664	190.22	46.25 ± 0.40	0.258 ± 0.010
13718	200.79	49.00 ± 0.26	0.267 ± 0.011
16000	211.35	52.13 ± 0.31	0.283 ± 0.013

Table 3.21: Number of molecules N, domain size L, droplet radius R and accommodation coefficient α for methane at $T = 150$ K.

N	L [Å]	R [Å]	α
4394	112.93	29.88 ± 1.49	0.045 ± 0.002
5488	121.61	32.04 ± 1.60	0.048 ± 0.003
6750	130.30	36.58 ± 1.05	0.064 ± 0.003
8192	138.99	39.64 ± 0.99	0.076 ± 0.003
9826	147.67	42.09 ± 0.74	0.080 ± 0.004
11664	156.36	44.48 ± 0.92	0.083 ± 0.004
13718	165.05	47.78 ± 0.81	0.093 ± 0.005
16000	173.73	50.31 ± 0.87	0.096 ± 0.004

Table 3.22: Number of molecules N, domain size L, droplet radius R and accommodation coefficient α for methanol.

$T = 375$ K			
N	L [Å]	R [Å]	α
686	114.46	19.70 ± 0.41	0.376 ± 0.058
1024	130.81	22.56 ± 0.51	0.427 ± 0.054
1458	147.16	25.38 ± 0.37	0.436 ± 0.049
2000	163.51	28.52 ± 0.45	0.463 ± 0.045
2662	179.86	31.31 ± 0.38	0.474 ± 0.043
3456	196.21	34.82 ± 0.32	0.505 ± 0.041
4394	212.56	37.81 ± 0.48	0.514 ± 0.038
5488	228.92	40.81 ± 0.22	0.525 ± 0.037
6750	245.27	43.86 ± 0.44	0.530 ± 0.034
8192	261.62	46.81 ± 0.45	0.537 ± 0.033
9826	277.97	50.06 ± 0.35	0.543 ± 0.031
11664	294.32	53.01 ± 0.40	0.549 ± 0.030
13718	310.67	55.97 ± 0.36	0.560 ± 0.029
16000	327.02	59.29 ± 0.34	0.564 ± 0.028
$T = 425$ K			
N	L [Å]	R [Å]	α
2662	151.61	21.32 ± 1.52	0.208 ± 0.021
3456	165.40	23.91 ± 1.43	0.231 ± 0.021
4394	179.18	25.14 ± 1.26	0.254 ± 0.019
5488	192.96	27.90 ± 1.01	0.268 ± 0.019
6750	206.75	30.91 ± 1.34	0.295 ± 0.018
8192	220.53	32.51 ± 2.07	0.293 ± 0.017
9826	234.31	35.26 ± 1.82	0.307 ± 0.016
11664	248.09	37.77 ± 2.30	0.316 ± 0.016
13718	261.88	40.10 ± 1.88	0.324 ± 0.015
16000	275.66	43.11 ± 2.73	0.335 ± 0.015

Table 3.23: Number of molecules N, domain size L, droplet radius R and accommodation coefficient α for water at $T = 500$ K and $T = 525$ K.

N	L [Å]	R [Å]	α
$T = 500$ K			
1500	112.52	19.84 ± 0.42	0.162 ± 0.010
1997	123.81	22.00 ± 0.42	0.178 ± 0.010
2592	135.03	24.15 ± 0.40	0.183 ± 0.009
3296	146.30	26.27 ± 0.39	0.201 ± 0.009
4116	157.53	28.53 ± 0.35	0.231 ± 0.010
5063	168.80	30.70 ± 0.32	0.238 ± 0.009
6144	180.04	32.83 ± 0.30	0.236 ± 0.009
7370	191.30	34.99 ± 0.30	0.268 ± 0.009
8748	202.54	37.16 ± 0.30	0.281 ± 0.009
10289	213.81	39.31 ± 0.30	0.280 ± 0.009
12000	225.05	41.43 ± 0.27	0.286 ± 0.008
$T = 525$ K			
1500	94.20	20.07 ± 0.56	0.131 ± 0.007
1997	103.64	22.38 ± 0.48	0.145 ± 0.007
2592	113.04	24.54 ± 0.47	0.165 ± 0.007
3296	122.47	26.84 ± 0.44	0.179 ± 0.007
4116	131.88	29.01 ± 0.42	0.185 ± 0.007
5063	141.31	31.32 ± 0.39	0.203 ± 0.008
6144	150.72	33.46 ± 0.38	0.214 ± 0.009
7370	160.15	35.65 ± 0.36	0.218 ± 0.007
8748	169.55	37.84 ± 0.35	0.213 ± 0.006
10289	178.98	40.07 ± 0.32	0.234 ± 0.007
12000	188.39	0.00 ± 0.00	0.000 ± 0.000

Table 3.24: Number of molecules N, domain size L, droplet radius R and accommodation coefficient α for water at $T = 550$ K and $T = 575$ K.

$T = 550$ K			
N	L [Å]	R [Å]	α
1500	90.45	17.95 ± 0.99	0.064 ± 0.004
1997	99.51	20.23 ± 0.77	0.071 ± 0.004
2592	108.53	22.36 ± 0.75	0.086 ± 0.006
3296	117.60	24.54 ± 0.67	0.099 ± 0.004
4116	126.62	26.84 ± 0.64	0.099 ± 0.004
5063	135.68	28.87 ± 0.63	0.121 ± 0.004
6144	144.71	31.01 ± 0.52	0.129 ± 0.004
7370	153.77	33.26 ± 0.55	0.125 ± 0.004
8748	162.80	35.45 ± 0.49	0.144 ± 0.005
10289	171.85	37.60 ± 0.45	0.141 ± 0.004
12000	180.89	39.63 ± 0.47	0.153 ± 0.004
$T = 575$ K			
N	L [Å]	R [Å]	α
2592	101.11	16.94 ± 1.99	0.023 ± 0.002
3296	109.55	20.11 ± 1.61	0.040 ± 0.002
4116	117.97	22.12 ± 1.43	0.053 ± 0.003
5063	126.40	24.83 ± 1.12	0.047 ± 0.002
6144	134.82	27.32 ± 0.99	0.057 ± 0.002
7370	143.25	29.06 ± 0.95	0.064 ± 0.003
8748	151.67	31.56 ± 0.94	0.072 ± 0.003
10289	160.10	33.15 ± 0.85	0.067 ± 0.002
12000	168.52	35.36 ± 0.88	0.079 ± 0.002

4 Molecular Calculations of Fluid-Fluid Interfacial Mobility

4.1 Introduction

Fluid-fluid interfaces are abundant in nature and in industrial processes involving drops and sprays [172], fluid injections [173], and emulsions [174, 175]. Interfacial motion is a dominant feature in many systems with applications including targeted drug delivery [174], self-cleaning surfaces [176], electrowetting-based reflective displays [177], and fiber optics [178]. Interfacial motion is important in these applications because it controls where and how drugs are released [174], how quickly a surface can be cleaned [176, 179], how light is refracted [178], how rapidly a display can be changed [177] and how transmission through a fiber optic cable can be tuned [178].

Diffuse interface models are widely used in the literature [172, 173, 179–185] and are often more favorable than their sharp interface counterparts to model the fluid-fluid interfaces mentioned above. Diffuse interface models treat the interface as a finite region between two fluids with physical properties that smoothly transition between the bulk properties of the two fluids due to diffusive mixing of the species. Sharp interface models treat the bulk fluids separately, connecting the fluids through an infinitely thin interfacial region leading to discontinuous physical properties and jump boundary conditions. Diffuse interface models avoid drawbacks such as mathematical singularities due to contact line motion, [180,182–185] are able to handle mass transfer across the interface [186], interface breakup [173], and ion or particle trapping at the interface [187], and do not require computationally expensive interface tracking [180, 182]. Furthermore, diffuse interface models are more appropriate for situations

in which the characteristic length scale of a fluid approaches the fluid-fluid interfacial thickness. Such situations include nano-liquid printing [173, 188] where droplets can have radii as small as 300 nm [188] and coalescence induced jumping of nano-droplets [189].

An important parameter in diffuse interface models is the interfacial mobility. This quantity, which is a measure of how the fluid-fluid interface fluctuates with time, dictates topological changes and energetic dissipation at the interface [181]. Like surface tension, it also connects the molecular scale interface motion to the broader hydrodynamic motion [183]. However, it is not currently possible to measure mobility experimentally, making the proper value for the mobility difficult to establish [172]. As a result, values for mobility are frequently estimated [173] or obtained from multiparameter fitting to experimental data [183–185]. This often leads to non-unique solutions [183, 184] in numerical models, which limits the predictive nature of these models.

Molecular dynamics (MD) simulations provide a different, direct approach to obtain physically meaningful fluid-fluid interfacial mobility values. MD has been widely used to study liquid-liquid [186, 190–192] and liquid-vapor interfaces [193–198] to calculate interfacial properties such as surface tension and interface thickness. It has also been used to calculate the mobility of particles [85, 199] and ions [187, 200] in bulk fluids and near or trapped within fluid-fluid interfaces [85, 187, 199, 200]. However, while interfacial mobility has been calculated for solid-solid interfaces such as grain boundaries [201–203], it has not yet been calculated for fluid-fluid interfaces.

The interfacial mobility M is related to the mean square displacement (MSD)

of the interface given by [85, 201]

$$\frac{\partial \langle \delta x_{int}(t)^2 \rangle}{\partial t} = \frac{2Mk_BT}{A} \qquad (4.1)$$

where t, k_B, T, and A denote time, Boltzmann constant, temperature, and interface area, respectively. $\delta x_{int} = x_{int}(t) - x_{int}(0)$ represents the difference between instantaneous and initial interface positions and $\langle \cdot \rangle$ denotes an ensemble average. This expression is valid in the long time limit of t. [85] An alternative method for obtaining the mobility is to integrate the interfacial velocity time-autocorrelation function (VACF) [85],

$$M = \frac{1}{k_BT/A} \int_0^\infty \langle v_{int}(t)v_{int}(0) \rangle dt \qquad (4.2)$$

where v_{int} is the interfacial velocity.

In this chapter the interfacial mobilities of three fluid-fluid interfaces, two liquid-liquid and one liquid-vapor, are calculated with MD. The simulation details and implementation are discussed in Sec. 4.2. The molecular definitions of x_{int} and v_{int} are discussed in Sec. 4.3.1, while confirmation of a random interface walk is discussed in Sec. 4.3.2. The mobility calculations are presented in Sec. 4.3.3, and finally, a summary of the work as well as further applications and future directions are presented in Sec. 4.4. Note that this chapter is based upon published work in *Journal of Chemical Physics* volume 147 number 24 page 244703 (2017) [100].

4.2 Simulation Details and Implementation

4.2.1 Domain Configuration

Three fluid-fluid interfaces were modeled in this work. The first was an interface between two liquids that repel each other but whose properties are identical (denoted "LL$_1$"), the second was an interface between two different liquids ("LL$_2$"), and the third was a liquid-vapor interface ("LV"). Interfaces between two fluids, denoted α and β, were modeled as shown in Fig. 4.1. The entire domain was set to be of width W and square cross sectional area A. Particles of α with mass m_α and particles of β with mass m_β were initially placed in a simple cubic lattice structure throughout the domain. For the LL$_1$ system, $N_\alpha = 7200$ α particles were placed between 0 and $W/2$, and $N_\beta = 7200$ β particles were placed between $W/2$ and W. For the LL$_2$ system, 5808 α particles were placed between 0 and $W/2$, and 7200 β particles were placed between $W/2$ and W. For the LV system, 135 α particles were placed between 0 and $0.95W$ and 7200 particles were placed between $0.95W$ and W. The uneven distribution for this system was chosen to ensure a sufficient number of vapor particles in the domain.

Grand canonical Monte Carlo control volumes Ω_α and Ω_β, of lengths d_α and d_β, were established at the left and right boundaries of the domain. These control volumes were used to set temperature and chemical potential in the simulations, as discussed later. d_α for the LV system is significantly larger than its LL$_1$ and LL$_2$ counterparts to ensure that there are enough particles within Ω_α to define a proper temperature. The domain was divided into static bins of width Δx_{bin} and volume $V_{bin} = A\Delta x_{bin}$ in order to perform local calculations at different x positions. Reflective boundary conditions (RBC) were applied in the horizontal direction, x, while, periodic boundary
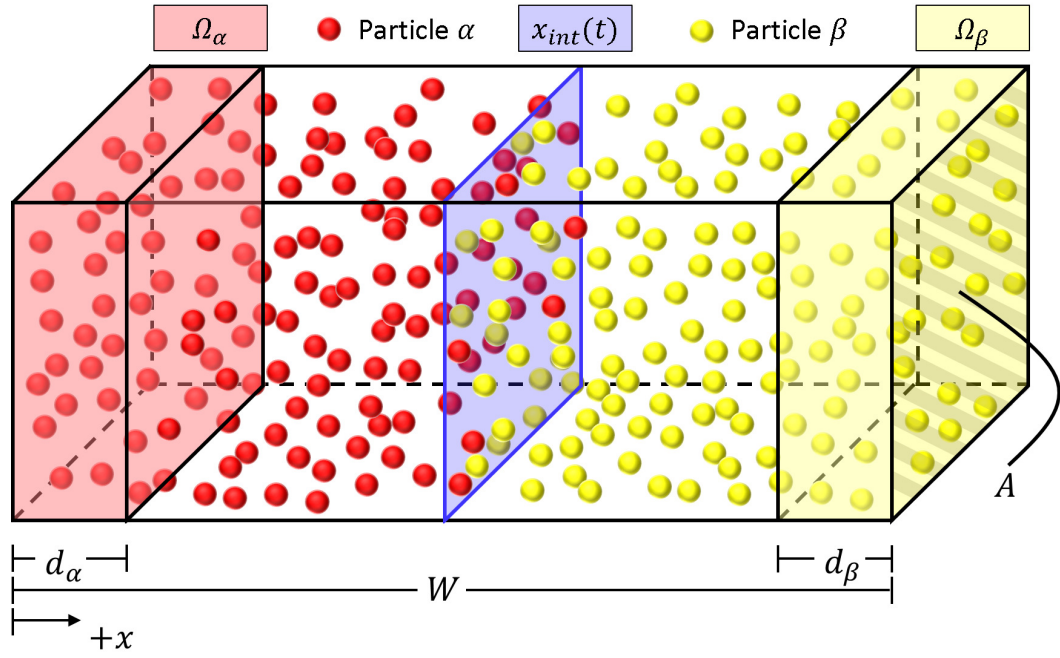
Fig. 4.1: System schematic. Shaded red and yellow regions at the boundaries indicate grand canonical Monte Carlo control volumes while the blue plane indicates the time-dependent interface position. Reflective boundary conditions are applied in the $x-$direction, while periodic boundary conditions are applied in the other directions.

Table 4.1: Input properties and geometry for the LL_1, LL_2, and LV simulations.

	m_α	m_β	$\epsilon_{\alpha\alpha}$	$\epsilon_{\beta\beta}$	$\epsilon_{\alpha\beta}$	W	d_α	d_β	μ_α	μ_β
LL_1	1	1	1	1	0.375	107.28	5.36	5.36	-8.14	-8.14
LL_2	0.8	1	0.8	1	0.375	107.28	5.36	5.36	-6.88	-8.14
LV	1	1	1	1	1	1126.4	107.28	5.36	-9.74	-8.40

Table 4.2: Common parameters used for the simulations.

T	A	r_c	Δt	τ_T	n_{eq}	n_{run}	k_{id}	k_t	Δx_{bin}
0.7	165.72	3	0.005	1	1×10^5	2×10^6	50	100	1.354

conditions (PBC) were applied in the remaining directions.

4.2.2 Numerical Integration

Simulations were run for the different interfaces using the molecular simulation package LAMMPS [204, 205] with the dimensionless truncated and shifted Lennard-Jones potential [85],

$$\phi(r) = \begin{cases} 4\epsilon_{ij}\left(\frac{1}{r^{12}} - \frac{1}{r^6} - \frac{1}{r_c^{12}} + \frac{1}{r_c^6}\right) & \text{if } r \leq r_c \\ 0 & \text{else} \end{cases}. \tag{4.3}$$

Here r, ϵ_{ij}, and r_c are the distance between particles, potential well depth and cutoff radius. The indices of ϵ refer to the two particle types α and β with $i = j$ being the self interaction and $i \neq j$ being the cross interaction. The velocity Verlet algorithm was used to integrate the equations of motion with a time step of Δt. In order to minimize density fluctuations near the RBC, a force was added to particles near the RBC to mimic the force due to the "missing" particles [206]. The value of this force is dependent on the distance from the RBC as well as the number density of the fluid. This missing force was calculated in separate simulations with PBC applied

in all directions for all fluids used. The calculated profiles for this force were found to be similar in magnitude to those found in previous works for fluids at similar temperatures and densities [206–208].

The numerical values for all parameters used in the simulations (unless otherwise noted) are found in Tables 4.1 and 4.2. All parameters and results in this work are given in dimensionless form and can be converted to real units for argon using length, energy, and mass scales of 0.3405 nm, 0.01032 eV, and 39.948 amu respectively [85]. Simulations were run on local machines as well as computing resources from the Extreme Science and Engineering Discovery Environment [209].

For each simulation, the particles were initialized to a temperature T by selecting their velocities from the corresponding Maxwell-Boltzmann distribution. To melt the lattice, the system was run for n_{eq} steps with a global Berendsen thermostat [90] with a damping constant τ_T. Then the velocity of the domain was removed to ensure that there was no bulk fluid motion in the system. Next, dual control volume grand canonical molecular dynamics (DCV-GCMD), a hybrid molecular dynamics and Monte Carlo approach [93], was performed for n_{run} time steps to maintain the control volumes Ω_α and Ω_β at chemical potentials μ_α and μ_β. Details about the values chosen for μ_α and μ_β, Table 4.1, can be found in the appendix at the end of the chapter. The temperatures of both control volumes were maintained at T using local Berendsen thermostats. To maintain μ_α and μ_β in the control volumes, grand canonical Monte Carlo was performed between every MD time step with k_t particle translation attempts and k_{id} particle insertion or deletion attempts with the probability of a particle insertion or deletion attempt being equal. The values chosen for k_t and k_{id} are similar to those in the literature [93, 94]. This process was then repeated for N_s different initial particle velocity distributions to perform the ensemble

averaging needed for Eqs. 4.1 and 4.2. The number of initializations for each type of interface can be found in Table 4.3.

4.3 Results and Discussion

4.3.1 Molecular Definitions of Interface Position and Velocity

In order to use the MSD and VACF to compute interfacial mobility, the interface position, x_{int}, and the interfacial velocity, v_{int}, are needed. x_{int} is determined as the location where the local mass density is equal to the target density. For systems such as LL_1 and LL_2 that have two species, the target density is defined as the density where $\rho_\alpha = m_\alpha N_\alpha/V_{bin}$ is equal to $\rho_\beta = m_\beta N_\beta/V_{bin}$. For systems with a single species but two phases (LV), the target density is defined as the location where the mass density, $\rho = mN/V_{bin}$, is the average of the bulk liquid and bulk vapor calculated far from the interface, $\rho(x_{int}) = (\rho_L + \rho_V)/2$. Figure 4.2 shows instantaneous snapshots of the density profiles for the three systems, and Table 4.3 gives the corresponding bulk densities of fluid α (ρ_α^B), fluid β (ρ_β^B), vapor (ρ_V), and liquid (ρ_L). To obtain x_{int}, the density profiles ρ_α, ρ_β, and ρ are linearly interpolated between the two neighboring bins over which the relative density $\rho_\alpha - \rho_\beta$ (for LL_1 and LL_2 systems) or $(\rho_L + \rho_V)/2 - \rho$ (for the LV system) changes sign. These two bins are shaded in Fig. 4.2. To determine v_{int}, it is reasonable to use the average molecular velocity of particles in a region containing the interface. Here, this region is defined as the same two spatial bins used to determine x_{int}. Other potential ways to define x_{int} and v_{int}, discussed in detail in the appendix at the end of the chapter, yield similar results for the diffusion coefficient, within 1.5%, which is less than the estimated error of roughly 5%.
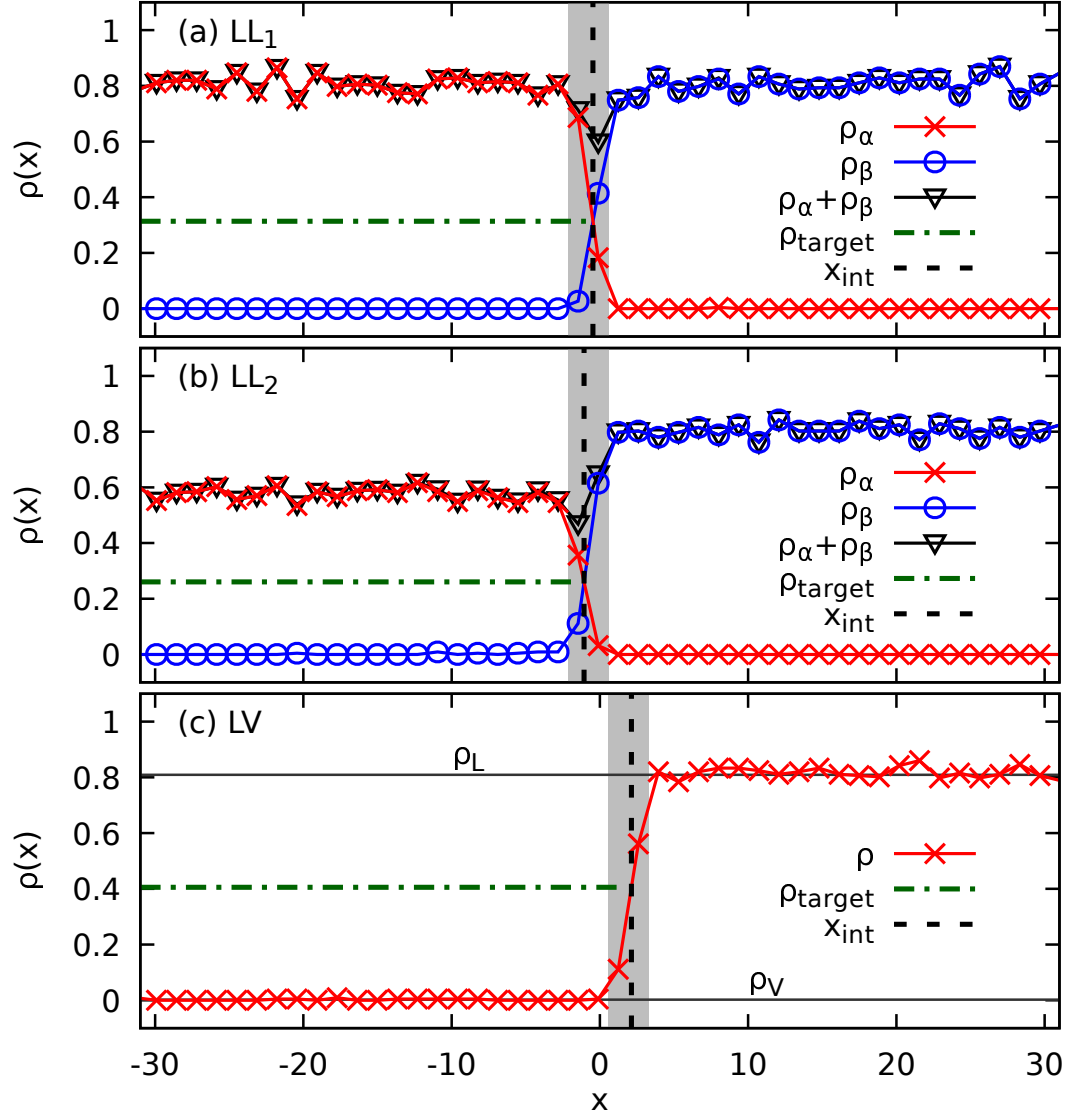
Fig. 4.2: Instantaneous local density profiles versus horizontal position for the (a) LL_1, (b) LL_2, and (c) LV interfaces. The intersection of the target density ($-\cdot-\cdot-$) and the local density profiles determines the interface positions, x_{int} ($--$). Shaded areas indicate the regions used to calculate v_{int}.

Table 4.3: Number of initializations, calculated bulk densities, and interfacial thicknesses for the three types of interfaces. The (·) represents the uncertainty in the preceding digit.

	N_s	ρ_α^B	ρ_β^B	L_{int}
LL$_1$	50	0.8072(5)	0.8074(5)	2.55(5)
LL$_2$	12	0.5719(6)	0.8072(4)	2.98(3)

	N_s	ρ_V	ρ_L	L_{int}
LV	16	0.00227(7)	0.8103(5)	2.07(1)

4.3.2 Ensuring Proper Interface Motion

In order to use Eqs. 4.1 and 4.2 to calculate mobility, the interface must be taking a random walk [85]. To ensure that the walks are indeed random, an interface displacement histogram, $\delta x_{int}(t)$, was generated from time-dependent interface positions using data from all initializations. These histograms were then fitted to a normal distribution of the form $C \exp(-(\delta x_{int})^2/2\sigma^2)$ where C and σ indicate the distribution height and width. In order to use this method to calculate mobilities, $\langle \delta x_{int}(t) \rangle$ should be approximately zero, which was found to be true as $\langle \delta x_{int}(t) \rangle$ was less than 0.4% of the interfacial thickness, L_{int}, for all three interface systems for all calculated histograms. Table 4.3 lists L_{int} for the three interfaces; details of the L_{int} calculations may be found in the appendix at the end of the chapter. Figures 4.3(a)-(c) show these distributions at several times for all three interfaces. Note that the data in Fig. 4.3 are normalized by the total number of samples in the histogram and the interfacial thickness. The results indicate that this is a truly random walk because the sum of small random numbers is expected to be normally distributed about zero due to the central limit theorem [169] which can be seen by the excellent fits of the normal distribution.

The motivation for running DCV-GCMD as opposed to normal MD in this paper
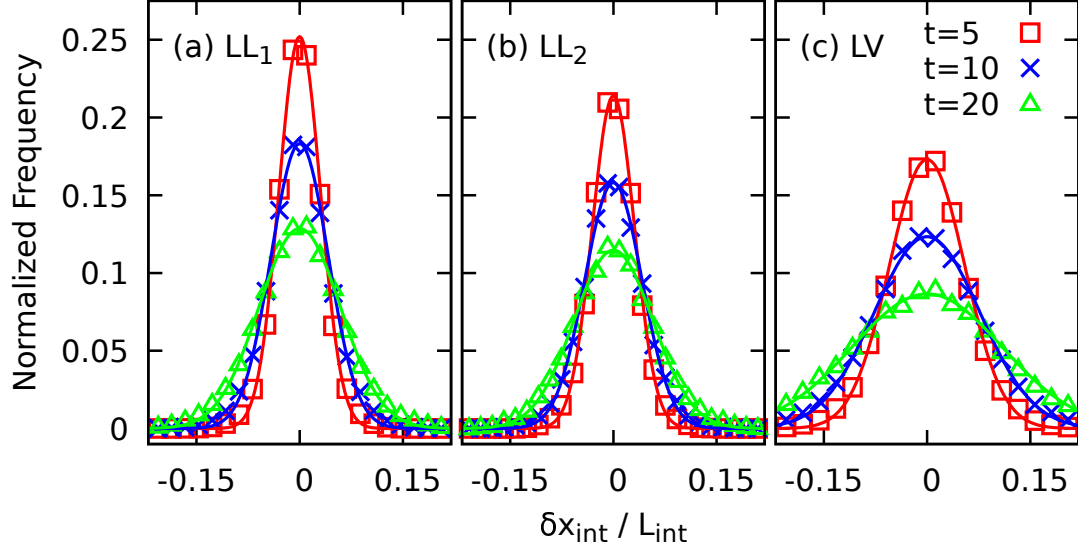
Fig. 4.3: Normalized frequency distribution for the normalized change in interface position at various times for (a) LL_1, (b) LL_2, and (c) LV. Lines represent fits of the form $C \exp(-(\delta x_{int})^2/2\sigma^2)$ where C and σ represent the distribution height and width.

was that MD simulations showed unexpected artifacts. These artifacts took the form of regular oscillations from periodic compression and expansion of the confined fluid as it moved back and forth between the domain boundaries. Compression of liquid is difficult due to its high density, which led to a suppression of the interface trajectory. DCV-GCMD allows for the interface to move without fluid compression. Detailed discussion of compression artifacts from MD and domain size effects in DCV-GCMD can be found in the appendix at the end of the chapter.

4.3.3 Mobility Calculations and Discussion

After confirming that the interface is taking a true random walk, the mobility was calculated for the LL_1, LL_2, and LV systems using three different methods. The first method was to utilize the variance, σ^2, of the distributions fit in Fig. 4.3. Figure 4.4(a) shows that the variances for these distributions linearly increase ($R^2 > 0.99$)
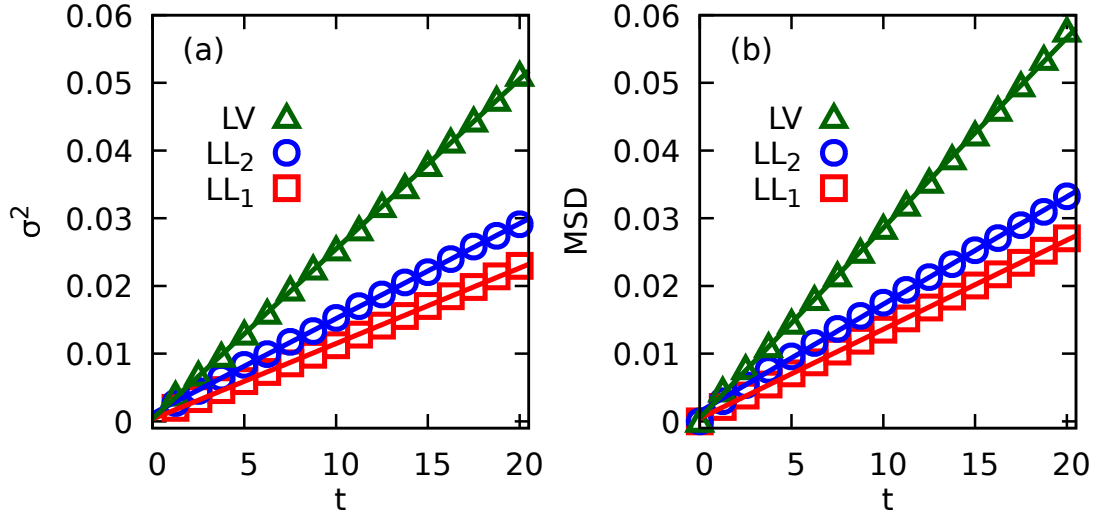
Fig. 4.4: (a) Distribution variance, σ^2, and (b) MSD versus time for the LL_1, LL_2, and LV interfaces. Error bars, not shown, are smaller than the size of the markers. Lines are linear fits of the data with $R^2 > 0.99$ for each fit.

as a function of time. Since the average interface position is zero, the variance is equivalent to the MSD and its time derivative can be used (Eq. 4.1) to calculate mobility.

The MSD was also calculated with the averages, $\langle\cdot\rangle$, in Eqs. 4.1 and 4.2, computed using data from all initializations for a time length of 100 units with new time origins taken every 5 units. This corresponds to averaging over 95, 23, or 31 thousand ensembles for the LL_1, LL_2, and LV systems respectively. Calculations with alternative time origins, from 1 time unit to 50 time units (changing the quantity in the ensemble averages from roughly 10%–500% of the previous values), were also performed; these gave similar results. Figure 4.4(b) shows that the MSD for all three interfaces increases linearly. Finally, the mobility was calculated using the VACF. Figure 4.5 shows the VACF and the time integral of the VACF for the LL_1 interface. The VACF was integrated numerically using Simpson's rule. It has a rapid decay and begins to fluctuate around zero after roughly 3 time units (inset of Fig. 4.5).
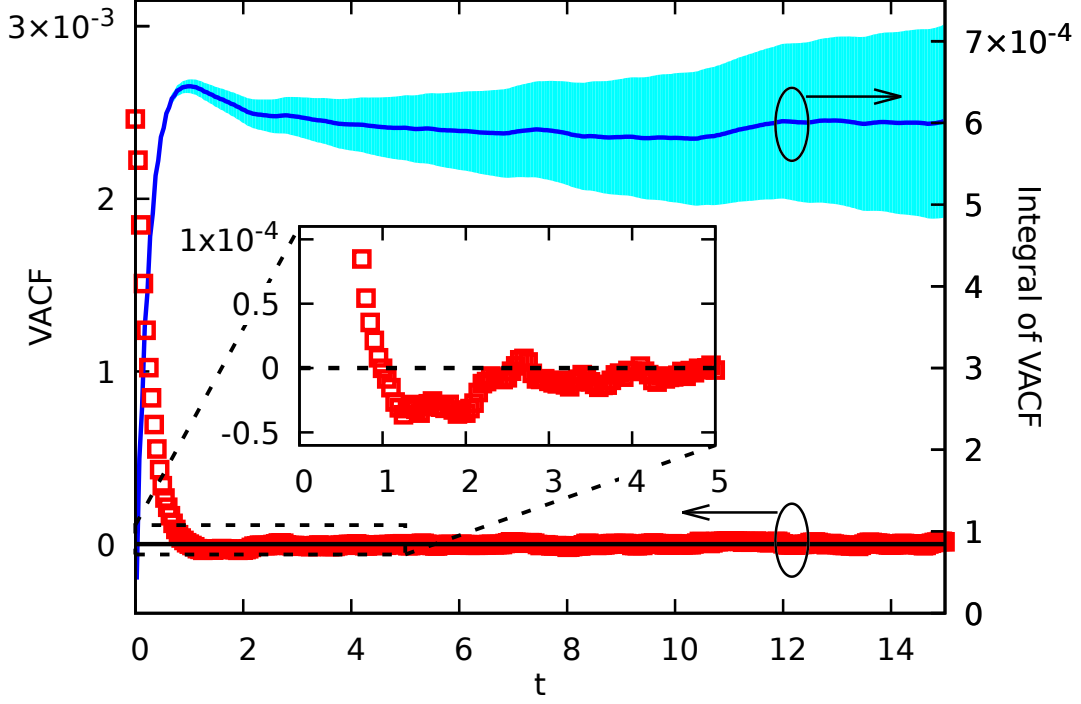
Fig. 4.5: VACF (left axis, red square) and the integral of the VACF (right axis, blue line) versus time from the LL_1 interface. Error bars for the VACF are similar in size to the markers while the error for the integral of the VACF is shown with the shaded region. Inset shows a finer resolution of the VACF.

Since the VACF approaches zero after a short period, its integral is roughly constant after 3 time units. Although the estimated error for the VACF is small, that error is compounded in the integral which is the reason for the increasing error with time. Similar curves (not shown) were obtained for the LL_2 and LV systems.

The interfacial mobilities were calculated using the above three methods in conjunction with Eqs. 4.1 and 4.2. For the MSD method, the right hand side of Eq. 4.1 was approximated as $\partial \langle \delta x_{int}^2 \rangle / \partial t \approx \Delta \langle \delta x_{int}^2 \rangle / \Delta t$ with Δt starting at 1 time unit and ending at 10 time units. The motivation for starting from 1 is to ignore any early time effects, which were found to decay after roughly 0.5 time units. For the VACF, the integral was stopped at 10 time units which allowed for the VACF to stabilize
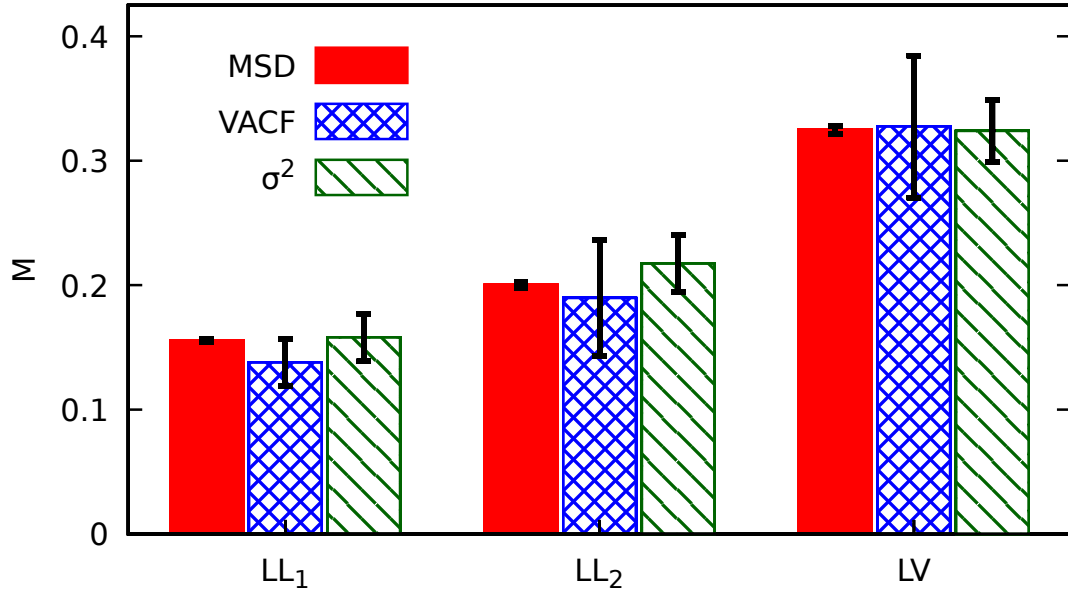
Fig. 4.6: Mobility for the LL_1, LL_2, and LV interfaces calculated from the MSD, VACF, and variance of the fitted distributions.

while not allowing the error of the integral to becomes excessively large. Figure 4.6 shows excellent agreement between the mobilities calculated with all three methods, which confirms that the interfacial mobility is indeed being captured correctly in the simulations. Furthermore, the significantly larger mobility for the LV interface is expected as moving the low density gas is relatively easier than moving a higher density liquid for the LL_1 and LL_2 interfaces.

Similarly to the diffusion coefficient and thermal conductivity, the mobility in diffuse interface models, γ, stems from a linear force-flux relation [181]. It is an inherently non-equilibrium parameter that affects how quickly an unstable interface, for example a sharp interface, relaxes to its stable diffuse state. The mobility calculated in this work and the mobility in the diffuse interface models differ by units of length. The mobility is an inherently interfacial property, therefore it is expected that diffuse mobility scales with the MSD mobility and the interfacial thickness, $\gamma \sim ML_{int}$.

4.4 Conclusions

A method for calculating the fluid-fluid interfacial mobility using DCV-GCMD was developed. The mobility for three interfaces, two liquid-liquid interfaces and one liquid-vapor interface, was calculated using the variance of interface position, MSD, and VACF, showing excellent agreement between the three calculation methods. Domain size effects were explored and found to have negligible impact on the calculated mobility if data were analyzed at times shorter than the characteristic time of wave propagation across the domain. This method provides a new approach to obtain the mobility needed for diffuse interface continuum models of fluid-fluid interfaces [180–182]. Rather than being obtained as a fitted, [183–185] estimated [173], or swept parameter [172,179], it is directly obtained from physically justifiable molecular-scale calculations, similarly to other interfacial properties like surface tension and interface thickness.

4.5 Appendix

4.5.1 Choosing Chemical Potentials

It was observed in the initial DCV-GCMD simulations that interfaces in LL_2 and LV systems swept steadily across the domain, ultimately leading to the complete disappearance of one of the fluids and thus of the interfaces themselves. To enable analysis of interfaces and their random walks, it is important to choose chemical potentials that maintain the time-averaged interface velocity, v_{int}, and change in interface position, δx_{int}, at zero. Figure 4.7 illustrates the trial and error procedure used to attain appropriate chemical potentials for the LL_2 system. Normalized interface position versus time is shown for three different choices of μ_α, with μ_β held constant
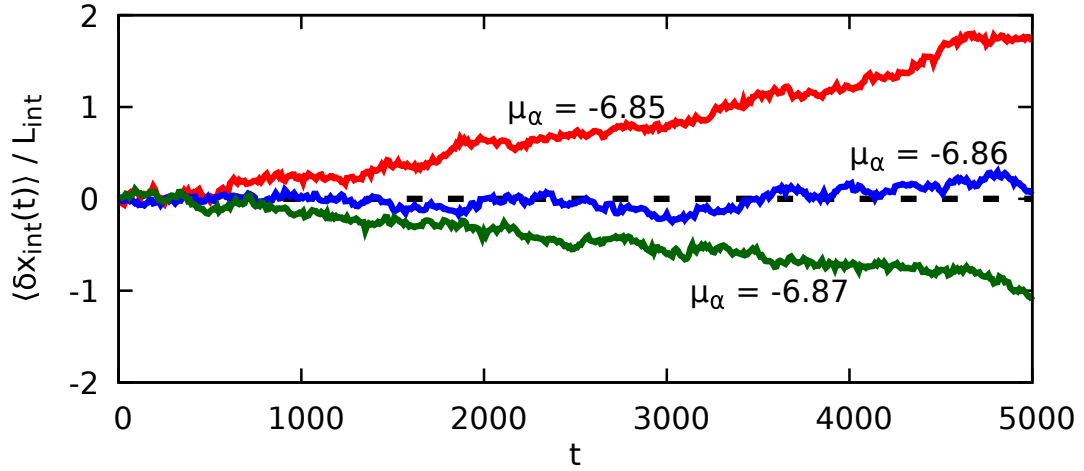
Fig. 4.7: Averaged normalized interface positions versus time for the LL_2 system for various chemical potentials.

at -8.14. Each of the three curves represents an average over three different initializations. It is evident that $\mu_\alpha = -6.86$ is the best choice to maintain a "stationary" interface. A similar procedure was performed for the LV system. For the LL_1 system, no trial and error was needed because both fluids were identical. All that was needed in that case to maintain a "stationary" interface was to set μ_α and μ_β equal.

At the end of n_{eq} MD time steps and before the DCV-GCMD portion of the simulations, the LL_2 system displayed an unexpected vapor layer at the interface between the bulk liquid α and β phases. This layer, roughly $0.1W$ thick and containing both α and β particles, likely arose due to the low number of particles initially chosen for α. Running DCV-GCMD caused bulk α and bulk β liquids to be driven toward one another, resulting in a steady decrease in vapor film thickness. After running 60000 DCV-GCMD steps the film was completely removed, and the linear velocity was removed from the system again before running DCV-GCMD for the mobility calculations.

4.5.2 Alternative definitions of Interface Position and Velocity

There are other potential ways to define x_{int} besides the "two-bin" method presented in the paper. One way, for systems with two species, is based on finding an extremum of total mass density $\rho_\alpha + \rho_\beta$. Figures 2(a) and (b) show that the total mass density exhibits a minimum very close to the value of x_{int} previously determined by setting $\rho_\alpha = \rho_\beta$. This minimum occurs because the repulsion between fluids α and β leads to a local depletion of particles in the interface. Still another way is to define x_{int} as the position where the local particle number density, as opposed to mass density, is equal to a target value. For the LL_1 and LV systems, this yields equivalent x_{int} values to those obtained using mass density because $m_\alpha = m_\beta$. For LL_2, this approach yields slightly different x_{int} values than those obtained from the mass density results in Fig. 2 because $m_\alpha \neq m_\beta$. Regardless of the slight differences in x_{int}, it was found that all three interface definitions give almost identical values for the diffusion coefficient, within 1.5%, in the MSD calculations which is less than the estimated error of roughly $\sim 5\%$.

To determine v_{int}, it is reasonable to use the average molecular velocity of particles in a region containing the interface. The key challenge is to determine the location and spatial extent of this region. Various calculations of v_{int} were performed using different interface regions. These included a region comprised of the two spatial bins used to interpolate the interface position x_{int} (shaded gray region in Fig. 2), a region comprised of the single spatial bin actually containing the interpolated x_{int}, regions centered on the interpolated x_{int} with "10-90", "5-95", and "1-99" interface thicknesses [191, 192], and regions whose interface positions and thicknesses were determined by fitting a hyperbolic tangent to the density profile [85]. For the latter two interface regions, which generally spanned multiple bins and had boundaries that did

not align perfectly with the bin edges, the contribution of each bin to the average v_{int} was weighted by the fraction of the bin contained by the interface.

For the hyperbolic tangent method, the interface thickness L_{int} of the LV system was obtained, along with the interface position, from the following commonly used fitting function

$$\rho(x) = \frac{\rho_L + \rho_V}{2} - \frac{\rho_L - \rho_V}{2} \tanh\left(\frac{2(x - x_{int})}{L_{int}}\right). \tag{4.4}$$

The interface thicknesses of the LL_1 and LL_2 systems were more complicated to determine because fluids α and β are different species. The density profiles of each species were separately fitted to the following equations

$$\rho_\alpha(x) = \frac{\rho_\alpha^B}{2}\left(1 - \tanh\left(\frac{2(x - s_\alpha)}{L_\alpha}\right)\right) \tag{4.5a}$$

$$\rho_\beta(x) = \frac{\rho_\beta^B}{2}\left(1 + \tanh\left(\frac{2(x - s_\beta)}{L_\beta}\right)\right) \tag{4.5b}$$

and the overall interface thickness of the two-species was calculated from the interface thicknesses and positions of the individual species (Table 4.4) as

$$L_{int} = \left(s_\beta + \frac{L_\beta}{2}\right) - \left(s_\alpha - \frac{L_\alpha}{2}\right). \tag{4.6}$$

In the above, ρ_α^B and ρ_β^B (Table 4.3) are the bulk densities of α and β far from the interface. To fit the data, instantaneous density profiles were recorded at each time step, aligned about their interface positions, time averaged over $0.1n_{run}$ time steps, and ensemble averaged over N_s initializations. This procedure gave the fitting parameters and interfacial thicknesses in Eqs. 4.4-4.6; numerical values for these parameters are found in Table 4.4.

Table 4.4: Fitted values for the LL_1 and LL_2 density profiles. The ($\cdot$) represents the uncertainty in the preceding digit.

	L_α	L_β	s_α	s_β
LL_1	1.97(3)	1.97(3)	-0.292(8)	0.292(8)
LL_2	2.38(2)	2.15(2)	-0.206(6)	0.506(7)

It was found that the two bin region yielded velocity autocorrelation based mobility values that agreed very well with those computed using other methods based on mean squared interface displacement and variance of interface position for all three systems. The single bin and hyperbolic tangent methods performed similarly to the two bin method, however the uncertainty in the single bin method was roughly twice that of the two bin method. For the 10–90, 5–95, and 1–99 methods, respectively, the interface thickness increased and the calculated mobilities decreased to a value 11% lower (for the 1-99 method) than the mobility value calculated from the two bin method.

It is believed that the 1-99 method (and to a lesser extent the 5–95 and 10–90 methods) yields interfaces that are too wide, incorporating significant numbers of bulk-like non-interface particles. These particles move much less readily than interface particles, leading to lower average interfacial velocities and lower VACF values. For these reasons the 1–99 method is not recommended. Due to its agreement with other mobility calculation methods and to its computational simplicity, the two-bin method is the preferred method for v_{int} calculations and is used for all calculations presented in the manuscript.

4.5.3 Boundary and Domain Size Effects

It is also important to ensure that the interface motion does not include artifacts arising from domain size and boundary conditions. Figure 4.8 shows MSD-related data computed for LL_1 systems of three different sizes: a baseline domain of volume $W \times A$, a wide domain of volume $2W \times A$, and a small cross section domain of volume $W \times A/2$. Since mobility scales with the time derivative of the product of MSD and cross sectional areas (Eq. 1), this product is plotted rather than the MSD itself. Similarities for all three domain sizes are evident for times less than approximately 25 time units, but beyond that the two domains with width W both show a reduction in slope of MSD $\times A$. The domain with width $2W$ also shows a reduction in slope, but at approximately 50 time units. Similar MSD results (not shown) were obtained for LL_2 and LV systems. These reductions in slope occur at times consistent with the time it takes a sound wave to cross the domain and interact with the RBC boundary: $\tau = W/c$ or $2W/c$. Using the speed of sound for a LJ fluid at $T = 0.7$ from Haile [86], the estimated interaction times are $\tau \approx 20$ and 40, which is roughly when deviations begin. Due to the similarities in the MSD$\times A$ for all three cases below 25 time units, it is expected that the domain size, both length and area, will have negligible effects on mobility, if data are taken before this characteristic time. Accordingly, all mobility calculations in this work are based on time windows shorter than τ.

The motivation for running DCV-GCMD as opposed to normal MD in this paper was that MD simulations were initially tried but showed unexpected artifacts. These artifacts took the form of regular oscillations with a well defined period, roughly 2τ, for domains of width W ("MD" curve in Fig. 4.8). These oscillations arose from periodic compression and expansion of the confined fluid as it moved back and forth between the domain boundaries. Compression of the liquid is difficult due to its high
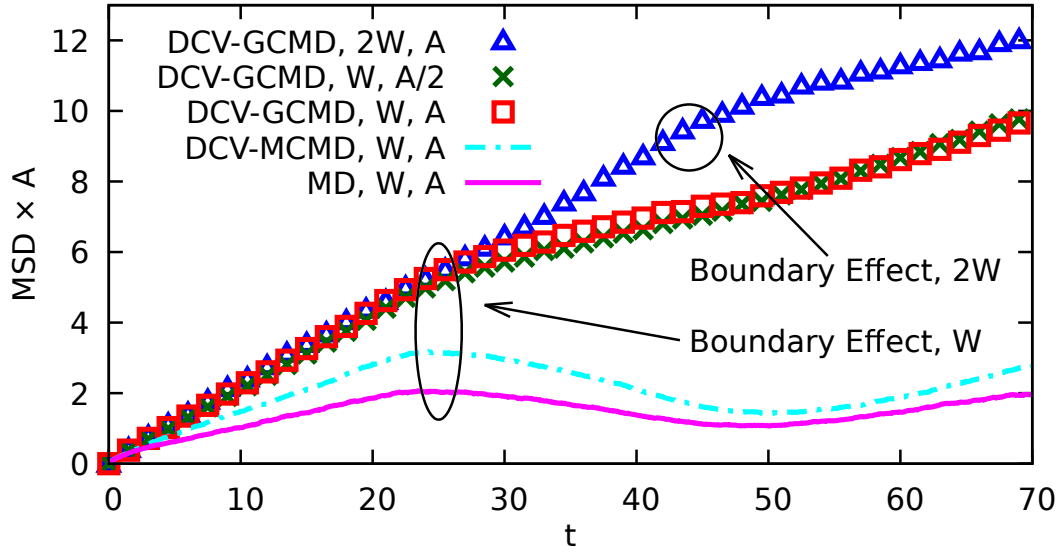
Fig. 4.8: Mean squared displacement multiplied by the cross sectional area versus time for the LL_1 interface for various domain sizes and computational methods. MD simulations correspond to setting $k_t = k_{id} = 0$ in the DCV-GCMD simulations, while DCV-MCMD simulations correspond to setting $k_{id} = 0$. Error bars, not shown, are similar in size to the markers.

density, leading to suppression of the interface trajectory (Fig. 4.9) and reduction of MSD (Fig. 4.8). Similar results on boundary-induced suppression of the diffusion coefficient, which is related to the MSD of individual atoms, have previously been reported [210, 211]. MD simulations with Monte Carlo translation steps were tried next in order to permit the particles to access lower energy configurations, with the goal of reducing the resistance of the liquid to interface motion. While the observed displacements and MSD values were higher ("DCV-MCMD" curve, Figs. 4.8 and 4.9), the MSD still displayed the undesired oscillatory behavior. It was decided to introduce particle sources and sinks at the boundaries via DCV-GCMD simulations, in the hope that this would allow free movement of the liquid and thereby eliminate the fluid compression effect of the confining walls. The oscillatory behavior was indeed eliminated. The boundary effect also appears in the VACF and more noticeably in

the integral of the VACF as seen in Fig. 4.10 which is a modified version of Fig. 4.5 in the main text that has been extended to longer time to illustrate the boundary effect.
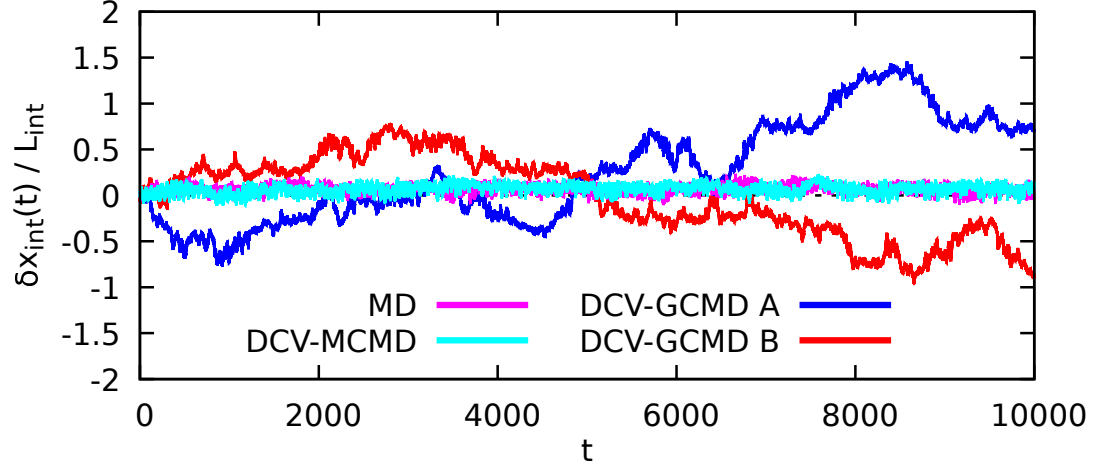
Fig. 4.9: Interface trajectories for the LL_1 system. Interface position is normalized by the interfacial thickness. MD simulations correspond to setting $k_t = k_{id} = 0$ in the DCV-GCMD simulations, while DCV-MCMD simulations correspond to setting $k_{id} = 0$. "A" and "B" for the DCV-GCMD simulations indicate different velocity initializations.
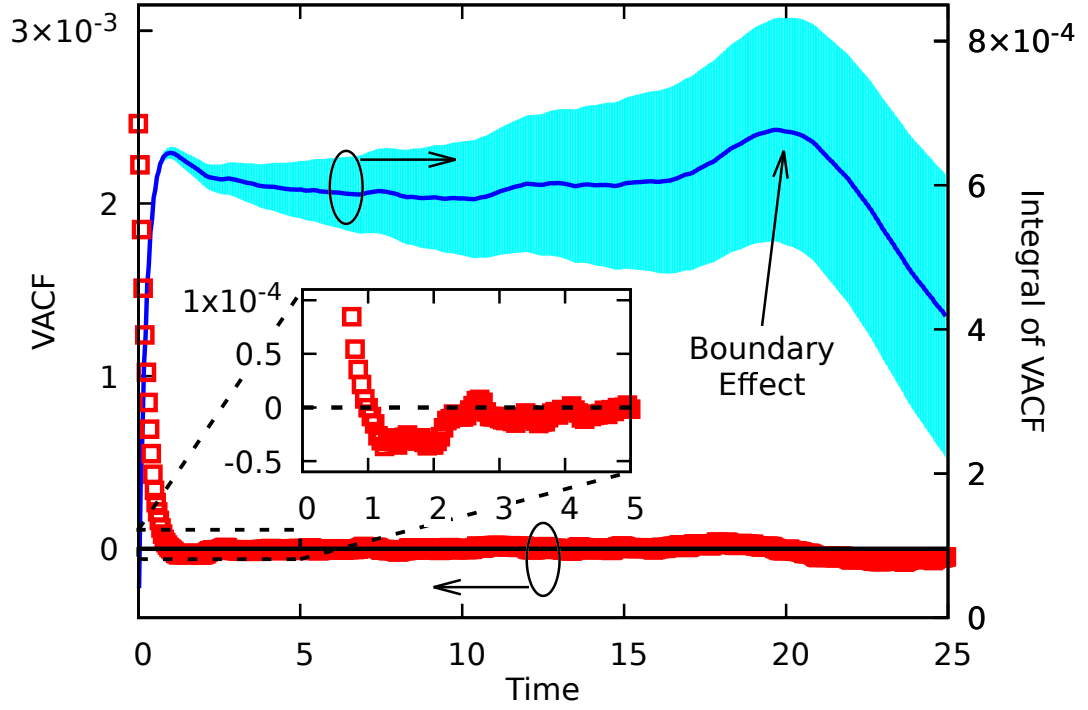
Fig. 4.10: VACF (left axis, red square) and the integral of the VACF (right axis, blue line) versus time from the LL_1 interface. Error bars for the VACF are similar in size to the markers while the error for the integral of the VACF is shown with the shaded region. Inset shows a finer resolution of the VACF.

5 Relationship between Interfacial Mobility and Cahn-Hilliard Fluid Phase Mobility

Chapter 4 established a molecular dynamics method to calculate the interfacial mobility between two fluids so that it could be used as an *a priori* input for continuum models. This chapter expands upon the continuum definition of the diffuse interfacial mobility γ used in the Navier-Stokes-Cahn-Hilliard equations and relates it to the fluctuation mobility M calculated in Chap. 4. The remainder of this chapter is as follows: Sec. 5.1 further expands upon the continuum background established in Chap. 2.3, Sec. 5.2 discusses equilibrium MD simulations and steady state continuum simulations, Sec. 5.3 discusses non-equilibrium MD simulations and transient continuum simulations of interfacial relaxation, and Sec. 5.4 makes a few final remarks and draws conclusions about interfacial mobility.

5.1 Continuum Background

5.1.1 Navier-Stokes-Cahn-Hilliard Equations

The incompressible Navier-Stokes-Cahn-Hilliard (NSCH) equations, a modified version of Eqs. 2.28, which are commonly used when modeling droplet motion [47, 172, 173, 179–185] are given by

$$\nabla \cdot \mathbf{v} = 0 \tag{5.1a}$$

$$\rho \frac{D(\mathbf{v})}{Dt} = -\nabla p + \eta \nabla^2 \mathbf{v} + \mathbf{F}_\sigma \tag{5.1b}$$

$$\frac{D\alpha}{Dt} = \gamma \nabla^2 \mu \tag{5.1c}$$

where $\mathbf{v}$ and p are the fluid velocity and pressure, α is the fluid phase fraction (not to be confused with the accommodation coefficient α in Chap. 3) with $\alpha \in [0, 1]$ where $\alpha = 0$ and $\alpha = 1$ represents the vapor V and liquid L phases, formerly fluid phases A and B in Chap. 2. Here ρ and η are the fluid density and viscosity which are a weighted average of the bulk values, $\rho(\alpha) = \rho_V + \alpha(\rho_L - \rho_V)$ and $\eta = \eta_V + \alpha(\eta_L - \eta_V)$, $\mathbf{F}_\sigma$ is the surface tension term, and μ is the chemical potential. Gurtin [212] proposed the following surface tension model, $\mathbf{F}_\sigma = \mu \nabla \alpha$, where the Cahn-Hilliard chemical potential is defined by

$$\mu = \mu_w + \mu_g = k_w \left(\alpha^3 - \frac{3\alpha^2}{2} + \frac{\alpha}{2} \right) - k_g \nabla^2 \alpha. \tag{5.2}$$

Here μ_w and μ_g represent contributions to the free energy from the phase fraction and gradient of the phase fraction with strength k_w and k_g respectively. The first term in Eq. 5.2 is a derivative of a symmetric double well potential for the Gibbs free energy G shown in Fig. 5.1 and given by the expression, $G = k_w \alpha^2 (\alpha - 1)^2 / 4$, while the second term arises by keeping the first non-zero term in an expansion of the free energy about the phase fraction [213]. μ_w arises from an energetic penalty for the fluid not being in the pure vapor or liquid state, $\alpha = 0$ or $\alpha = 1$, while μ_g is an energetic penalty for having sharp changes in phase. The balance between μ_w and μ_g allows for a diffuse interface to form with finite thickness L_{int}. The strength of the energetic well and phase gradient energy are related to the interfacial length and the surface tension σ_{ST} by [47, 182–184]

$$k_g = \frac{3\sqrt{2}\sigma_{ST} L_{int}}{2} \tag{5.3a}$$

$$k_w = \frac{6\sqrt{2}\sigma_{ST}}{L_{int}}. \tag{5.3b}$$

102
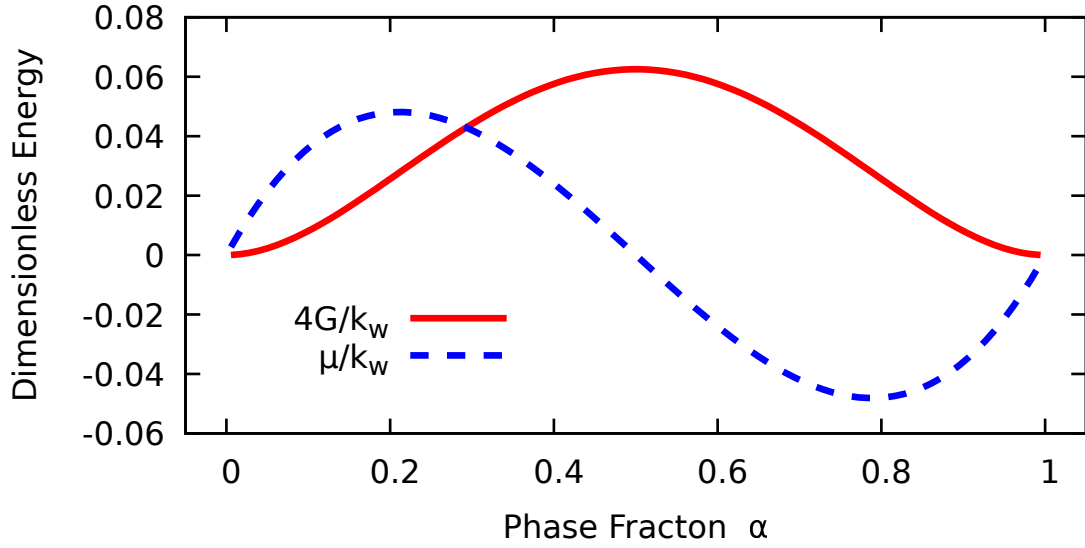
Fig. 5.1: Bulk Gibbs free energy $4G/k_w$ (solid line) and chemical potential μ/k_w (dashed line) as a function of phase fraction for the Cahn-Hilliard symmetric double well.

Other surface tension models are also used in the literature [214–217], but the Gurtin model is the most common.

A benefit of the symmetric double well free energy G is that there exists an analytical steady state solution for the interfacial profile α_s [218, 219],

$$\alpha_s(x) = \frac{1}{2}\left(\tanh\left(\frac{x}{\sqrt{2}L_{int}}\right) + 1\right). \tag{5.4}$$

Although a steady state solution is beneficial, a symmetric double well potential is only an approximation for the chemical potential of a Lennard Jones fluid [220, 221]. Adjusting the free energy to an asymmetric fourth order double well leads to issues discussed in Sec. 5.5. Higher order energetic wells are beyond the scope of this dissertation; therefore, the symmetric double well potential will suffice.

103

5.1.2 Navier-Stokes-Cahn-Hilliard Mobility

The mobility γ in the diffuse interface model of the NSCH equations stems from a linear force-flux relation [181] and has units of $Length^3 \times Time \times Mass^{-1}$. The mobility M in Chap. 4 stems from random fluctuations of the interface using either the mean-square displacement or a Green-Kubo style integration of the interfacial velocity autocorrelation function and has units of $Length^2 \times Time \times Mass^{-1}$. These mobilities M and γ are both inherently interfacial properties, therefore it is expected that diffuse mobility γ scales with the fluctuation mobility M. The interfacial thickness L_{int} provides a connection between the two mobilities, and it is expected that $\gamma \sim M L_{int}$.

Equilibrium MD has been used to calculate transport coefficients such as viscosity and thermal conductivity [85]. Alternatively, non-equilibrium MD combined with analytical continuum solutions has been used to extract viscosity [222] and thermal conductivity [223, 224]. Similar to these examples, Chap. 4 establishes an equilibrium method to extract interfacial mobility while this chapter extracts the mobility from non-equilibrium simulations. These methods to calculate the mobility are similar to the equilibrium and non-equilbrium methods to calculate other physical properties such as the viscosity and thermal conductivity. Therefore the extracted values for γ from the interfacial relaxation simulations are expected to be related to the equilibrium mobility M from Chap. 4.

5.2 Steady State Interface

Before interfacial relaxation simulations are performed, steady state validation of the continuum equations in Sec. 5.3.2 must be discussed. MD simulations were

run to gather physical properties needed as inputs for the continuum computational fluid dynamics (CFD) simulations. CFD simulations were performed using the open source software OpenFOAM [225, 226] with an in house solver for the NSCH equations. The solver used an implicit Euler time stepping scheme and linear Gaussian discretization scheme for the spatial domain. Alternative higher order time stepping schemes such as Runge-Kutta or Dormand-Prince and higher order discretization schemes had minimal effects on the numerical results; therefore the above methods were chosen to reduce computation time. Note both MD and CFD simulations are run in dimensionless Lennard-Jones units and all values presented in this chapter are dimensionless unless otherwise noted.

5.2.1   Molecular Domain Simulations

A dimensionless, truncated and shifted Lennard-Jones potential was used for all interactions. Initially $N = 12000$ particles were placed in a domain of $L \times H \times H$, and Table 5.1 shows the domain sizes for the liquid-vapor simulations which were chosen such that there would be approximately 10000 liquid particles and 2000 vapor particles based on the bulk densities from the literature [162]. More particles were placed in the center of the domain to allow for the liquid film to form in a reasonable initialization period. The system was allowed to equilibrate to a temperature T for $N_{equil} = 4.5 \times 10^6$ steps with a time step $\Delta t = 0.005$. Rescaling thermostats were used to control T in two regions, one in the center portion of the liquid film and one in the center of the vapor region. The size of the thermostatted region was such that roughly 200 particles were thermostatted at every time step. Periodic boundary conditions were implemented in all directions so two liquid-vapor interfaces formed

Table 5.1: Temperatures, domain size, bulk densities, bulk viscosities, surface tension, and interface width for the liquid-vapor interface relaxation simulations.

T	L	H	ρ_L	$\rho_V(\times 100)$
0.7	3769.30	12	0.81 ± 0.07	0.35 ± 0.04
0.8	1254.17	12	0.77 ± 0.07	1.07 ± 0.15
0.9	594.83	12	0.71 ± 0.07	2.54 ± 0.33
1.0	357.71	12	0.65 ± 0.07	4.77 ± 1.19
T	η_L	$\eta_V(\times 100)$	σ	L_{int}
0.7	2.61 ± 0.19	0.87 ± 0.16	0.71 ± 0.53	0.579 ± 0.006
0.8	1.76 ± 0.11	2.92 ± 0.36	0.60 ± 0.53	0.719 ± 0.006
0.9	1.27 ± 0.09	6.35 ± 0.38	0.46 ± 0.52	0.917 ± 0.007
1.0	0.97 ± 0.06	9.53 ± 0.55	0.23 ± 0.52	1.199 ± 0.010

in the simulation domain. The phase fraction α for the liquid-vapor systems is

$$\alpha(x) = \frac{\rho(x) - \rho_V}{\rho_L - \rho_V}. \tag{5.5}$$

The bulk liquid and vapor densities and surface tension (Table 5.1) as well as the average interface profile were calculated during the last $N_{ave} = 10^6$ steps. The steady state phase solution, Eq. 5.4, was used to extract the interfacial length L_{int}. The bulk viscosities, η_L and η_V, for the liquid and vapor phases were calculated using Eq. 2.58 in separate MD simulations at the corresponding temperature and densities.

5.2.2 Continuum Domain and Comparison

With the equilibrium MD complete, steady CFD simulations were performed in order to model the Lennard Jones liquid-vapor interface. Bulk properties were taken from the MD averages and the domain sizes were the same size as the MD

simulations, Table 5.1. The initial α values for the CFD simulation were taken from the MD steady state solution. Note that the MD α, Eq. 5.5, does not strictly limit $\alpha \in [0, 1]$ so when needed, the values of α were truncated. Near the interfaces and in the liquid domain, a spatial grid resolution of $\Delta x = 0.25$ was used, while a slightly larger spatial grid resolution was used for the remainder of the vapor domain. Studies were performed with finer spatial grid resolutions and minimal differences were seen in the numerical results. Simulations were run with various values of γ in order to allow the continuum solver to relax to the desired steady state solution. Regardless of the γ value used, the solver converged to a similar steady state profile after a short simulation time (as expected since the initial condition is very close to the equilibrium profile and is independent of γ). The time step for the CFD solver was the same as the MD time step, and the simulations were run until the phase profile was steady with time. Figure 5.2 shows the steady state MD and CFD profiles as well as the analytical solution, Eq. 5.4. Excellent agreement is seen between the MD and continuum data for all temperatures. Furthermore, the minimal differences between the CFD results and analytical solutions in Figs. 5.2 indicate that the numerical CFD model is implemented correctly and accurately capturing the steady state physics of the NSCH equations (Eq. 5.1).

In order to quantitatively examine the differences between the MD and continuum simulations, the steady state merit function χ_s is defined as

$$\chi_s(x) = \left(\alpha_{MD}(x) - \alpha_{CFD}(x)\right)^2.$$ (5.6)

Figure 5.3 shows the merit function versus position, and the small values of χ_s confirm that Eq. 5.4 accurately represents the steady state solution for the Lennard Jones liquid-vapor interface at the temperatures simulated. Furthermore the peaks in Fig.
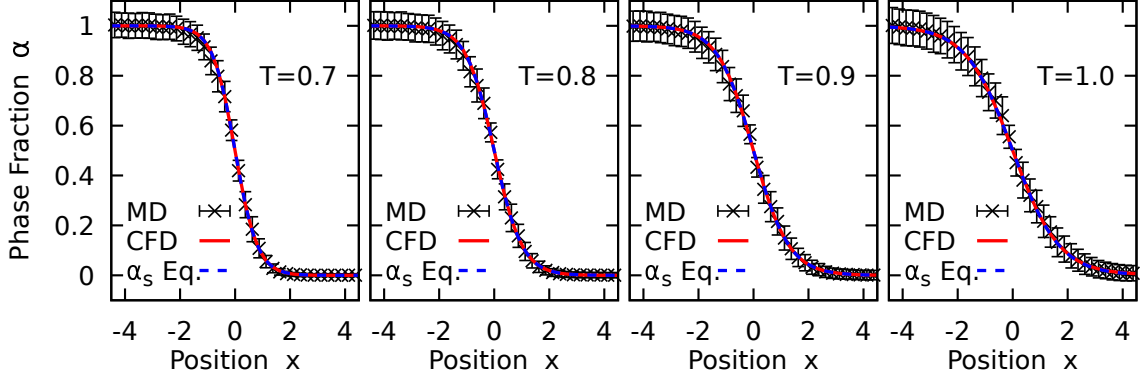
Fig. 5.2: MD, CFD, and analytical steady state equation for α_s (Eq. 5.4) results for the phase fraction α profiles at various temperatures for a Lennard Jones fluids.
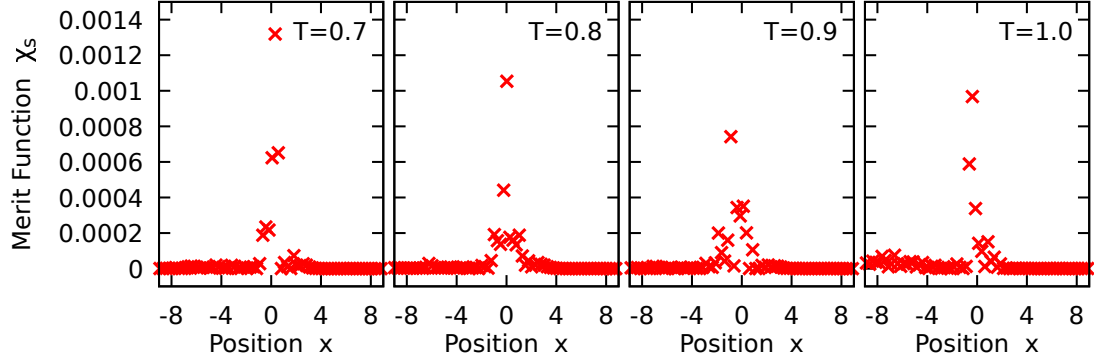
Fig. 5.3: CFD merit function (Eq. 5.6) at various temperatures.

5.3 indicate that the merit function has non-negligible values only near the interfacial region. This result is expected as the bulk phases in the continuum model are well represented by the NSCH model.

5.3 Interfacial Relaxation Simulations

With the verification of the steady state solutions, relaxation of a stretched interface were performed. Based upon Eq. 5.4, every interface has a natural resting shape (a hyperbolic tangent) and width L_{int} over which the phase fraction α smoothly changes from one phase to another. Therefore if perturbed from this natural state,
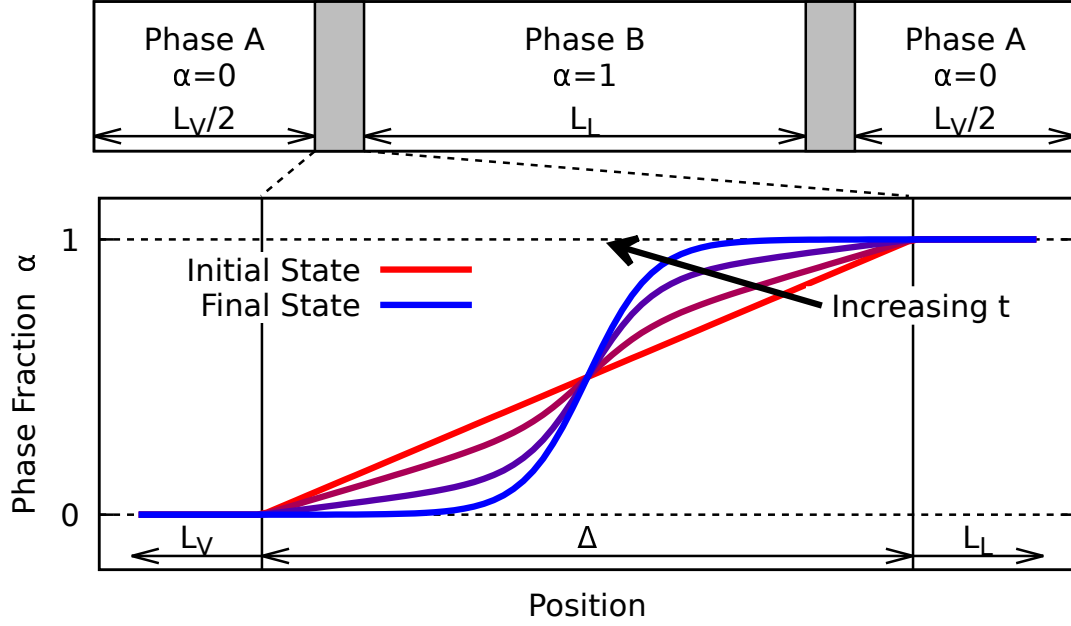
Fig. 5.4: Schematic for interface relaxation simulations. The entire domain (top) and detailed representation of the transition region (bottom). Lines in the bottom figure show potential interface states.

an interface will relax to its desired length and the key parameters governing this transition are the surface tension σ and the interfacial mobility γ. A simple way to extract γ is to stretch the interface in one dimension at several values of γ and find the value of γ which minimizes some merit function. Figure 5.4 shows a schematic of a natural interface profile as well as the perturbed linear interface used to extract γ for the Lennard-Jones fluid.

5.3.1 Molecular Simulations

In order to simulate the stretched interface in Fig. 5.4, MD simulations were run in the following manner. Interface profiles taken during the steady state averaging in Sec. 5.2.1 were used as the initial configurations for the MD domain. At $t = 0$, particles were removed in the region $\Delta = 10L_{int}$ in order to create the desired linear

profile on either side of the liquid film. Table 5.2 contains the geometric data for the relaxation simulation in Fig. 5.4. Besides the removal of particles from the domain, all other values from the equilibrium MD simulations were used.

Table 5.2: Geometric information for interface relaxation simulations.

T	L_L	L_V	Δ	$L_L + L_V + 2\Delta$
0.7	75.96	3681.76	5.79	3769.30
0.8	79.40	1160.39	7.19	1254.17
0.9	82.96	493.53	9.17	594.83
1.0	87.59	246.14	11.99	357.71

Normal MD was then run for $N_{run} = 50000$ steps with data collected every $N_d = 50$ steps. For all temperatures studied, this was sufficient time for the interfacial profile to relax to its desired length. This process was then repeated $N_t = 50$ times in order to gather appropriate temporal statistics on the interfacial relaxation. Figure 5.5 shows the average interface profile at various times and temperatures. All of the profiles rapidly converge to a steady profile and fluctuate about their equilibrium profile as expected. Note that the colder temperatures which have sharper interfaces converge more rapidly to the appropriate steady state solution than the higher temperature interfaces. This is due to the higher surface tension and larger difference between the liquid and vapor phases at colder temperatures.

5.3.2 Continuum Domain and Molecular Comparison

Continuum simulations were run in the following manner. The MD averaged initial linear α profile was used as the initial condition for the phase fraction. Simulations were then run with various values of γ in order to determine which value of
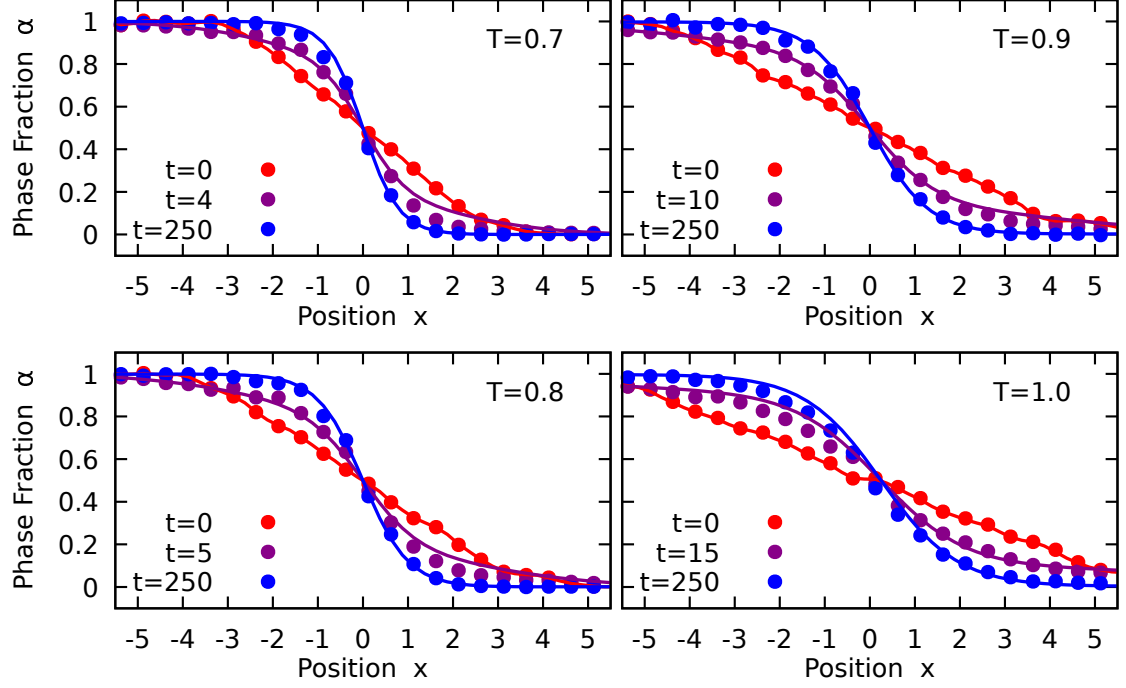
Fig. 5.5: Phase fraction at various times and temperatures for MD (points) and CFD (lines). Values for γ can be found in Table 5.3. Error bars for MD data are slightly larger than marker size and were left out for clarity.

γ best matched the MD simulations. Figure 5.5 compares the MD and CFD simulations at various times and temperatures. A reasonable agreement between the two methods can be seen for the given time snapshots.

In order to quantify the difference between MD and CFD, the instantaneous merit function

$$\chi_t(x,t) = (\alpha_M(x,t) - \alpha_C(x,t))^2 \tag{5.7}$$

is defined, similar to the steady state merit function χ_s. Figure 5.6 show χ_t at various time snap shots. The difference between the MD and CFD is higher than the steady state counterpart, but χ_t is still reasonably small for "good" values of γ (the definition of "good" will be defined later). The overall agreement in trends between the MD and CFD results lends confidence that the Lennard Jones fluids is accurately represented
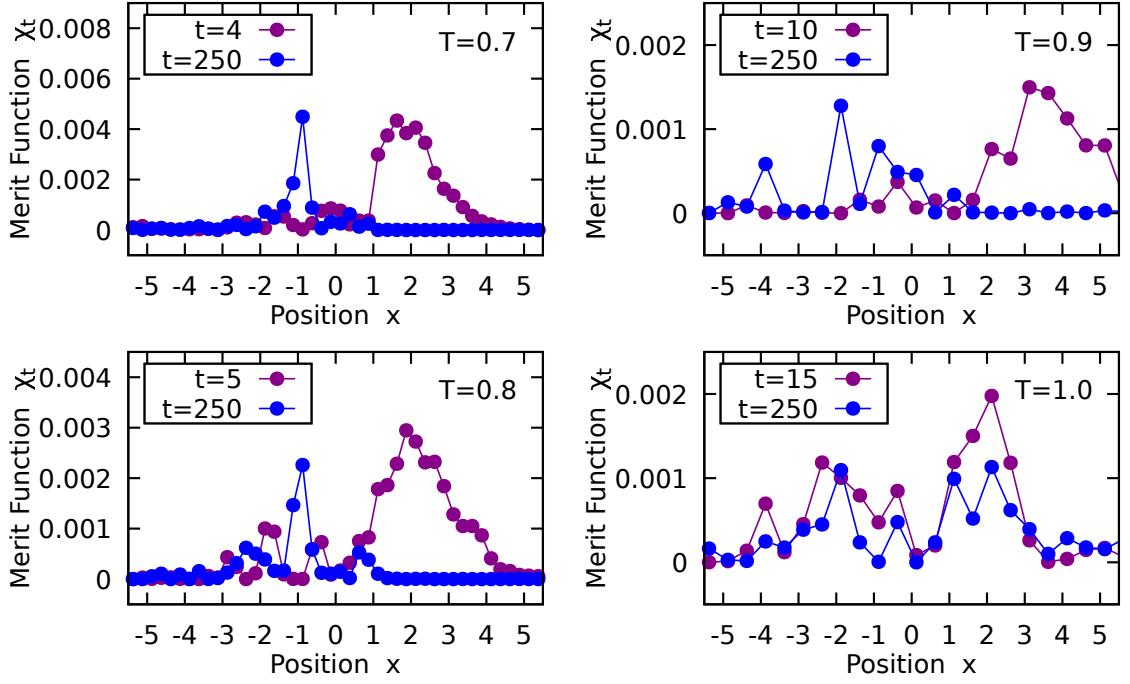
Fig. 5.6: Instantaneous merit function (Eq. 5.7) comparing MD and CFD data. Values for γ can be found in Table 5.3.

by the NSCH model.

The mobility γ is a required input for the continuum model, and it is not known *a priori* which value matches the MD data the best for the entire spatial domain. Therefore, several values of γ were run for each temperature, and the transient merit function χ was used to determine the optimal value of γ by finding which value of γ minimized χ with the overall transient merit function defined as

$$\chi = \sum_t \sum_x w(x,t)\chi_t(x,t). \tag{5.8}$$

Here $w(x,t)$ is a weighting function. Since the MD and CFD start and end at similar conditions the weights for these times should be minimal, therefore the weighting

Table 5.3: Optimal values for the mobility γ from the CFD simulations and from a polynomial fit which minimized the merit function χ.

T	γ_{min}	γ_{min}^{fit}
0.7	0.13	0.1341
0.8	0.23	0.2274
0.9	0.40	0.4045
1.0	1.7	1.6616

function

$$w(x,t) = (\alpha_M(x,0) - \alpha_M(x,t))^2(\alpha_M(x,\infty) - \alpha_M(x,t))^2 \qquad (5.9)$$

was used because it has larger penalties for being dissimilar to the MD solution while the interface is transitioning. Figure 5.7 shows the ratio $\chi(\gamma)/\chi(\gamma_{min})$ where γ_{min} is the value of γ that minimizes a cubic polynomial fit of χ function. Each temperature has a clear minimum in χ indicating that there exists an optimal value for γ which minimizes the differences between the MD and CFD solutions. Table 5.3 lists the values of γ which minimized χ at a given temperature.

Figure 5.8 shows the optimal diffuse mobilities γ as a function of temperature. This temperature dependence of γ indicates that γ can be interpreted as a temperature dependent interfacial property for a given fluid-fluid interface similar to surface tension and interfacial length. Figure 5.8 also shows ML_{int} for $T = 0.7$ from Chap. 4. The similarity between γ and ML_{int} for $T = 0.7$ lends confidence to the hypothesis that $\gamma \sim ML_{int}$. However, robust conclusions on this result should be further verified by performing equilibrium simulations at additional temperatures. Furthermore, compressibility or phase dependent mobility could be incorporated into the NSCH in order to more accurately represent the Lennard Jones fluid, but these ideas are beyond the scope of this dissertation.
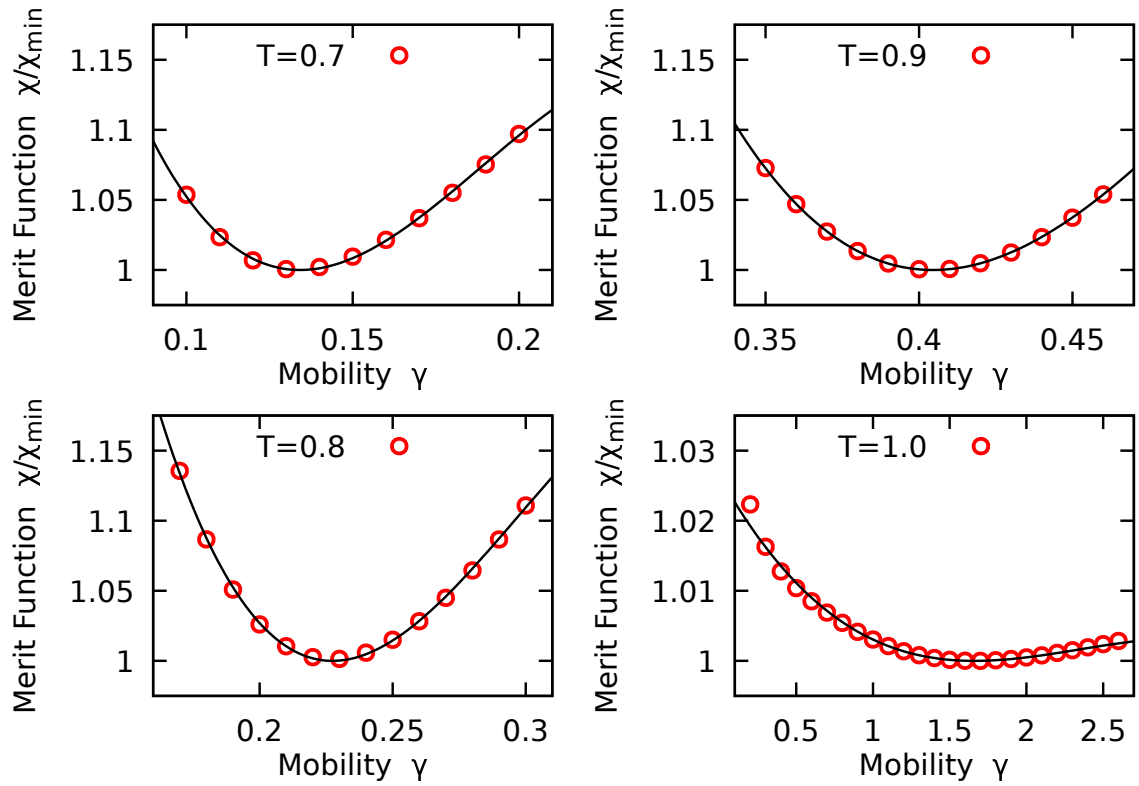
Fig. 5.7: Merit functions comparing MD and CFD data for various values of mobility γ. Each temperature clearly has a distinct minimum indicating there exists an optimal value of γ. Solid lines are cubic polynomial fits of the data.
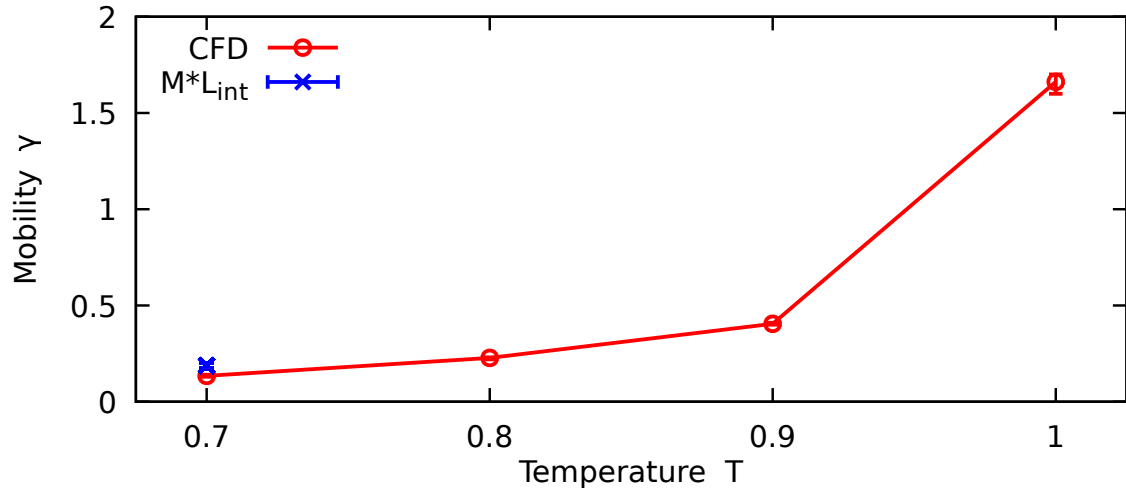
Fig. 5.8: Mobility as a function of temperature T. Optimal values from CFD simulations are red circles while blue crosses are the mobility M calculated in Chap. 4 multiplied by the interfacial length L_{int}. Error markers that are not shown are similar to marker size.

5.4   Conclusions

The this chapter establishes a method to obtain a value of mobility γ needed for the NSCH model (Eq. 5.1) from a combination of molecular and continuum simulations. First equilibrium MD simulations of a Lennard Jones liquid-vapor interface at several temperatures was performed in order to extract bulk densities and viscosities as well as surface tensions and interfacial lengths. Steady state continuum simulations were performed on the NSCH model to verify the validity of the NSCH model for the Lennard Jones fluid. With the validity of the equilibrium/steady state model, non-equilibrium/transient simulations of interfacial relaxation from a unnatural linear state to its desired profile were performed in both MD and CFD. A global merit function was defined in order to extract a "best" value for the continuum mobility γ. Finally, a brief discussion of the relationship between the diffuse mobility γ and the fluctuation mobility M was made with $\gamma \sim ML_{int}$.

5.5   Appendix: Asymmetric Double Well

This appendix will discuss using an asymmetric double well as an alternative to the symmetric double well free energy, $G = k_w\alpha^2(\alpha - 1)^2/4$. The symmetric fourth order well is assumed as it has an analytical steady state solution (Eq. 5.4). However, it may not accurately represent a Lennard-Jones liquid-vapor interface because the liquid and vapor phases are identical, therefore the Gibbs free energy G may not be perfectly symmetric. The simplest way to model this asymmetry would be with an asymmetrical fourth order free energy G_{asym}. Note that the mathematical software Mathematica [227] was heavily used throughout this portion.

An asymmetric fourth order double well free energy and chemical potential can
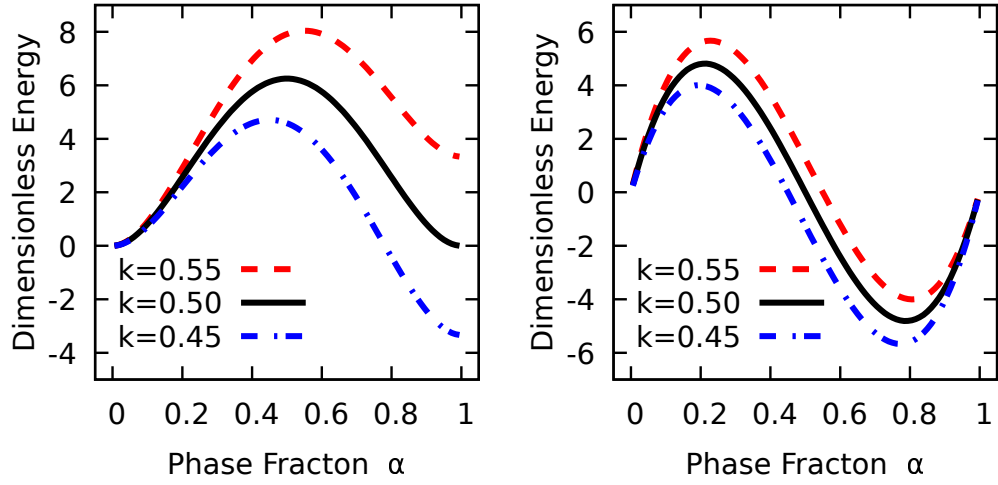
Fig. 5.9: Dimensionless asymmetric Gibbs free energy $100G_{asym}/k_w$ (left) and chemical potential $100\mu_{asym}/k_w$ (right) as a function of phase fraction α for select values of asymmetry k.

be written as

$$G_{asym} = k_w \alpha^2 \left(\frac{\alpha^2}{4} - \frac{(1+k)\alpha}{3} + \frac{k}{2} \right) \tag{5.10a}$$

$$\mu_{asym} = k_w \alpha (\alpha - 1)(\alpha - k) \tag{5.10b}$$

where $k \in [0,1]$ and $k = 1/2$ results in the symmetric double well. Figure 5.9 shows the asymmetric free energy and chemical potential at select values of k. While deriving α_s [218, 219], Eq. 5.4 assumes that

$$\alpha(x) = a_0 + a_1 w(x) + \frac{a_2}{w(x)} \tag{5.11}$$

where a_i are constants and $w(x)$ satisfies the Riccati equation

$$w'(x) = bw(x) + w^2(x) \tag{5.12}$$

116

where b is a constant and $'$ denotes differentiation with respect to x. Equation 5.12 has the general solution

$$w(x) = \frac{1}{2}\left(-b + \sqrt{-b^2}\tan(\sqrt{-b^2}x)\right). \tag{5.13}$$

Plugging Eq. 5.11 into Eq. 5.1c and assuming steady state while using Eq. 5.12 to remove all $w'(x)$ results in a set of nine equations by matching powers of w^i with $i = -3, -2, ..., 4, 5$ that must be zero. In order to satisfy the steady state solutions Eq. 5.1c, the following equations must hold:

$$-9a_2^3 b^2 k_w = 0 \tag{5.14a}$$

$$-15a_2^3 bk_w - 12a_0 a_2^2 b^2 k_w + 4a_2^2 b^2(1+k)k_w = 0 \tag{5.14b}$$

$$a_2 b^4 k_g - 6a_2^3 k_w - 18a_0 a_2^2 bk_w - 3a_0^2 a_2 b^2 k_w - 3a_1 a_2^2 b^2 k_w - a_2 b^2 kk_w$$
$$+6a_2^2 b(1+k)k_w + 2a_0 a_2 b^2(1+k)k_w = 0 \tag{5.14c}$$

$$a_2 b^3 k_g - 6a_0 a_2^2 k_w - 3a_0^2 a_2 bk_w - 3a_1 a_2^2 bk_w - a_2 bkk_w + 2a_2^2(1+k)k_w$$
$$+2a_0 a_2 b(1+k)k_w = 0 \tag{5.14d}$$

$$a_1 b^4 k_g - 3a_0^2 a_1 b^2 k_w - 3a_1^2 a_2 b^2 k_w - a_1 b^2 kk_w + 2a_0 a_1 b^2(1+k)k_w = 0 \tag{5.14e}$$

$$15a_1 b^3 k_g - 9a_0^2 a_1 bk_w - 9a_1^2 a_2 bk_w - 12a_0 a_1^2 b^2 k_w - 3a_1 bkk_w$$
$$+6a_0 a_1 b(1+k)k_w + 4a_1^2 b^2(1+k)k_w = 0 \tag{5.14f}$$

$$50a_1 b^2 k_g - 6a_0^2 a_1 k_w - 6a_1^2 a_2 k_w - 30a_0 a_1^2 bk_w - 9a_1^3 b^2 k_w - 2a_1 kk_w$$
$$+4a_0 a_1(1+k)k_w + 10a_1^2 b(1+k)k_w = 0 \tag{5.14g}$$

$$60a_1 bk_g - 18a_0 a_1^2 k_w - 21a_1^3 bk_w + 6a_1^2(1+k)k_w = 0 \tag{5.14h}$$

$$24a_1 k_g - 12a_1^3 k_w = 0. \tag{5.14i}$$

The solutions to Eq. 5.14 are of the form

$$b = \pm \sqrt{\frac{2k_w}{3k_g}(k^2 - k + 1)} \tag{5.15a}$$

$$a_0 = \frac{1}{3}\left(1 + k \pm \sqrt{3(k^2 - k + 1)}\right) \tag{5.15b}$$

$$a_1 = \pm\sqrt{2k_g/k_w} \tag{5.15c}$$

$$a_2 = 0. \tag{5.15d}$$

Note that taking the combinations of $\{-,-,-\}$ or $\{-,+,+\}$ for the $\pm$ operators in Eqs. 5.15a, 5.15b, and 5.15c respectively are not solutions but all remaining combinations for the $\pm$ operator are solutions. Plugging 5.15 into Eq. 5.11 and using Eq. 5.13 results in

$$\alpha(x) = \frac{1}{3}\left(1 + k + \sqrt{3(k^2 - k + 1)}\tanh\left(x\sqrt{\frac{k_w}{6k_g}(k^2 - k + 1)}\right)\right). \tag{5.16}$$

The limits of tanh are ± 1 so the minimum and maximum values of Eq. 5.16 are

$$\alpha_{\min} = \frac{1}{3}\left(1 + k - \sqrt{3(k^2 - k + 1)}\right) \tag{5.17a}$$

$$\alpha_{\max} = \frac{1}{3}\left(1 + k + \sqrt{3(k^2 - k + 1)}\right) \tag{5.17b}$$

$$\Delta\alpha \equiv \alpha_{\max} - \alpha_{\min} = \frac{2}{3}\sqrt{3(k^2 - k + 1)}. \tag{5.17c}$$

Figure 5.10 shows Eq. 5.17 on the relevant interval of $k \in [0, 1]$. Note that it can be easily shown that $\alpha_{min} = 0$, $\alpha_{max} = 1$, and $\Delta\alpha = 1$ only when $k = 1/2$; therefore for asymmetric values of k ($k \neq 1/2$) the steady state solution for α yields non physical results. This implies that an asymmetric fourth order free energy is unsuited for use with the NSCH equations. Higher order double well free energies may offer a to solution this issue, but is beyond the scope of this dissertation.
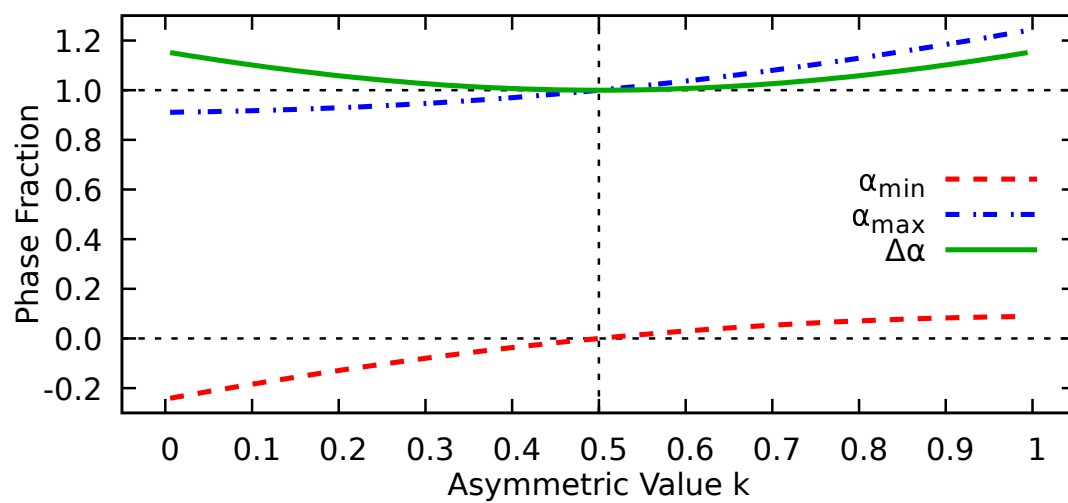
Fig. 5.10: Extremes of the phase fraction as a function of asymmetry.

6 Condensation onto Planar and Curved Interfaces

Chapters 3, 4, and 5 focused on constant temperature calculations of fluid-fluid interfacial properties. This chapter focuses on liquid-vapor interfaces under condensation using molecular dynamics. The outline of the remainder of this chapter is as follows: Sec. 6.1 describes the MD simulations, Sec. 6.2 discusses the Schrage's relationship for the mass flux, Sec. 6.3 discusses the calculation of the Onsager coefficients, and Sec. 6.4 discusses the effective heat transfer coefficient of the liquid-vapor interface during condensation. Finally discussions of the results are made in Sec. 6.5.

6.1 Molecular Dynamics Simulations

6.1.1 Domain Setup and Configuration

Condensation simulations in MD were performed on the dimensionless, truncated, and shifted Lennard-Jones potential with a cutoff radius of 3 and a time step of 0.005 with periodic boundary conditions. Figure 6.1 shows a schematic of the simulation domain for both the planar and curved liquid-vapor interfaces with domain sizes of $L \times H \times H$ and $L \times L \times L$ respectively. Regions Ω_V and Ω_L are control volumes where the temperature is thermostatted with velocity rescaling thermostats. Since the desired goal is to maintain condensation without depletion in the vapor region, the number of particles during the simulations must increase in order for the liquid region to condense. This was done by running GCMD in Ω_V in order to maintain a vapor chemical potential of μ_{res} in the control volume Ω_V. After the entire domain was equilibrated at $\rho_V(T_V)$, region Ω_L was subcooled by ΔT with $\Delta T = T_V - T_L$ where T_L is the temperature in Ω_L. A brief outline of the steps taken for the condensation
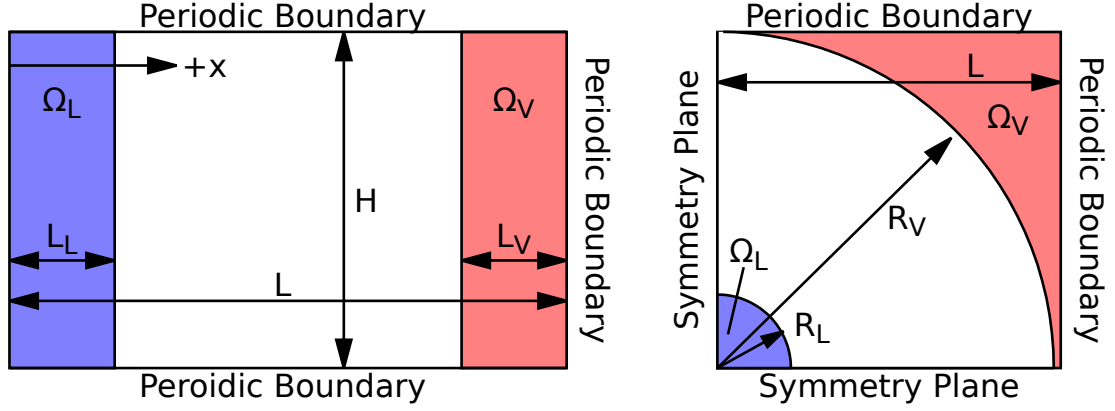
Fig. 6.1: Schematic for the condensation simulations of (left) planar liquid films and (right) spherical droplets. Blue regions indicate where cold thermostats were applied while red regions indicate where hot thermostats and GCMC where applied.

simulations are as follows:

(A) Thermostat global domain to T_V at $\rho_V(T_V)$

(B) Turn off global thermostat

(C) Locally thermostat Ω_V and Ω_L to T_V

(D) Begin GCMD to control μ_V in Ω_V

(E) Locally thermostat Ω_V to T_V and Ω_L to $T_L = T_V - \Delta T$.

Simulations were monitored to observe if liquid particles condensed in Ω_L. If a liquid region formed and was stable, the positions of the particles were centered such that the center-of-mass of the liquid region coincided with the geometric center of Ω_L. This was done to prevent smearing of data for the condensing droplets as the data was averaged in spherical bins centered about the origin.

6.1.2 Controlling the Chemical Potentials in Ω_V

In order to maintain the desired density, GCMD was applied in Ω_V. To determine the appropriate value for chemical potential of the vapor reservoir, μ_{res}, for Ω_V, separate GCMD simulations were performed in a cubic domain with periodic bound-

121
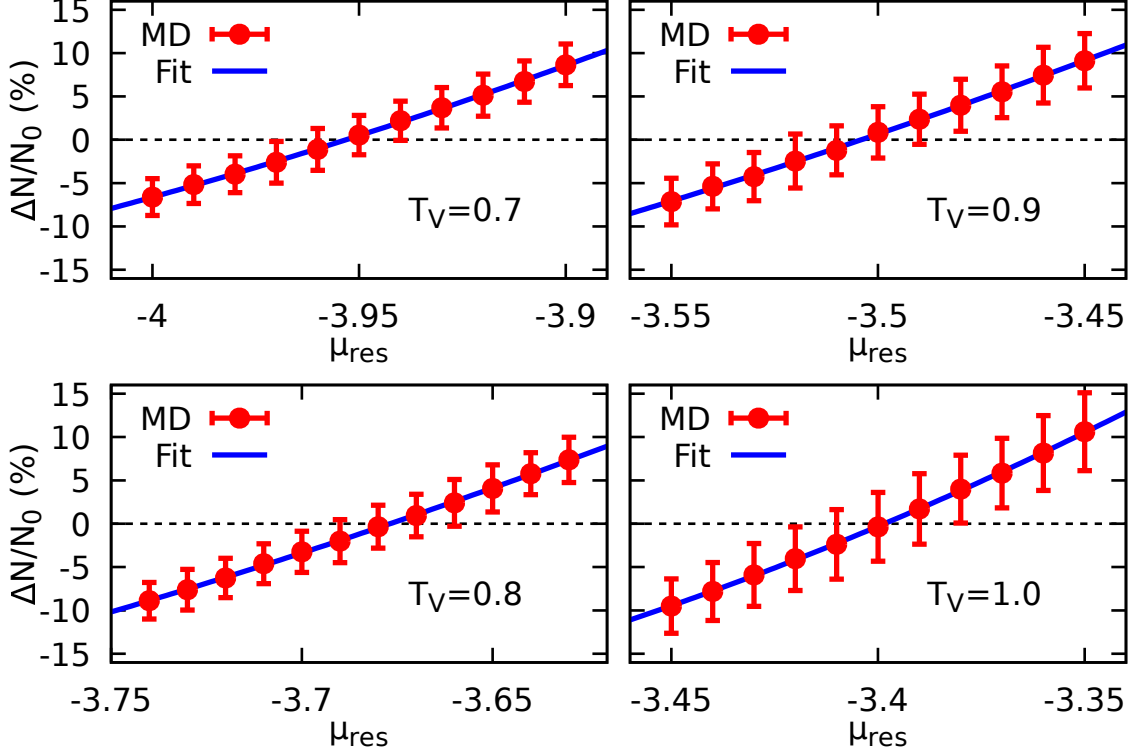
Fig. 6.2: Percent change in the number of atoms versus chemical potential for the GCMD simulations at various temperatures. Markers are MD data while solid lines are a quadratic fit to the data. Values for where the fitted quadratic crosses zero can be found in Table 6.1.

ary conditions with $N_0 = 2048$ particles. The lengths of the domains correspond to the densities in Table 6.1. GCMC was performed at various values of μ_{res}, and the number of molecules in the domain was monitored for 200000 time steps. Figure 6.2 shows the percent change in the number of particles, $\Delta N/N_0$, as a function of the chemical potential μ_{res}. Each value of μ_{res} was run with three separate initializations in order to obtain statistics for μ_{res}. A quadratic polynomial was then fit to the data in the least squares sense [169] in order to obtain the value of μ_{res} that would maintain the desired density of the domain at a set temperature. The values μ_{res} for which $\Delta N/N_0 = 0$ can be found in Table 6.1.

Table 6.1: Reservoir chemical potentials for vapor equilibrium at a given temperature and density.

T	ρ_V	μ_{res}	μ_{res} Error
0.7	0.0035	-3.953	0.006
0.8	0.0107	-3.677	0.004
0.9	0.0254	-3.504	0.011
1.0	0.0477	-3.399	0.003

6.1.3 Condensation and Interface Definition

Condensation simulations were run for at least 2 million time steps in order to see if condensation occurred. Table 6.2 lists whether condensation was observed for a given vapor temperature and liquid subcooling. No condensation was observed for any of the simulations with $T_V = 0.7$. At lower T_V the vapor density decreases, requiring larger density fluctuations in order to form a stable liquid droplet (film) in Ω_L. These larger fluctuations are less likely to occur resulting in no liquid region forming during the simulation runtime. A similar argument can be used for the lack of condensation seen at low subcooling.

The purpose of the GCMC steps in Ω_V is to replenish vapor particles that leave Ω_V and condense due to the temperature gradient. Figures 6.3 and 6.4 show the change in the number of particles in the simulation, ΔN, as a function of time for the planar and spherical systems respectively. Linear profiles were fit to ΔN (the solid lines in Figs. 6.3 and 6.4) all with excellent correlation with $R^2 > 0.99$ for all fits. The slopes of the linear profiles can be used to estimate the mass condensation rate $\dot{m}$ and are listed Table 6.3. As expected simulations with a larger subcooling ΔT have larger $\dot{m}$ as shown in Fig. 6.5. The mass flow for a given ΔT is the same within error for all T_V, which indicates that the subcooling, not the vapor temperature, is

Table 6.2: Table showing when condensation occurred.

	Planar Simulations							
ΔT	0.05	0.10	0.15	0.20	0.25	0.30	0.35	0.40
$T_V = 0.7$	No	No	–	–	–	–	–	–
$T_V = 0.8$	No	No	No	Yes	–	–	–	–
$T_V = 0.9$	No	No	Yes	Yes	Yes	Yes	–	–
$T_V = 1.0$	No	Yes	Yes	Yes	Yes	Yes	Yes	Yes
	Spherical Simulations							
ΔT	0.05	0.10	0.15	0.20	0.25	0.30	0.35	0.40
$T_V = 0.7$	No	No	–	–	–	–	–	–
$T_V = 0.8$	No	No	No	No	–	–	–	–
$T_V = 0.9$	No	No	Yes	Yes	Yes	Yes	–	–
$T_V = 1.0$	No	Yes	Yes	Yes	Yes	Yes	Yes	Yes
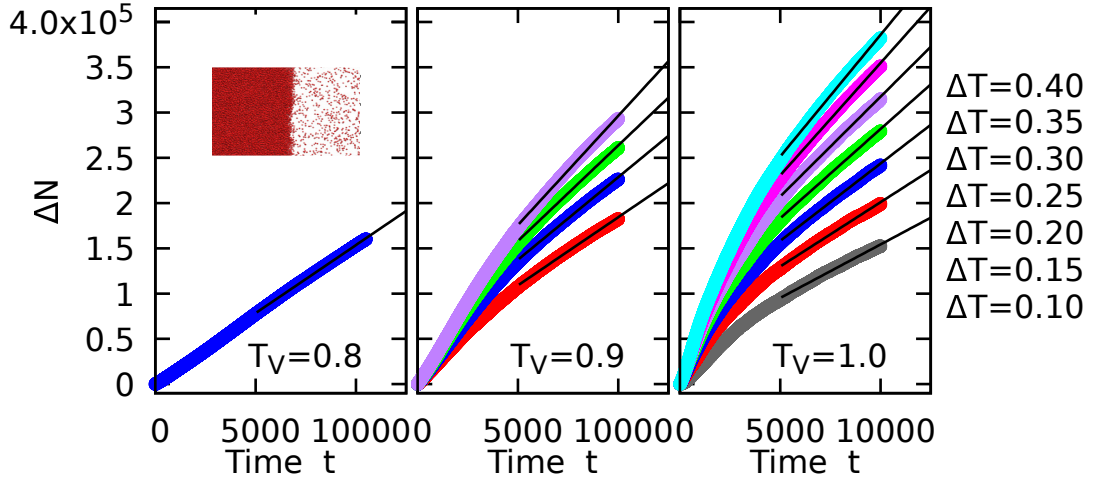
Fig. 6.3: Change in the number of particles in the planar simulations as a function of time for various vapor temperatures and liquid subcoolings. Solid lines are linear fits to the data after $t = 3750$ with $R^2 > 0.99$ for all cases.
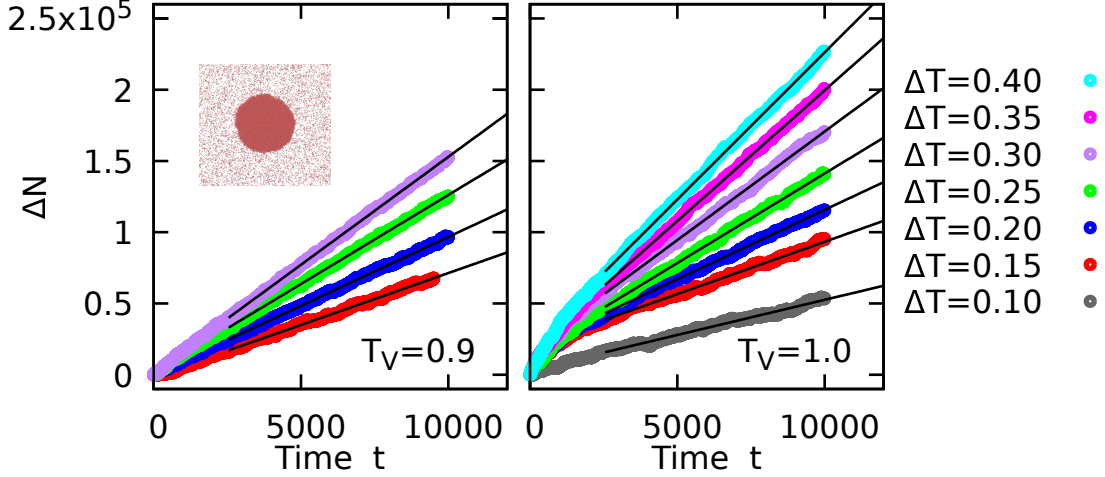
Fig. 6.4: Change in the number of particles in the droplet simulations as a function of time for various vapor temperatures and liquid subcoolings. Solid lines are linear fits to the data after $t = 2500$ with $R^2 > 0.99$ for all cases.

the dominate factor in determining the mass flow rate.

The GCMD steps of the simulations attempts particle insertions and deletions at a one to one ratio. Due to the net increase in ΔN the probability of accepting a trial insertion is greater than than accepting a trial deletion. However, the probability of accepting a trial deletion is $> 65\%$ and differs from the insertion probability by less than 2% for all simulations. This indicates that the vapor region Ω_V is maintaining an appropriate chemical potential and therefore density as desired. A significantly lower deletion probability would be a strong indicator that the vapor in Ω_V is not being appropriately replenished.

Figure 6.6 shows sample density and temperature profiles for the condensation simulations. The density was fit to the profile of the form [87]

$$\rho(r) = \frac{\rho_L(r) + \rho_V}{2} - \frac{\rho_L(r) + \rho_V}{2}\left(1 - \tanh\left(\frac{r - R}{\sqrt{2}L_{int}}\right)\right) \tag{6.1}$$

where R is the interface position, L_{int} is the interfacial thickness, ρ_V is the bulk vapor
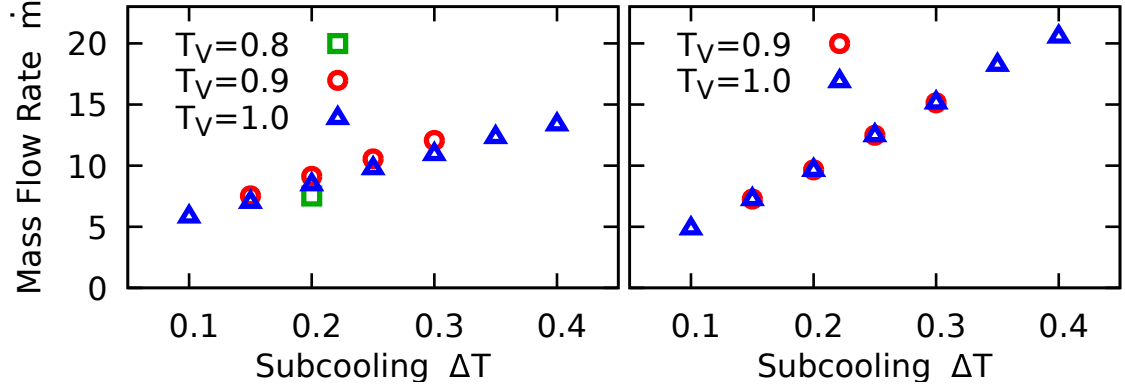
Fig. 6.5: Mass flow rate $\dot{m}$ versus temperature subcooling ΔT for the (left) planar and (right) spherical simulations. Error bars are similar to marker size.

Table 6.3: Mass flow rates.

T_V	ΔT	Planar $\dot{m}$	Spherical $\dot{m}$
0.8	0.20	7.512 ± 0.003	——
0.9	0.15	7.527 ± 0.007	7.266 ± 0.007
0.9	0.20	9.123 ± 0.008	9.656 ± 0.005
0.9	0.25	10.553 ± 0.010	12.478 ± 0.005
0.9	0.30	12.064 ± 0.011	15.136 ± 0.005
1.0	0.10	5.908 ± 0.007	4.933 ± 0.009
1.0	0.15	7.101 ± 0.008	7.331 ± 0.009
1.0	0.20	8.543 ± 0.008	9.722 ± 0.007
1.0	0.25	9.855 ± 0.009	12.553 ± 0.007
1.0	0.30	11.018 ± 0.012	15.236 ± 0.010
1.0	0.35	12.408 ± 0.013	18.315 ± 0.006
1.0	0.40	13.440 ± 0.015	20.629 ± 0.010
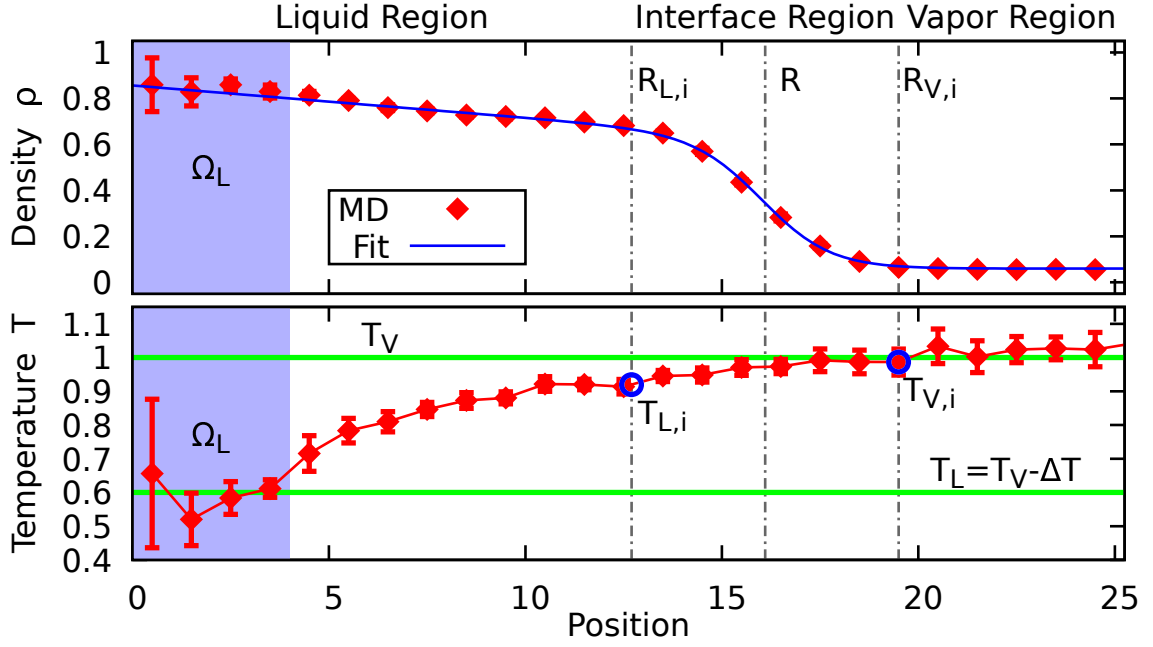
Fig. 6.6: Density (top) and temperature (bottom) profiles at $t = 600$ with $T_V = 1.0$ and $\Delta T = 0.4$ for the droplet simulation.

density, and $\rho_L(r) = ar + b$ is a linear fit of the liquid density with slope of a and intercept of b. The interfacial region is defined as the region between $R_{L,i}$ and $R_{V,i}$. Here $R_{L,i}$ is the location where $1 - \tanh((r_{L,i} - R)/\sqrt{2}L_{int}) = k$ with $k = 0.02$ and $R_{V,i}$ is the location where $k = 0.98$. Note that for the planar systems the notation x and X are used for the interfacial position instead of r and R. The temperature within the vapor region is approximately constant at T_V for all simulations and indicates that the energy flow through the vapor region is primarily due to mass flow. This is similar to the condensation simulations seen by Liang et $al.$ [4] and Kjelstrup et $al.$ [228]. However, there is a drastic temperature drop in the liquid region seen in Fig. 6.6, but in Ω_L the liquid temperature stabilizes to T_L indicating that thermostat in Ω_L is working as expected. The constant temperature in T_V along with the constant $\dot{m}$ indicates that the energy flowing through the system is roughly constant because $\dot{m}$ is constant.
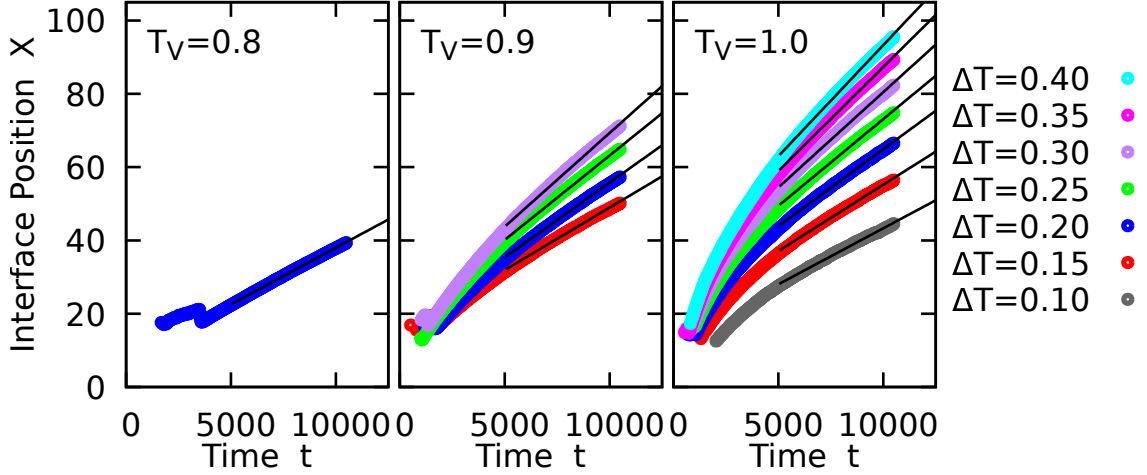
Fig. 6.7: Interface position as a function of time for various vapor temperatures and liquid subcoolings for the planar simulations. Solid linear are linear fits to the data all with $R^2 > 0.99$.

In the temperature profile in Fig. 6.6 there is not a temperature discontinuity throughout the interface as sometimes seen in colder interfaces and is in agreement with previous literature [77–79, 130, 131, 229]. This is due to the broadening of the interface, and the relative smoothness of the density profile across the interfacial region as opposed to the sharper interfaces at colder temperatures. The broader interface contains a larger number of particles, allowing for the latent heat of a vapor particle to be absorbed by a larger number of interfacial particles.

Figure 6.7 and Fig. 6.8 show the interface location as a function of time for the planar and droplet simulations respectively. Solid lines are fits for the data based upon solutions to $\dot{X} = a$ for planar systems and $\dot{R} = bR^{-2}$ for spherical systems where a and b are constant based upon the constant $\dot{m}$. The excellent fits for both the planar and spherical systems seen in Figs. 6.7 and 6.8 confirms the assumption that $\dot{m}$ is constant. Note that the sudden decrease in the interface positions for the planar simulations (around $t = 3500$ for $T_V = 0.8$ and $\Delta T = 0.20$) is the transition from a cylindrical liquid "drop" to a liquid film due to geometry of the domain.

128
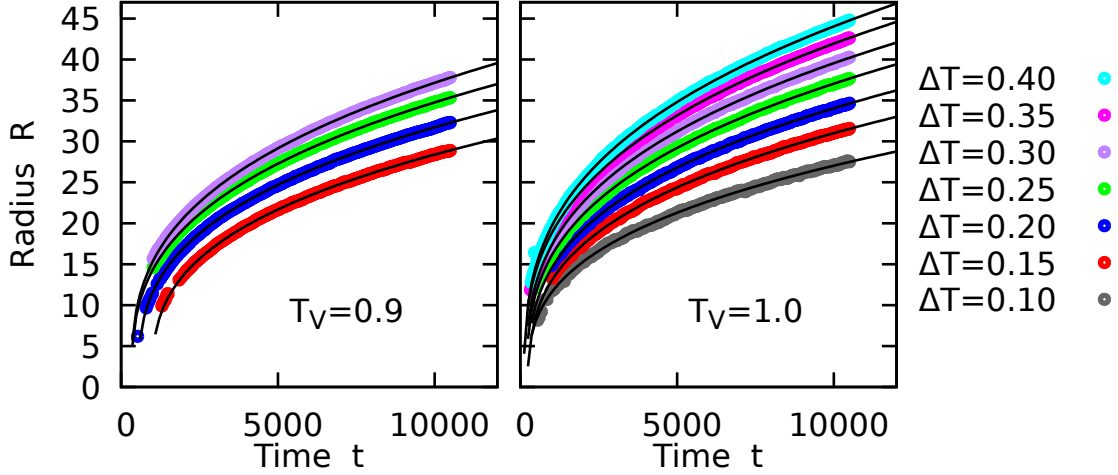
Fig. 6.8: Droplet radius as a function of time for various vapor temperatures and liquid subcoolings. Solid lines are fits to the data of the form $R(t) = \sqrt[3]{3k(t - t_0)}$ where k and t_0 are fitting parameters related to droplet growth rate and initial condensation time respectively.

6.2 Mass Flux: Schrage Relationship

The constant $\dot{m}$ and interfacial area A can be used to calculate the mass flux $\dot{m}''$ directly from the MD simulations. The mass flux for a planar interface was derived by Schrage [72] using kinetic theory and is often simplified to [4, 71, 73, 164]

$$\dot{m}''_S = \frac{2\alpha}{2 - \alpha} \sqrt{\frac{k_B}{2\pi m}} \left(\rho_V(T_{V,i}) \sqrt{T_{V,i}} - \rho_V(T_{L,i}) \sqrt{T_{L,i}} \right) \tag{6.2}$$

where α is the mass accommodation coefficient and $\rho_V(T_{V,i})$ and $\rho_V(T_{L,i})$ are the vapor densities evaluated at the vapor and liquid temperatures respectively. Marek [73] modified Schrage's result accounting for spherical geometry resulting in

$$\dot{m}''_S = \frac{4\alpha}{4 - 3\alpha} \sqrt{\frac{k_B}{2\pi m}} \left(\rho_V(T_{V,i}) \sqrt{T_{V,i}} - \rho_V(T_{L,i}) \sqrt{T_{L,i}} \right). \tag{6.3}$$

Equation 6.2 and Eq. 6.3 assume that condensation is occurring slowly, $v_0 v_{th}^{-1} \ll 1$ where $v_0 = \rho_V^{-1} \dot{m}''$ is the condensation velocity and $v_{th} = \sqrt{2k_B T/\pi m}$ is the thermal

129

Fig. 6.9: Mass flux $\dot{m}''$ as a function of (left) planar interface position X or (middle/right) droplet radius R for $T_V = 1.0$ and $\Delta T = 0.4$. Solid lines are the direct MD calculated mass flux $\dot{m}'' = \dot{m}A^{-1}$, while markers are Schrage's result, Eq. 6.2 or Eq. 6.3, calculated from the MD data. The (middle) figure does not account for the curvature dependence of α (Eq. 3.21) while the right does.

velocity. The minimum droplet radii analyzed during condensation is $R_{min} \sim 10$ therefore the maximum approach velocity is $v_0^{max} \sim 0.47$. The thermal velocity $v_{th} \sim 0.7 - 0.8$ therefore Eqs. 6.2 and 6.3 are expected to be valid for the majority of the droplet and film growth.

Figure 6.9 shows $\dot{m}''$ for a planar interface (left) and a curved interface (middle/right) with $T_V = 1.0$ and $\Delta T = 0.4$. The middle panel does not account for the curvature dependence of α (Eq. 3.21) while the right panel does. The curvature correction for small R decreases the difference between the MD calculated mass flux and Eq. 6.3. The mean square error χ is defined as

$$\chi = \left\langle \left(1 - \frac{\dot{m}''_S}{\dot{m}/A} \right)^2 \right\rangle \tag{6.4}$$

and decreases by over 40% by appropriately correcting for the curvature dependence of α, making χ similar to the value of the planar case.
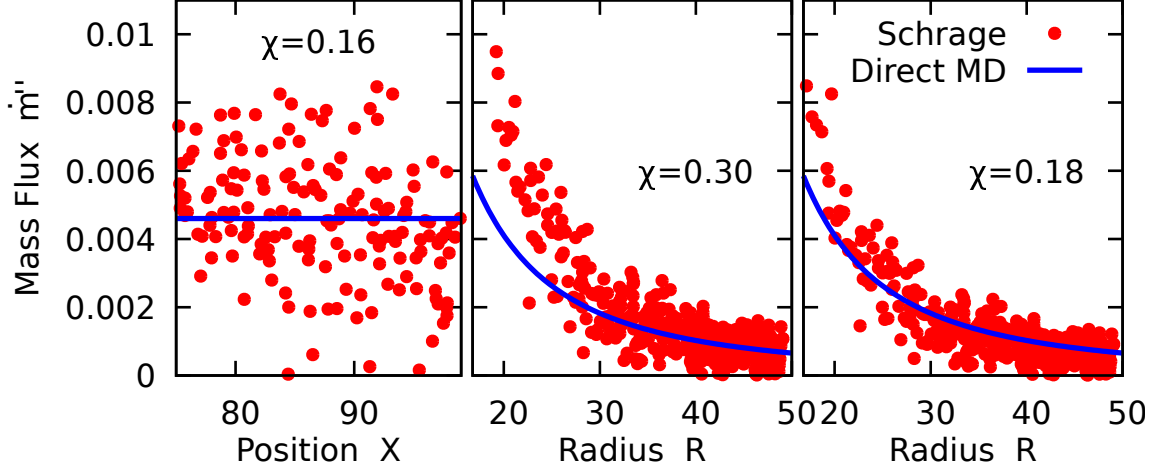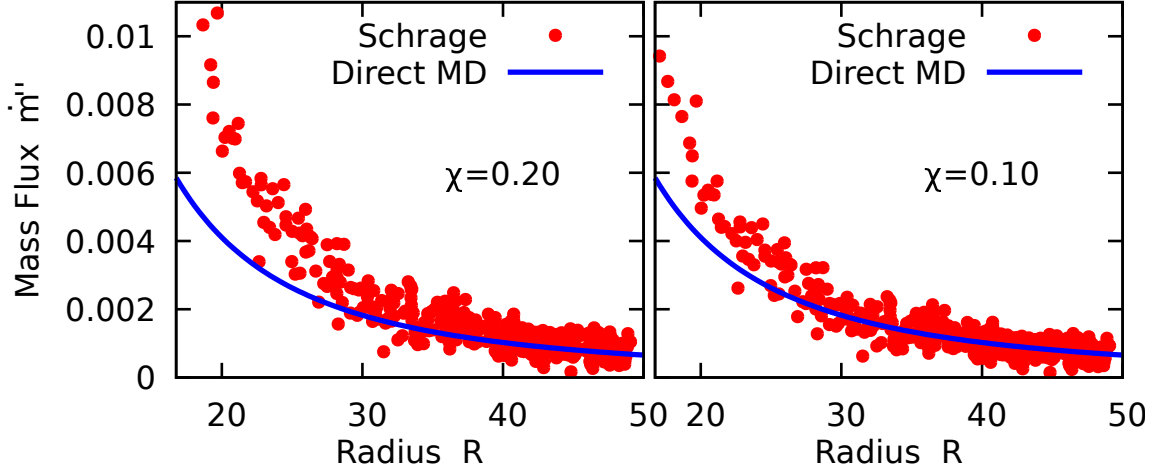
Fig. 6.10: Mass flux $\dot{m}''$ as a function of (left) planar interface position X or (middle/right) droplet radius R for $T_V = 1.0$ and $\Delta T = 0.4$. Solid lines are $\dot{m}'' = \dot{m}A^{-1}$ while markers are Eq. 6.5 calculated from the MD data. The (middle) figure does not account for the curvature dependence of α (Eq. 3.21) while the right does.

For the smallest droplets the assumption that $v_0 v_{th}^{-1} \ll 1$ may not be valid. The more generic form of Schrage's mass flux incorporating the approach velocity v_0 is [4]

$$\dot{m}''_{S,Full} = \alpha \sqrt{\frac{k_B}{2\pi m}} \left(\Gamma(-v_0 v_{th}^{-1}) \rho_V(T_{V,i})\sqrt{T_{V,i}} - \rho_V(T_{L,i})\sqrt{T_{L,i}} \right) \qquad (6.5)$$

where $\Gamma(a)$ is

$$\Gamma(a) = \exp(-a^2) - a\sqrt{\pi}(1 - \text{erf}(a)), \qquad (6.6)$$

and erf is the error function. Figure 6.10 shows $\dot{m}''_{Full}$ for a curved interface with $T_V = 1.0$ and $\Delta T = 0.4$. The left panel does not account for the curvature dependence of α (Eq. 3.21) while the right panel does. Similar to the previous result, applying the curvature dependence for α decreases the χ by roughly 50%, and overall Eq. 6.5 has a lower χ value compared to Eq. 6.2 as expected as it makes fewer assumptions. Applying Eq. 6.5 would have less of an effect on the planar interface because $v_0 v_{th}^{-1}$ does not change during the simulations because $\dot{m}$ and A are constants.

131

Deviations from Eq. 6.5 for the smallest radii can been seen in Fig. 6.10. The prominence of interfacial fluctuations at small radii offer a potential explanation for this deviation. A key assumption in the derivation of Eq. 6.5 is that the interface is infinitely thin with no surface fluctuations. When the droplet is small, the interface fluctuations are comparable to the droplet radii and have a dominate impact on the liquid-vapor interactions. These regions of positive and negative curvature impact condensation pathways of vapor particles as seen by Varilly and Chandler [230]. As the droplet increases in size, these fluctuation become less dominate and droplet becomes more "smooth" and spherical implying that the assumption made by Schrage is valid.

6.3 Onsager Coefficients During Condensation

In order to calculate the coupled interfacial heat and mass transfer effects, the local entropy generation σ^s (Eq. 2.42) can be simplified to

$$\sigma^s = \boldsymbol{q} \cdot \nabla \left(\frac{1}{T} \right) \tag{6.7}$$

recalling that $\boldsymbol{q}$ is the conductive heat flux. Integrating Eq. 6.7 (perpendicular to the interface so the vector notation can be dropped) results in the total interfacial entropy generation σ^S as [77, 78, 229, 231–235]

$$\sigma^S = \int q \frac{d}{dx} \left(\frac{1}{T} \right) dx = \int J \frac{d}{dx} \left(\frac{1}{T} \right) dx - \int \dot{m}'' h \frac{d}{dx} \left(\frac{1}{T} \right) dx \tag{6.8}$$

where q is the conductive heat flux, $\dot{m}'' h$ is the convective heat flux, and J is the total heat flux due to both conduction and convection through the interface which is assumed to be constant. Here $h = u + P/\rho$ is the local enthalpy, u is the local
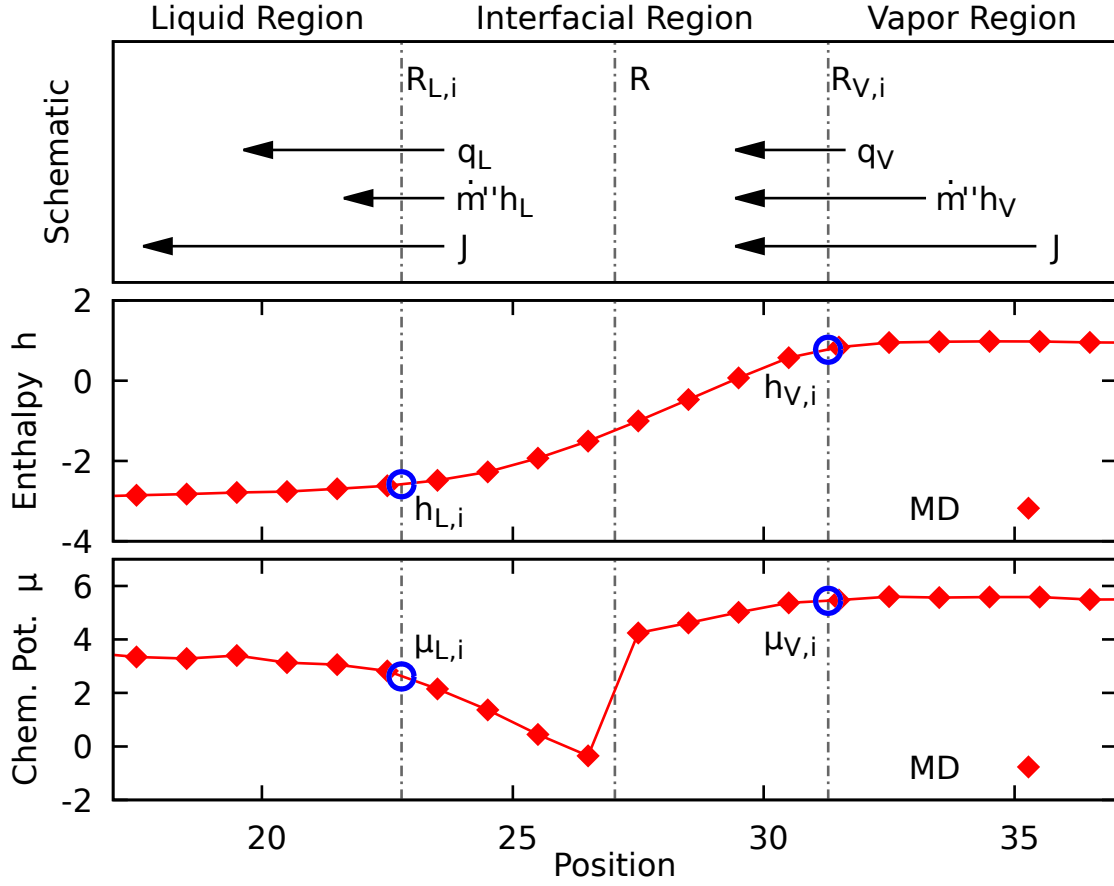
Fig. 6.11: (top) Energy flow schematic. (middle) Enthalpy and (bottom) chemical potential at $t = 2750$ with $T_V = 1.0$ and $\Delta T = 0.35$ for the droplet simulation.

internal energy, and P is the pressure. The constant total heat flux assumption [77, 78, 229, 231–235] implies that $J = q_L + \dot{m}''h_L = q_V + \dot{m}''h_V$ where the subscripts L and V indicate the heat flowing through the liquid and vapor "edges" of the interface, $R_{L,i}$ and $R_{V,i}$ respectively (dashed vertical gray lines in Fig. 6.6 and Fig. 6.11). Figure 6.11(top) shows a schematic of the energy flowing through the interface. Here the local internal energy is assumed to be the average per particle potential energy within a region, $u = \langle \mathcal{V}_j \rangle$ where $\mathcal{V}_j$ is the pairwise potential energy of particle j.

Figure 6.12 shows the energy (heat) added and removed by the thermostats in Ω_V and Ω_L respectively for $T_V = 1.0$ and $\Delta T = 0.40$. The agreement between $\dot{m}''h_V t$
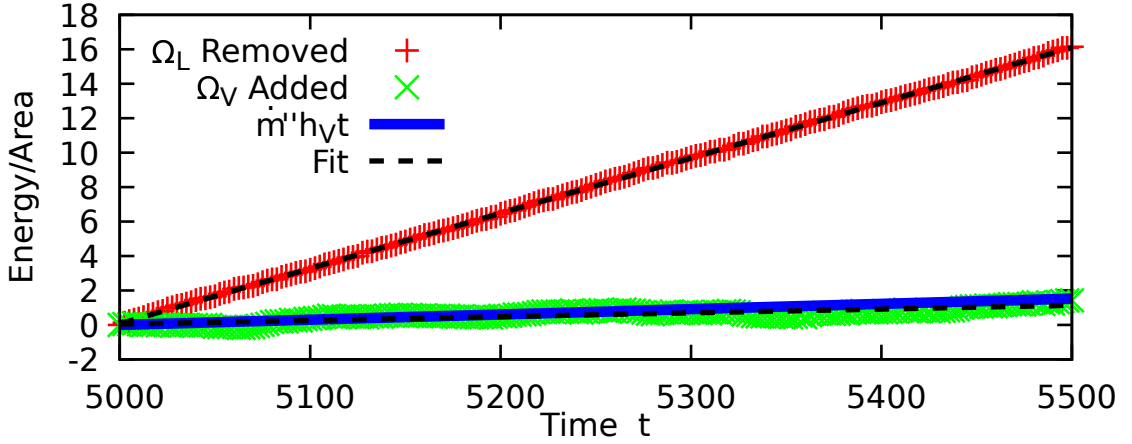
Fig. 6.12: Cumulative energy per area added or removed by the thermostats in Ω_L and Ω_V for the planar interfaces with $T_V = 1.0$ and $\Delta T = 0.40$. Dashed lines are linear fits of the data with $R^2 > 0.97$. The solid blue line is $\dot{m}'' h_V t$. The slope for the Ω_L fit is 0.032, while the slope for the Ω_V fit is 0.002.

and the energy added in Ω_V indicates that $q_V \approx 0$. This is in agreement with the constant temperature in the vapor region as seen in Fig. 6.6 and is consistent with the assumptions of Kjelstrup *et al.* [228]. The difference between the added and removed energy combined with $\dot{m}''$ is a measure of the latent energy being absorbed in the domain due to condensation. With $q_V \approx 0$ and a the latent heat $h_V - h_L$, q_L can be approximated as $q_L \approx (h_V - h_l)/\dot{m}''$.

Evaluating the integral in Eq. 6.8 at the "edges" of the interface using the thermodynamic identity (details found in Sec. 6.6)

$$\frac{d}{dx}\left(\frac{\mu}{T}\right) = h\frac{d}{dx}\left(\frac{1}{T}\right) \tag{6.9}$$

where μ is the chemical potential, results in

$$\sigma^S = J\left(\frac{1}{T_{V,i}} - \frac{1}{T_{L,i}}\right) - \dot{m}''\left(\frac{\mu_{V,i}}{T_{V,i}} - \frac{\mu_{L,i}}{T_{L,i}}\right). \tag{6.10}$$

134

Here subscripts V, i and L, i indicate properties taken at the vapor and liquid edges of the interface respectively, $R_{L,i}$ and $R_{V,i}$ respectively (dashed vertical gray lines in Fig. 6.6 and Fig. 6.11). Substituting back in for the conductive heat flux q_L results in

$$\sigma^S = q_L \left(\frac{1}{T_{V,i}} - \frac{1}{T_{L,i}} \right) - \dot{m}'' \left(\frac{\mu_{V,i} - h_{V,i}}{T_{V,i}} - \frac{\mu_{L,i} - h_{L,i}}{T_{L,i}} \right). \tag{6.11}$$

Figure shows 6.11 the local profiles for h and μ where Widom sampling, Eq. 2.61, was used to calculate the excess portion of μ. The discontinuity in the interfacial region for μ is due to the limited number of data points in the region. The chemical potential throughout the interfacial region is not expected to be monotonic, similar to the normal and transverse pressure profiles across an interface [236–239].

The Onsager relations (Eq. 2.43) based upon the results of Eq. 6.11 are

$$q_L = L^{qq} F_T - L^{qm} F_M \tag{6.12a}$$

$$\dot{m}'' = L^{qm} F_T - L^{mm} F_M \tag{6.12b}$$

where $F_T = (1/T_{V,i}) - (1/T_{L,i})$ and $F_M = (\mu_{V,i} - h_{V,i})/T_{V,i} - (\mu_{L,i} - h_{L,i})/T_{L,i}$ are the thermal and mass driving forces, and L^{qq}, L^{mm}, and L^{qm} are the Onsager coefficients for heat flow, mass flow, and coupled heat-mass flow. Figures 6.13 and 6.14 show the driving forces as a function of droplet size with F_M being roughly an order of magnitude greater than F_T. From Fig. 6.13, there is a decrease in the magnitude F_T at increased R, which can be contributed to the decreased energetic flux due to increasing surface area of the droplet. The similar magnitudes of F_M between the planar and spherical systems in Fig. 6.14 indicate that curvature does not play a key role in the the mass driving force. A slight trend can be seen in Figs.6.13 and 6.14 where the increased subcooling increases the driving forces F_T and F_M for a given
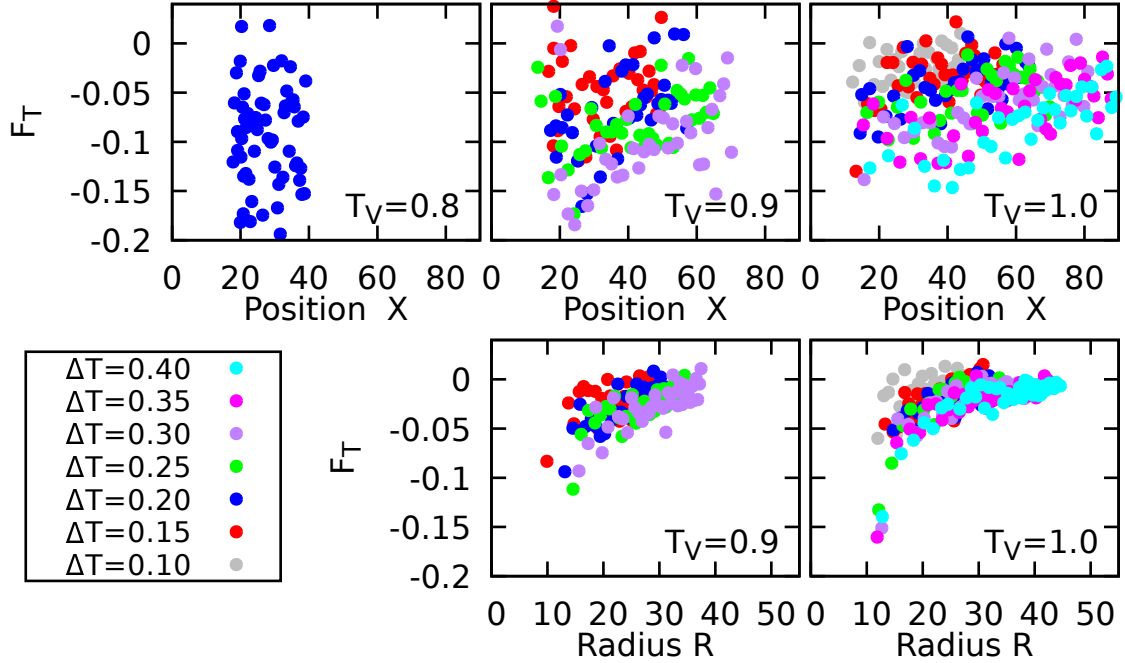
Fig. 6.13: Thermal driving force $F_T = (1/T_{V,i}) - (1/T_{L,i})$ as a function of (top) planar interface position and (bottom) droplet radius simulations for various vapor temperatures.

vapor temperature. The noise in the data (especially for F_T) for both the planar and spherical cases is due to the limited averaging because of the moving interfaces. This makes it difficult to draw any robust conclusions about either of the driving forces as a function of T_V, ΔT, or R.

Bedeaux and Kjelstrup [235] and Kuhn *et al.* [240] relate the Onsager mass flow coefficient to the diffusion coefficient D with $L^{mm} \sim D$. Recalling the results from Chap. 4, D is proportional to the interfacial mobility M mobility, therefore

$$L^{mm} \sim \rho^2 T M \sim \frac{\rho^2 T \gamma}{L_{int}} \tag{6.13}$$

noting that Bedeaux and Kjelstrup [235] absorbed the temperature into the Onsager coefficient and recalling that γ is the mobility from the Navier-Stokes-Cahn Hilliard
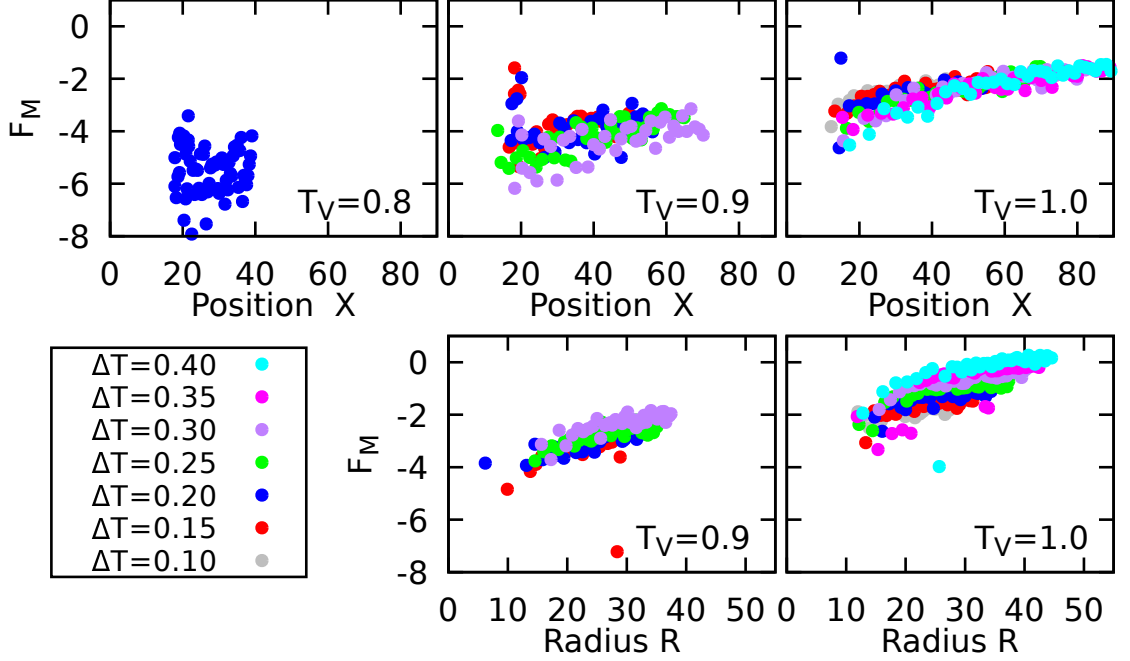
Fig. 6.14: Mass driving force $F_M = (\mu_{V,i} - h_{V,i})/T_{V,i} - (\mu_{L,i} - h_{L,i})/T_{L,i}$ as a function of of (top) planar interface position and (bottom) droplet radius simulations for various vapor temperatures.

model (Eqs. 5.1). Assuming that the proportionality constant is unity, L^{mm} is shown in Fig. 6.15. The mass Onsager coefficient increases with temperature similar to the mobility and interfacial length.

The remaining Onsager coefficients L^{qq} and L^{qm} can now be calculated in MD because q and $\dot{m}''$ are known. Figure 6.16 compares the ratio of the mass and thermal driving terms in Eq. 6.12, $(L_{qm}F_M)/(L_{qq}F_T)$, as a function of interface position or droplet size. The ratio being of $\mathcal{O}(1)$ indicates that the thermal and mass forces are consistent with one another. This is supported by the small value of q_L as compared to $(L_{qm}F_M)$. The slope in Fig. 6.12 can be used to estimate q_L with $q_L \approx 0.024$. For the corresponding case, the average of the mass driving term is $L^{qm}F_M = 1.28 \pm 0.17$. The numerical values given are typical for both the spherical and planar interfaces with the value for q_L being small relative to the mass driving force. This indicates that
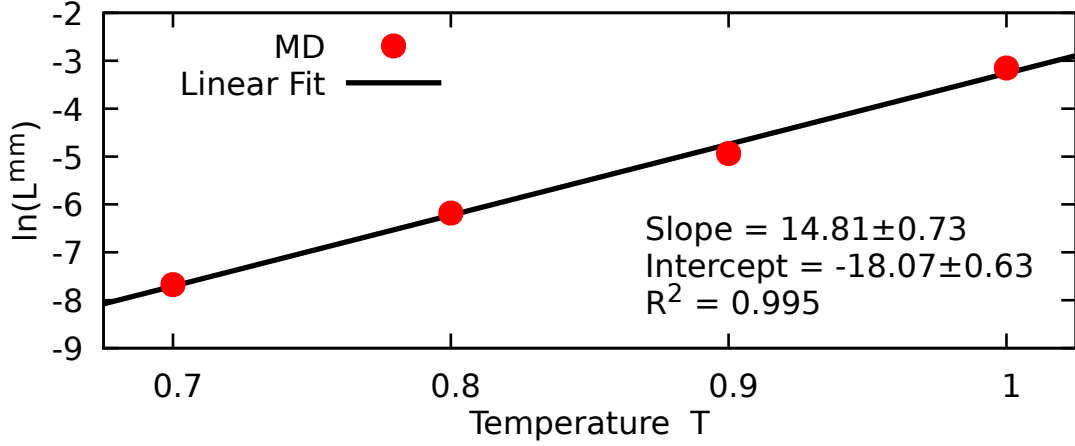
Fig. 6.15: Natural logarithm of the Onsager coefficient L^{mm} as a function of temperature. Values are in dimensionless units.

there is a minimal coupling between the heat and mass fluxes because $q_L \ll L^{qm} F_M$. Due to the relatively slow condensation process and small values of $\dot{m}''$ and q_L, the ratio of the driving forces and coefficients is fairly insensitive to the precise value used for the proportionality in Eq. 6.13.

6.4 Effective Heat Transfer Coefficient

Section 6.3 shows the majority of energy transfered through the interface is through accessing the latent heat required to change from the vapor to the liquid phase, therefore the effective interfacial heat transfer coefficient h_{eff} is

$$h_{eff} = \frac{q_L - q_V}{T_{V,i} - T_{L,i}} \approx \frac{\dot{m}''(h_{V,i} - h_{L,i})}{T_{V,i} - T_{L,i}}. \tag{6.14}$$

This is the commonly used form for interfacial heat transfer and is verified in Sec. 6.3. Figure 6.17 shows h_{eff} as a function of subcooling ΔT for the planar (left) and spherical (right) simulations averaged over the last 2000 time units. The general

138
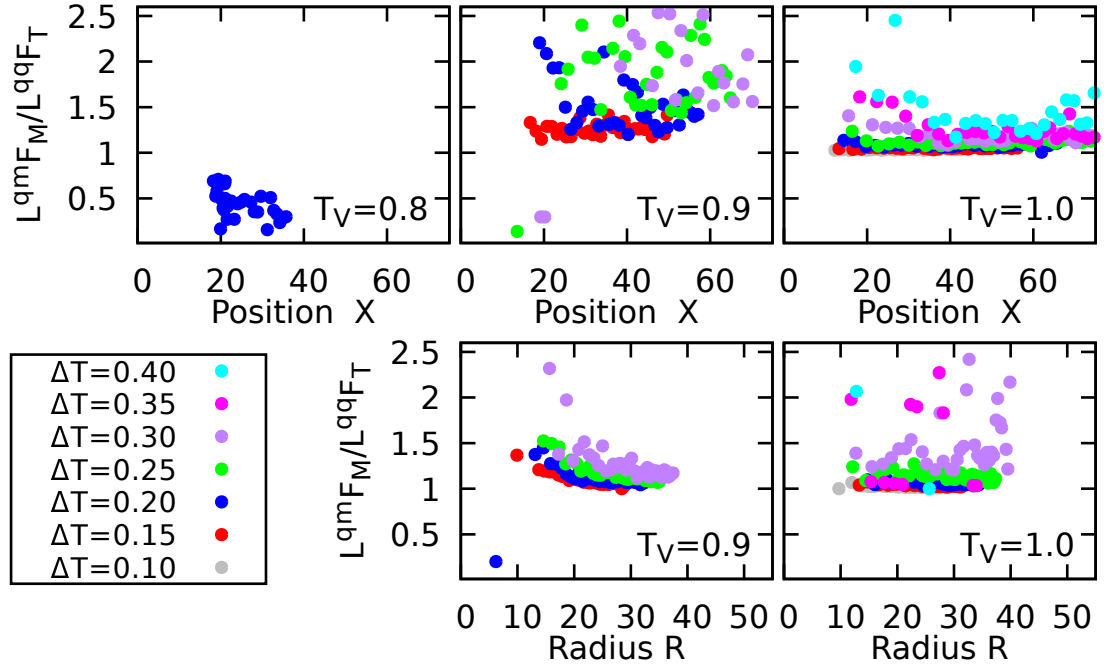
Fig. 6.16: Ratio of the Onsager coupled heat-mass coefficient term $L^{qm}F_M$ to the heat Onsager term $L^{qq}F_T$ as a function of time for (top) planar and (bottom) droplet simulations. Vapor temperatures T_V are shown in the figures, and all values are in dimensionless units.
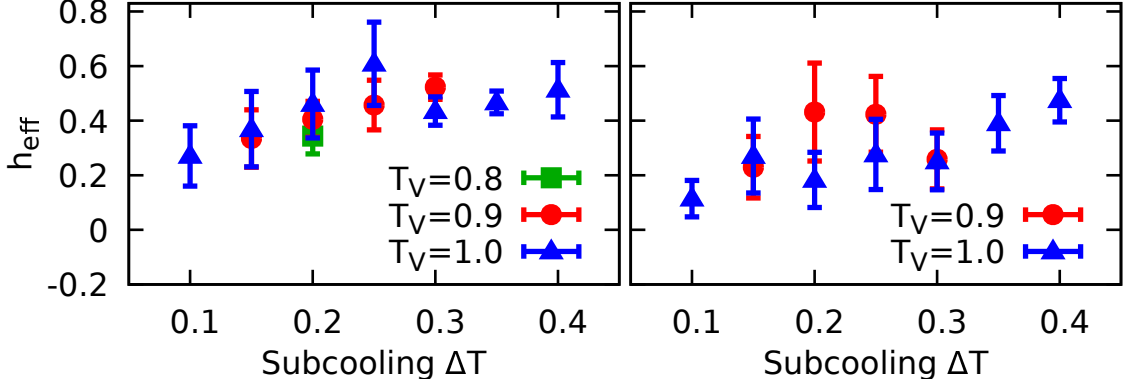
Fig. 6.17: Effective heat transfer coefficient versus h_{eff} versus subcooling for (left) planar simulations and (right) spherical simulations.

trend is that heat transfer improves with an increased temperature difference. This is primarily due to the increased mass flux $\dot{m}''$ as $\dot{m}''$ increases linearly with ΔT, Fig. 6.5. The values for h_{eff} are also similar to the result of Liang *et al.* [4] giving further confidence that the coupled heat-mass transport is negligible as assumed by Liang *et al.*

The vapor temperature T_V does not seem to have a significant impact on the results. Furthermore, it is difficult to draw any firm conclusions about the effect of T_V due to the large overlap between the error bars in the data seen in Fig. 6.17. The effect of T_V could be further explored by setting T_V to higher values than in this work. However, larger T_V would make T_V greater than the critical temperature of the fluid (Table 3.8) and care must be taken to ensure that $T_L = T_V - \Delta T$ is within the coexistence region, which would require larger ΔT than studied in this work.

6.5   Discussion and Conclusion

GCMD simulations were performed at various subcooling, and condensation occurred only if the subcooling was above a given value for a specific vapor temperature.

The mass flow increased with increased subcooling and showed minimal dependence on the vapor temperature. Schrage's mass flux relationship was examined and shown to be valid for droplets with radii larger than 30 in dimensionless units. The coupled heat and mass transfer was shown to be negligible for the subcoolings and vapor temperatures simulated in this chapter, confirming that the total energy (heat) flux through the interface is $J \approx \dot{m}''(h_V - h_L)$. The effective heat transfer coefficient was found to increase with subcooling similar to the mass flow rate.

The purpose of running GCMD is to replenish the vapor region in Ω_V in a thermodynamically consistent manner, allowing for condensation to occur in a quasi-steady manner. However, the GCMD portion of the simulation drastically increases the computational run time of the simulations as several ~ 100 GCMC trial moves are performed requiring energy computations between every MD time step, drastically increasing the computational cost compared with standard MD [99]. There exist alternative methods to replenish the vapor particles such as applying the USHER [241] or FADE [242] algorithms in Ω_V, similar to the particle insertion deletion method for enforcing fluid flow [99]. However, these methods lack the thermodynamic justification of GCMD, but could allow for a more thorough study of condensing systems in the presence of non-condensible gases (NCG) or with surface surfactants.

The presence of NCGs can play a crucial role in condensation [130,131] and could be an area of future exploration of droplet condensation simulations. The presence of NCG has been shown to decrease the mass flux under similar subcooling [130] causing a decrease in the effective heat transfer coefficient for planar simulations. The presence of NCG was also shown to cause a temperature decreases in the pure vapor region [131] while the temperature was roughly constant without the presence of NCG [4]. This would require larger temperature gradients in order for condensation to occur

causing Ω_V to contain vapor at temperature above the critical temperature similar [77–79, 229]. The larger temperature gradients may cause the linear approximations made in the Onsager relations to no longer be valid due to the larger driving forces.

6.6 Appendix: Thermodynamic Identity

In this chapter the assumption $h = \frac{\partial(\mu/T)}{\partial(1/T)}$ was used where h is the specific enthalpy, μ is the chemical potential, and T is the temperature. Letting $k = T^{-1}$ the equation simplifies to

$$h = \frac{\partial(\mu/T)}{\partial(1/T)} = \frac{\partial(k\mu)}{\partial k} = \mu + k\frac{\partial\mu}{\partial k} = \mu + \frac{1}{T}\frac{\partial\mu}{\partial T}\frac{\partial T}{\partial k} = \mu - T\frac{\partial\mu}{\partial T}. \tag{6.15}$$

Therefore if the above can be shown then the assumption is valid. The Euler equation solved for the specific entropy s is

$$s = \frac{h - \mu}{T} \tag{6.16}$$

and the Gibbs-Duhem relationship solving for s results in

$$s = \frac{\nu dp - d\mu}{dT}. \tag{6.17}$$

Combing Eqs. 6.16 and 6.17 and solving for h yields

$$h = \nu T\frac{dp}{dT} + \mu - T\frac{d\mu}{dT}. \tag{6.18}$$

If $p = const$ and letting the partial derivative ∂ be a spatial derivative d/dx then Eq. 6.18 reduces to Eq. 6.15 as desired,

$$h\frac{d}{dx}\left(\frac{1}{T}\right) = \frac{d}{dx}\left(\frac{\mu}{T}\right).$$

(6.19)

7 Conclusions

7.1 Summary

Fluid-fluid interfaces under equilibrium and non-equilibrium conditions were investigated using molecular and continuum models. Several continuum properties including the mass accommodation coefficient and interfacial mobility were computed using molecular dynamics allowing for the physical parameters to be used as an *a priori* input to continuum scale models such as the Navier-Stokes-Cahn-Hilliard equations or interfacial resistances in condensation models.

Equilibrium molecular dynamics simulations were performed to calculate the mass accommodation coefficient for liquid-vapor interfaces (liquid films and droplets) for a variety of simple fluids as well as for the realistic fluids of benzene, butane, methane, methanol, and water. A new method to tag accommodated particles was developed and validated against the literature for planar interfaces. This method was then applied to calculated the mass accommodation coefficient for highly curved droplets. A curvature dependence was seen for all fluids simulated, and the mass accommodation coefficient decreased as the size of the liquid droplet decreased. A universal trend was seen if the mass accommodation coefficient is scaled by its planar value and if the droplet radius is scaled by an appropriate normalizing radius. For the fluids simulated, the curvature dependence was prevalent for droplets with radii less than ~ 55 nm. Incorporating this effect into continuum models may allow for a more accurate representation of dropwise condensation on small length scales.

The fluid-fluid interfacial mobility for two liquid-liquid and one liquid-vapor interface was computed using equilibrium molecular dynamics. The mobility was cal-

144

culated from interfacial fluctuation using three methods: using the interfacial mean square displacement, using a Green-Kubo integration of the interfacial velocity auto-correlation function, and using the variance of the average interfacial position. The three methods agreed well with one another for the three fluid-fluid interfaces indicating that any of the methods could be used to compute the interfacial mobility.

The diffuse mobility in the Navier-Stokes-Cahn-Hilliard model was computed from a combination of molecular dynamics and the computational fluid dynamics using Navier-Stokes-Cahn-Hilliard equations for the Lennard-Jones interface at several temperatures. The diffuse mobility is an inherently dynamic property, therefore interfacial relaxation simulations were performed. Bulk parameters such as viscosity, density, and surface tension, were first computed in molecular dynamics and used as inputs for the continuum model. Comparison between the two methods allowed for an effective diffuse mobility to found for the continuum model. This extracted diffuse mobility was compared with the fluctuation mobility for the liquid-vapor interface. The two mobilities differed by a unit of length, and the interfacial width was used to bridge difference between the two mobilities. The two values for the mobilities agreed well with one another indicating the the fluctuation mobility and diffuse mobility are measuring a similar interfacial property.

Finally, condensation simulations were performed using molecular dynamics to calculate interfacial properties for both condensing liquid films and droplets. The liquid was subcooled to values ranging from 6.0 K to 48.4 K (0.05 to 0.4 dimensionless units). Schrage's relationship for the mass flux was shown to be valid if the curvature dependence of the mass accommodation coefficient is taken into account for droplets with radii larger than 10 nm (30 in dimensionless units). The interfacial heat transfer coefficient increased with increased subcooling due to the increased mass flux and la-

tent heat. Additionally the interfacial Onsager coefficients were calculated, including the heat and mass cross term for the condensing systems. The coupled-heat mass term was found to negligible for the systems studied in this work, but could be of importance for systems with higher driving forces or in the presence of non-condensible gases or on surfaces with heterogeneous condensation.

7.2   Engineering Perspective

This work examines the of physical properties for fluid-fluid interfaces with a focus on liquid-vapor interfaces in the absence of non-condensible gases. Interfacial motion and condensation have a direct impact in engineering applications such as water harvesting [111–113], desalination [19, 25], power generation [28–30, 112, 243–245], thermal management [23, 24], and environmental control [26, 27, 246]. Homogeneous nucleation of liquid droplets directly impact several of these applications through the flashing phenomenon which impacts nuclear power plant safety and can cause mechanical damage to refrigeration systems and emergency values [243, 244, 247]. Homogeneous nucleation is a difficult problem that is summarized well by a quote from the review article by Wyslouzil and Wölk [248], "The fact that after $\sim$ 120 yr of effort we still cannot confidently predict the nucleation rates associated with this phase transition, emphasizes that even homogeneous vapor phase nucleation is not an easy problem." The curvature dependence of the mass accommodation coefficients makes strides toward understanding the challenges of fully homogeneous nucleation as it is directly relevant toward the stability and growth of small liquid droplets.

Particle-cloud interactions are currently a significant open question in climate modeling and are driven by the condensation of atmospheric water vapor onto cloud condensation nuclei [101–104, 249]. This has lead to the investigation of alterna-

tive cooling and refrigerant options such as ammonia, carbon dioxide, nitrogen, and hydrocarbons as their ozone depletion and global warming potential are minimal [245, 250–254]. These coolants are expected to be used in future power plants cooling systems [245], especially hydrocarbons due to their reduced costs and interactions with common lubricants [250–252]. Being able to accurately characterize these fluids and having a robust understanding of the interfacial motion and condensation is important for improving the efficiency and reducing the emissions of these systems [255], and this dissertation provides a framework for calculating the physical properties of these interfaces.

7.3 Future Directions

Future directions for this work could be to further explore the curvature dependence of the mass accommodation coefficient to see if the dependence is present in more complex fluid systems such as binary fluid mixtures, interfaces in the presence of non-condensible gases. Furthermore, the connection between the fluctuation and diffuse mobilities could be further established my comparing the mobilities at several temperatures and for additional fluid-fluid interfaces. For the condensation simulations, larger temperature gradients could be applied by increasing the vapor temperature in order examine the effects of larger gradients on the Onsager coefficients, specifically the coupled heat-mass coefficient. Incorporating the mass accommodation coefficient into continuum models would allow for a more accurate representation of small scale phenomena on a computationally accessible manner for condensing systems. This combined with an *a priori* mobility may open the door to further improve and optimize condensing systems because the continuum models will be built on a more robust foundation. These improved systems have the potential to have a positive

147

impact on variety of applications ranging from microelectronics to power generation.

References

[1] Tatsuya Ishiyama, Takeru Yano, and Shigeo Fujikawa. Molecular dynamics study of kinetic boundary condition at an interface between argon vapor and its condensed phase. *Physics of Fluids*, 16(8):2899–2906, 2004.

[2] Shengfeng Cheng, Jeremy B Lechman, Steven J Plimpton, and Gary S Grest. Evaporation of lennard-jones fluids. *The Journal of Chemical Physics*, 134(22):224704, 2011.

[3] Gyoko Nagayama and Takaharu Tsuruta. A general expression for the condensation coefficient based on transition state theory and molecular dynamics simulation. *The Journal of Chemical Physics*, 118(3):1392–1399, 2003.

[4] Zhi Liang, Thierry Biben, and Pawel Keblinski. Molecular simulation of steady-state evaporation and condensation: Validity of the schrage relationships. *International Journal of Heat and Mass Transfer*, 114:105–114, 2017.

[5] A. A. Rostami, A. S. Mujumdar, and N. Saniei. Flow and heat transfer for gas flowing in microchannels: A review. *Heat and Mass Transfer*, 38(4-5):359–367, 2002.

[6] Chiara Neto, Drew R. Evans, Elmar Bonaccurso, Hans-Jürgen Butt, and Vincent S. J. Craig. Boundary slip in newtonian liquids: A review of experimental studies. *Reports on Progress in Physics*, 68(12):2859, 2005.

[7] Yuxiu Li, Jinliang Xu, and Dongqing Li. Molecular dynamics simulation of nanoscale liquid flows. *Microfluidics and Nanofluidics*, 9(6):1011–1031, 2010.

[8] M. Whitby and N. Quirke. Fluid flow in carbon nanotubes and nanopipes. *Nature Nanotechnology*, 2(2):87–94, 2007.

[9] George M. Whitesides. The origins and the future of microfluidics. *Nature*, 442(7101):368–373, 2006.

[10] Arash Aghigh, Vahid Alizadeh, H. Y. Wong, Md. Shabiul Islam, Nowshad Amin, and Mukter Zaman. Recent advances in utilization of graphene for filtration and desalination of water: A review. *Desalination*, 365:389–397, 2015.

[11] Seyed Ali Saadati and Ehsan Roohi. Detailed investigation of flow and thermal field in micro/nano nozzles using simplified bernoulli trial (sbt) collision scheme in dsmc. *Aerospace Science and Technology*, 46:236–255, 2015.

[12] Yingxia Qi, Xiangqi Meng, Defu Mu, Yangliu Sun, and Hua Zhang. Study on mechanism and factors affecting the gas leakage through clearance seal at nano-level by molecular dynamics method. *Energy*, 102:252–259, 2016.

[13] Bertrand Bourlon, Joyce Wong, Csilla Mikó, László Forró, and Marc Bockrath. A nanoscale probe for fluidic and ionic transport. *Nature Nanotechnology*, 2(2):104–107, 2007.

[14] Omid Ejtehadi, Ehsan Roohi, and Javad Abolfazli Esfahani. Investigation of basic molecular gas structural effects on hydrodynamics and thermal behaviors of rarefied shear driven micro/nano flow using dsmc. *International Communications in Heat and Mass Transfer*, 39(3):439–448, 2012.

[15] Ran Yoo, Jeongmin Kim, Min-Jung Song, Wooyoung Lee, and Jin Seo Noh. Nano-composite sensors composed of single-walled carbon nanotubes and polyaniline for the detection of a nerve agent simulant gas. *Sensors and Actuators B: Chemical*, 209:444–448, 2015.

[16] Qihua Wu, Jeong Tae Ok, Yongpeng Sun, S. T. Retterer, Keith B. Neeves, Xiaolong Yin, Baojun Bai, and Yinfa Ma. Optic imaging of single and two-phase

pressure-driven flows in nano-scale channels. *Lab on a Chip*, 13(6):1165–1171, 2013.

[17] Chaohua Guo, Jianchun Xu, Keliu Wu, Mingzhen Wei, and Songyuan Liu. Study on gas flow through nano pores of shale gas reservoirs. *Fuel*, 143:107–117, 2015.

[18] Lidong Geng, Gensheng Li, Pacelli Zitha, Shouceng Tian, Mao Sheng, and Xin Fan. A diffusion–viscous flow model for simulating shale gas transport in nano-pores. *Fuel*, 181:887–894, 2016.

[19] Akili D. Khawaji, Ibrahim K. Kutubkhanah, and Jong-Mihn Wie. Advances in seawater desalination technologies. *Desalination*, 221(1-3):47–69, 2008.

[20] M. Showers, T. M. Biewer, J. B. O. Caughman, D. C. Donovan, R. H. Goulding, and J. Rapp. Heat flux estimates of power balance on proto-mpex with ir imaging. *Review of Scientific Instruments*, 87(11):11D412, 2016.

[21] Mark Zerby. Thermal management for the next generation navy, March 2017.

[22] Yunus A. Çengel and Afshin J. Ghajar. *Heat and Mass Transfer Fundamentals and Applications*. New York: McGraw Hill, 4 edition, 2007.

[23] Baizhan Li and Runming Yao. Urbanisation and its impact on building energy consumption and efficiency in china. *Renewable Energy*, 34(9):1994–1998, 2009.

[24] B. Von Elsner, D. Briassoulis, D. Waaijenberg, A. Mistriotis, Chr. Von Zabeltitz, J. Gratraud, G. Russo, and R. Suay-Cortes. Review of structural and functional characteristics of greenhouses in european union countries: Part i, design requirements. *Journal of Agricultural Engineering Research*, 75(1):1–16, 2000.

[25] Lin Zhou, Yingling Tan, Jingyang Wang, Weichao Xu, Ye Yuan, Wenshan Cai, Shining Zhu, and Jia Zhu. 3d self-assembly of aluminium nanoparticles for plasmon-enhanced solar desalination. *Nature Photonics*, 10:393–398, 2016.

[26] Luis Pérez-Lombard, José Ortiz, and Christine Pout. A review on buildings energy consumption information. *Energy and Buildings*, 40(3):394–398, 2008.

[27] Mattheos Santamouris and Dionysia Kolokotsa. On the impact of urban overheating and extreme climatic conditions on housing, energy, comfort and environmental quality of vulnerable population in europe. *Energy and Buildings*, 98:125–133, 2015.

[28] János M. Beér. High efficiency electric power generation: The environmental role. *Progress in Energy and Combustion Science*, 33(2):107–134, 2007.

[29] Sarada Kuravi, Jamie Trahan, D. Yogi Goswami, Muhammad M. Rahman, and Elias K. Stefanakos. Thermal energy storage technologies and systems for concentrating solar power plants. *Progress in Energy and Combustion Science*, 39(4):285–319, 2013.

[30] David Barlev, Ruxandra Vidu, and Pieter Stroeve. Innovation in concentrated solar power. *Solar Energy Materials and Solar Cells*, 95(10):2703–2725, 2011.

[31] Nenad Miljkovic, Ryan Enright, and Evelyn N. Wang. Effect of droplet morphology on growth dynamics and heat transfer during condensation on superhydrophobic nanostructured surfaces. *ACS Nano*, 6(2):1776–1785, 2012.

[32] Konrad Rykaczewski. Microdroplet growth mechanism during water condensation on superhydrophobic surfaces. *Langmuir*, 28(20):7720–7729, 2012.

[33] Nenad Miljkovic, Ryan Enright, and Evelyn N. Wang. Modeling and op-

timization of superhydrophobic condensation. *Journal of Heat Transfer*, 135(11):111004, 2013.

[34] Shreyas Chavan, Hyeongyun Cha, Daniel Orejon, Kashif Nawaz, Nitish Singla, Yip Fun Yeung, Deokgeun Park, Dong Hoon Kang, Yujin Chang, Yasuyuki Takata, et al. Heat transfer through a condensate droplet on hydrophobic and nanostructured superhydrophobic surfaces. *Langmuir*, 32(31):7774–7787, 2016.

[35] Sunwoo Kim and Kwang J. Kim. Dropwise condensation modeling suitable for superhydrophobic surfaces. *Journal of Heat Transfer*, 133(8):081502, 2011.

[36] Ryan Enright, Nenad Miljkovic, Nicholas Dou, Youngsuk Nam, and Evelyn N. Wang. Condensation on superhydrophobic copper oxide nanostructures. *Journal of Heat Transfer*, 135(9):091304, 2013.

[37] Xiuliang Liu and Ping Cheng. Dropwise condensation theory revisited: Part i. droplet nucleation radius. *International Journal of Heat and Mass Transfer*, 83:833–841, 2015.

[38] Xiuliang Liu and Ping Cheng. Dropwise condensation theory revisited part ii. droplet nucleation density and condensation heat flux. *International Journal of Heat and Mass Transfer*, 83:842–849, 2015.

[39] Hector Mendoza, Sara Beaini, and Van P. Carey. An exploration of transport within microdroplet and nanodroplet clusters during dropwise condensation of water on nanostructured surfaces. *Journal of Heat Transfer*, 136(12):121501, 2014.

[40] Aydin Umur and P. Griffith. Mechanism of dropwise condensation. *ASME J. Heat Transfer*, 87(2):275–282, 1965.

[41] Rongfu Wen, Zhong Lan, Benli Peng, Wei Xu, and Xuehu Ma. Droplet dynamics and heat transfer for dropwise condensation at lower and ultra-lower pressure. *Applied Thermal Engineering*, 88:265–273, 2015.

[42] Majid Ahmadlouydarab, Jalel Azaiez, and Zhangxin Chen. Dynamics of viscous liquid bridges inside microchannels subject to external oscillatory flow. *Physical Review E*, 91(2):023002, 2015.

[43] L. F. R. Espath, A. F. Sarmiento, P. Vignal, B. O. N. Varga, A. M. A. Cortes, L. Dalcin, and V. M. Calo. Energy exchange analysis in droplet dynamics via the navier–stokes–cahn–hilliard model. *Journal of Fluid Mechanics*, 797:389–430, 2016.

[44] David Jacqmin. Calculation of two-phase navier–stokes flows using phase-field modeling. *Journal of Computational Physics*, 155(1):96–127, 1999.

[45] David Jacqmin. Contact-line dynamics of a diffuse fluid interface. *Journal of Fluid Mechanics*, 402:57–88, 2000.

[46] J. Lowengrub and L. Truskinovsky. Quasi–incompressible cahn–hilliard fluids and topological transitions. In *Proceedings of the Royal Society of London A: Mathematical, Physical and Engineering Sciences*, volume 454, pages 2617–2654. The Royal Society, 1998.

[47] F. Magaletti, Francesco Picano, M. Chinappi, Luca Marino, and Carlo Massimo Casciola. The sharp-interface limit of the cahn–hilliard/navier–stokes model for binary fluids. *Journal of Fluid Mechanics*, 714:95–126, 2013.

[48] Pengtao Yue and James J. Feng. Wall energy relaxation in the cahn–hilliard model for moving contact lines. *Physics of Fluids*, 23(1):012106, 2011.

[49] P. Yue and J. J. Feng. Can diffuse-interface models quantitatively describe moving contact lines? *The European Physical Journal Special Topics*, 197(1):37–46, 2011.

[50] Jonathan B Boreyko and Chuan-Hua Chen. Self-propelled dropwise condensate on superhydrophobic surfaces. *Physical Review Letters*, 103(18):184501, 2009.

[51] Feng-Chao Wang, Fuqian Yang, and Ya-Pu Zhao. Size effect on the coalescence-induced self-propelled droplet. *Applied Physics Letters*, 98(5):053112, 2011.

[52] Cunjing Lv, Pengfei Hao, Zhaohui Yao, and Fenglei Niu. Departure of condensation droplets on superhydrophobic surfaces. *Langmuir*, 31(8):2414–2420, 2015.

[53] TQ Liu, W Sun, XY Sun, and HR Ai. Mechanism study of condensed drops jumping on super-hydrophobic surfaces. *Colloids and Surfaces A: Physicochemical and Engineering Aspects*, 414:366–374, 2012.

[54] Nenad Miljkovic, Ryan Enright, Youngsuk Nam, Ken Lopez, Nicholas Dou, Jean Sack, and Evelyn N. Wang. Jumping-droplet-enhanced condensation on scalable superhydrophobic nanostructured surfaces. *Nano Letters*, 13(1):179–187, 2012.

[55] Konrad Rykaczewski, Adam T. Paxson, Sushant Anand, Xuemei Chen, Zuankai Wang, and Kripa K. Varanasi. Multimode multidrop serial coalescence effects during condensation on hierarchical superhydrophobic surfaces. *Langmuir*, 29(3):881–891, 2013.

[56] Cunjing Lv, Pengfei Hao, Zhaohui Yao, Yu Song, Xiwen Zhang, and Feng He. Condensation and jumping relay of droplets on lotus leaf. *Applied Physics Letters*, 103(2):021601, 2013.

[57] Jonathan B. Boreyko and Chuan-Hua Chen. Vapor chambers with jumping-drop liquid return from superhydrophobic condensers. *International Journal of Heat and Mass Transfer*, 61:409–418, 2013.

[58] Youngsuk Nam, Hyunsik Kim, and Seungwon Shin. Energy and hydrodynamic analyses of coalescence-induced jumping droplets. *Applied Physics Letters*, 103(16):161601, 2013.

[59] Nenad Miljkovic, Daniel J Preston, Ryan Enright, and Evelyn N. Wang. Electrostatic charging of jumping droplets. *Nature Communications*, 4, 2013.

[60] Fangjie Liu, Giovanni Ghigliotti, James J. Feng, and Chuan-Hua Chen. Numerical simulations of self-propelled jumping upon drop coalescence on non-wetting surfaces. *Journal of Fluid Mechanics*, 752:39–65, 2014.

[61] Kosuke Yanagisawa, Munetoshi Sakai, Toshihiro Isobe, Sachiko Matsushita, and Akira Nakajima. Investigation of droplet jumping on superhydrophobic coatings during dew condensation by the observation from two directions. *Applied Surface Science*, 315:212–221, 2014.

[62] Nenad Miljkovic, Daniel J. Preston, Ryan Enright, and Evelyn N. Wang. Jumping-droplet electrostatic energy harvesting. *Applied Physics Letters*, 105(1):013111, 2014.

[63] Ryan Enright, Nenad Miljkovic, James Sprittles, Kevin Nolan, Robert Mitchell, and Evelyn N. Wang. How coalescing droplets jump. *ACS Nano*, 8(10):10352–10362, 2014.

[64] Kungang Zhang, Fangjie Liu, Adam J. Williams, Xiaopeng Qu, James J. Feng, and Chuan-Hua Chen. Self-propelled droplet removal from hydrophobic fiber-based coalescers. *Physical Review Letters*, 115(7):074502, 2015.

[65] Samaneh Farokhirad, Jeffrey F. Morris, and Taehun Lee. Coalescence-induced jumping of droplet: Inertia and viscosity effects. *Physics of Fluids*, 27(10):102102, 2015.

[66] Zhi Liang and Pawel Keblinski. Coalescence-induced jumping of nanoscale droplets on super-hydrophobic surfaces. *Applied Physics Letters*, 107(14):143105, 2015.

[67] Moon-Kyung Kim, Hyeongyun Cha, Patrick Birbarah, Shreyas Chavan, Chen Zhong, Yuehan Xu, and Nenad Miljkovic. Enhanced jumping-droplet departure. *Langmuir*, 31(49):13452–13466, 2015.

[68] Abulimiti Aili, Hongxia Li, Mohamed H. Alhosani, and TieJun Zhang. Unidirectional fast growth and forced jumping of stretched droplets on nanostructured microporous surfaces. *ACS Applied Materials & Interfaces*, 8(33):21776–21786, 2016.

[69] Andrea Cavalli, Daniel J. Preston, Evelyn Tio, David W. Martin, Nenad Miljkovic, Evelyn N. Wang, Francois Blanchette, and John W. M. Bush. Electrically induced drop detachment and ejection. *Physics of Fluids*, 28(2):022101, 2016.

[70] J. W. Rose and L. R. Glicksman. Dropwise condensationthe distribution of drop sizes. *International Journal of Heat and Mass Transfer*, 16(2):411–425, 1973.

[71] Amir Faghri and Yuwen Zhang. *Transport Phenomena in Multiphase Systems*. Academic Press, 2006.

[72] Robert W. Schrage. *A Theoretical Study of Interphase Mass Transfer*. Columbia University Press, 1953.

[73] Rudolf Marek. *Einfluß Thermokapillarer Konvektion und Inerter Gase beim Blasensieden in Unterkühlter Flüssigkeit.* PhD thesis, Technische Universität München, 1996.

[74] G. Fang and C. A. Ward. Temperature measured close to the interface of an evaporating liquid. *Physical Review E*, 59(1):417, 1999.

[75] G. Fang and C A. Ward. Examination of the statistical rate theory expression for liquid evaporation rates. *Physical Review E*, 59(1):441, 1999.

[76] CA Ward and G Fang. Expression for predicting liquid evaporation flux: Statistical rate theory approach. *Physical Review E*, 59(1):429, 1999.

[77] A. Røsjorde, S. Kjelstrup, D. Bedeaux, and B. Hafskjold. Nonequilibrium molecular dynamics simulations of steady-state heat and mass transport in condensation: Ii. transfer coefficients. *Journal of Colloid and Interface Science*, 240(1):355–364, 2001.

[78] A. Røsjorde, D. W. Fossmo, D. Bedeaux, S. Kjelstrup, and B. Hafskjold. Nonequilibrium molecular dynamics simulations of steady-state heat and mass transport in condensation: I. local equilibrium. *Journal of Colloid and Interface Science*, 232(1):178–185, 2000.

[79] Øivind Wilhelmsen, Thuat T. Trinh, Signe Kjelstrup, Titus S. van Erp, and Dick Bedeaux. Heat and mass transfer across interfaces in complex nanogeometries. *Physical Review Letters*, 114(6):065901, 2015.

[80] Øivind Wilhelmsen, Thuat T. Trinh, Signe Kjelstrup, and Dick Bedeaux. Influence of curvature on the transfer coefficients for evaporation and condensation of lennard-jones fluid from square-gradient theory and nonequilibrium molecular dynamics. *The Journal of Physical Chemistry C*, 119(15):8160–8173, 2015.

[81] L. D. Landau and E. M. Lifshitz. *Fluid Mechanics*. Pergamon Press Ltd., 1959.

[82] William M. Deen. *Analysis of Transport Phenomena*. Oxford University Press, 2 edition, 2012.

[83] D. Jou, J. Casas-Vázquez, and G. Lebon. *Extended Irreversible Thermodynamics*. Springer-Verlag New York, Inc., 1993.

[84] Y. L. Yao. *Irreversible Thermodynamics*. 1981.

[85] Daan Frenkel and Berend Smit. *Understanding Molecular Simulation: from Algorithms to Applications*. Academic Press, 2 edition, 2001.

[86] J. M. Haile. *Molecular Dynamics Simulation*. Wiley, New York, 1992.

[87] M. P. Allen and D. J. Tildesley. *Computer Simulations of Liquids*. Oxford University Press, 2001.

[88] Jean-Pierre Hansen and Ian R. McDonald. *Theory of Simple Liquids with Applications to Soft Matter*, volume 4. Elsevier, 2013.

[89] B Widom. Structure of interfaces from uniformity of the chemical potential. *Journal of Statistical Physics*, 19(6):563–574, 1978.

[90] Herman J C Berendsen, J P M van Postma, Wilfred F van Gunsteren, A R H J DiNola, and J R Haak. Molecular dynamics with coupling to an external bath. *The Journal of Chemical Physics*, 81(8):3684–3690, 1984.

[91] T Schneider and E Stoll. Molecular-dynamics study of a three-dimensional one-component model for distortive phase transitions. *Physical Review B*, 17(3):1302, 1978.

[92] Glenn J Martyna, Michael L Klein, and Mark Tuckerman. Nosé–hoover chains: The canonical ensemble via continuous dynamics. *The Journal of chemical physics*, 97(4):2635–2643, 1992.

[93] Grant S Heffelfinger and Frank van Swol. Diffusion in lennard-jones fluids using dual control volume grand canonical molecular dynamics simulation (dcv-gcmd). *The Journal of Chemical Physics*, 100(10):7548–7552, 1994.

[94] Gaurav Arya, Hsueh-Chia Chang, and Edward J Maginn. A critical comparison of equilibrium, non-equilibrium and boundary-driven molecular dynamics techniques for studying transport in microporous materials. *The Journal of Chemical Physics*, 115(17):8112–8124, 2001.

[95] Jie Zheng, Erin M Lennon, Heng-Kwong Tsao, Yu-Jane Sheng, and Shaoyi Jiang. Transport of a liquid water and methanol mixture through carbon nanotubes under a chemical potential gradient. *The Journal of chemical physics*, 122(21):214702, 2005.

[96] YJ Lü and M Chen. Oscillation of gas molecules in carbon nanotubes. *Nanotechnology*, 19(21):215707, 2008.

[97] T Mutat, J Adler, and M Sheintuch. Single species transport and self diffusion in wide single-walled carbon nanotubes. *The Journal of chemical physics*, 136(23):234902, 2012.

[98] José Rafael Bordin, José S Andrade Jr, Alexandre Diehl, and Marcia C Barbosa. Enhanced flow of core-softened fluids through narrow nanotubes. *The Journal of Chemical Physics*, 140(19):194504, 2014.

[99] Paul L Barclay and Jennifer R Lukes. Mass-flow-rate-controlled fluid flow in nanochannels by particle insertion and deletion. *Physical Review E*,

94(6):063303, 2016.

[100] Paul L Barclay and Jennifer R Lukes. Fluid-fluid interfacial mobility from random walks. *The Journal of Chemical Physics*, 147(24):244703, 2017.

[101] AP Khain, N BenMoshe, and A Pokrovsky. Factors determining the impact of aerosols on surface precipitation from clouds: An attempt at classification. *Journal of the Atmospheric Sciences*, 65(6):1721–1748, 2008.

[102] Daniel Rosenfeld, Ulrike Lohmann, Graciela B Raga, Colin D O'dowd, Markku Kulmala, Sandro Fuzzi, Anni Reissell, and Meinrat O Andreae. Flood or drought: How do aerosols affect precipitation? *Science*, 321(5894):1309–1313, 2008.

[103] Jiwen Fan, Yuan Wang, Daniel Rosenfeld, and Xiaohong Liu. Review of aerosol–cloud interactions: Mechanisms, significance, and challenges. *Journal of the Atmospheric Sciences*, 73(11):4221–4252, 2016.

[104] Chandan Sarangi, SN Tripathi, Shivam Tripathi, and Mary C Barth. Aerosol-cloud associations over gangetic basin during a typical monsoon depression event using wrf-chem simulation. *Journal of Geophysical Research: Atmospheres*, 120(20), 2015.

[105] Yongmei Zheng, Hao Bai, Zhongbing Huang, Xuelin Tian, Fu-Qiang Nie, Yong Zhao, Jin Zhai, and Lei Jiang. Directional water collection on wetted spider silk. *Nature*, 463(7281):640, 2010.

[106] Jie Ju, Hao Bai, Yongmei Zheng, Tianyi Zhao, Ruochen Fang, and Lei Jiang. A multi-structural and multi-functional integrated fog collection system in cactus. *Nature Communications*, 3:1247, 2012.

[107] FT Malik, RM Clement, DT Gethin, W Krawszik, and AR Parker. Nature's moisture harvesters: a comparative review. *Bioinspiration & Biomimetics*, 9(3):031002, 2014.

[108] Kyoo-Chul Park, Philseok Kim, Alison Grinthal, Neil He, David Fox, James C Weaver, and Joanna Aizenberg. Condensation on slippery asymmetric bumps. *Nature*, 531(7592):78, 2016.

[109] Holger F Bohn and Walter Federle. Insect aquaplaning: Nepenthes pitcher plants capture prey with the peristome, a fully wettable water-lubricated anisotropic surface. *Proceedings of the National Academy of Sciences*, 101(39):14138–14143, 2004.

[110] JW Rose. Dropwise condensation theory and experiment: a review. *Proceedings of the Institution of Mechanical Engineers, Part A: Journal of Power and Energy*, 216(2):115–128, 2002.

[111] Mussie Fessehaye, Sabah A Abdul-Wahab, Michael J Savage, Thomas Kohler, Tseggai Gherezghiher, and Hans Hurni. Fog-water collection for community use. *Renewable and Sustainable Energy Reviews*, 29:52–62, 2014.

[112] Ritwick Ghosh, Tapan K Ray, and Ranjan Ganguly. Cooling tower fog harvesting in power plants–a pilot study. *Energy*, 89:1018–1028, 2015.

[113] Donghyun Seo, Junghun Lee, Choongyeop Lee, and Youngsuk Nam. The effects of surface wettability on the fog and dew moisture harvesting performance on tubular surfaces. *Scientific Reports*, 6:24276, 2016.

[114] Jonathan B Boreyko and Chuan-Hua Chen. Vapor chambers with jumping-drop liquid return from superhydrophobic condensers. *International Journal of Heat and Mass Transfer*, 61:409–418, 2013.

162

[115] Nenad Miljkovic, Ryan Enright, Youngsuk Nam, Ken Lopez, Nicholas Dou, Jean Sack, and Evelyn N Wang. Jumping-droplet-enhanced condensation on scalable superhydrophobic nanostructured surfaces. *Nano Letters*, 13(1):179–187, 2012.

[116] Konrad Rykaczewski. Microdroplet growth mechanism during water condensation on superhydrophobic surfaces. *Langmuir*, 28(20):7720–7729, 2012.

[117] Nenad Miljkovic, Ryan Enright, and Evelyn N Wang. Effect of droplet morphology on growth dynamics and heat transfer during condensation on superhydrophobic nanostructured surfaces. *ACS Nano*, 6(2):1776–1785, 2012.

[118] Sunwoo Kim and Kwang J Kim. Dropwise condensation modeling suitable for superhydrophobic surfaces. *Journal of Heat Transfer*, 133(8):081502, 2011.

[119] Sangsoo Lee, Hyung Kee Yoon, Kwang J Kim, Sunwoo Kim, Mike Kennedy, and Bong June Zhang. A dropwise condensation model using a nano-scale, pin structured surface. *International Journal of Heat and Mass Transfer*, 60:664–671, 2013.

[120] Jie Zhu, Yuting Luo, Jian Tian, Juan Li, and Xuefeng Gao. Clustered ribbed-nanoneedle structured copper surfaces with high-efficiency dropwise condensation heat transfer performance. *ACS Applied Materials & Interfaces*, 7(20):10660–10665, 2015.

[121] Xuehu Ma, Jiabin Chen, Dunqi Xu, Jifang Lin, Chunsheng Ren, and Zhenhu Long. Influence of processing conditions of polymer film on dropwise condensation heat transfer. *International Journal of Heat and Mass Transfer*, 45(16):3405–3411, 2002.

[122] Aritra Ghosh, Sara Beaini, Bong June Zhang, Ranjan Ganguly, and Constantine M Megaridis. Enhancing dropwise condensation through bioinspired wettability patterning. *Langmuir*, 30(43):13103–13115, 2014.

[123] Pallab Sinha Mahapatra, Aritra Ghosh, Ranjan Ganguly, and Constantine M Megaridis. Key design and operating parameters for enhancing dropwise condensation through wettability patterning. *International Journal of Heat and Mass Transfer*, 92:877–883, 2016.

[124] Sushant Anand and Sang Young Son. Sub-micrometer dropwise condensation under superheated and rarefied vapor condition. *Langmuir*, 26(22):17100–17110, 2010.

[125] N Chodes, J Warner, and A Gagin. A determination of the condensation coefficient of water from the growth rate of small cloud droplets. *Journal of the Atmospheric Sciences*, 31(5):1351–1357, 1974.

[126] R Marek and J Straub. Analysis of the evaporation coefficient and the condensation coefficient of water. *International Journal of Heat and Mass Transfer*, 44(1):39–53, 2001.

[127] LJ Delaney, RW Houston, and LC Eagleton. The rate of vaporization of water and ice. *Chemical Engineering Science*, 19(2):105–114, 1964.

[128] Shigeo Fujikawa and Mehdi Maerefat. A study of the molecular mechanism of vapour condensation. *JSME International Journal. Ser. 2, Fluids Engineering, Heat Transfer, Power, Combustion, Thermophysical Properties*, 33(4):634–641, 1990.

[129] JC Bonacci, AL Myers, G Nongbri, and LC Eagleton. The evaporation and condensation coefficient of water, ice and carbon tetrachloride. *Chemical Engi-*

neering Science, 31(8):609–617, 1976.

[130] Zhi Liang and Pawel Keblinski. Molecular simulation of steady-state evaporation and condensation in the presence of a non-condensable gas. *The Journal of Chemical Physics*, 148(6):064708, 2018.

[131] James Gonzalez, Josue Ortega, and Zhi Liang. Prediction of thermal conductance at liquid-gas interfaces using molecular dynamics simulations. *International Journal of Heat and Mass Transfer*, 126:1183–1192, 2018.

[132] Akihiro Morita. Molecular dynamics study of mass accommodation of methanol at liquid–vapor interfaces of methanol/water binary solutions of various concentrations. *Chemical Physics Letters*, 375(1-2):1–8, 2003.

[133] Akihiro Morita, Masakazu Sugiyama, Hirofumi Kameda, Seiichiro Koda, and David R Hanson. Mass accommodation coefficient of water: Molecular dynamics simulation and revised analysis of droplet train/flow reactor experiment. *The Journal of Physical Chemistry B*, 108(26):9111–9120, 2004.

[134] Jan Julin, Manabu Shiraiwa, Rachael EH Miles, Jonathan P Reid, Ulrich Pöschl, and Ilona Riipinen. Mass accommodation of water: Bridging the gap between molecular dynamics simulations and kinetic condensation models. *The Journal of Physical Chemistry A*, 117(2):410–420, 2013.

[135] Takaharu Tsuruta and Gyoko Nagayama. A microscopic formulation of condensation coefficient and interface transport phenomena. *Energy*, 30(6):795–805, 2005.

[136] Bing-Yang Cao, Jian-Fei Xie, and Sergei S Sazhin. Molecular dynamics study on evaporation and condensation of n-dodecane at liquid–vapor phase equilibria. *The Journal of Chemical Physics*, 134(16):164309, 2011.

[137] Kenji Yasuoka, Mitsuhiro Matsumoto, and Yosuke Kataoka. Evaporation and condensation at a liquid surface. i. argon. *The Journal of Chemical Physics*, 101(9):7904–7911, 1994.

[138] Mitsuhiro Matsumoto, Kenji Yasuoka, and Yosuke Kataoka. Evaporation and condensation at a liquid surface. ii. methanol. *The Journal of Chemical Physics*, 101(9):7912–7917, 1994.

[139] Akihiro Morita. Molecular dynamics study of mass accommodation of methanol at liquid–vapor interfaces of methanol/water binary solutions of various concentrations. *Chemical Physics Letters*, 375(1-2):1–8, 2003.

[140] S Takahama and LM Russell. A molecular dynamics study of water mass accommodation on condensed phase water coated by fatty acid monolayers. *Journal of Geophysical Research: Atmospheres*, 116(D2), 2011.

[141] Richard C Tolman. The effect of droplet size on surface tension. *The Journal of Chemical Physics*, 17(3):333–337, 1949.

[142] SM Thompson, KE Gubbins, JPRB Walton, RAR Chantry, and JS Rowlinson. A molecular dynamics study of liquid drops. *The Journal of Chemical Physics*, 81(1):530–542, 1984.

[143] MJ Haye and C Bruin. Molecular dynamics study of the curvature correction to the surface tension. *The Journal of Chemical Physics*, 100(1):556–559, 1994.

[144] AE Van Giessen and EM Blokhuis. Determination of curvature corrections to the surface tension of a liquid–vapor interface through molecular dynamics simulations. *The Journal of Chemical Physics*, 116(1):302–310, 2002.

[145] Øivind Wilhelmsen, Dick Bedeaux, and David Reguera. Tolman length and

rigidity constants of the lennard-jones fluid. *The Journal of Chemical Physics*, 142(6):064706, 2015.

[146] Hisao Yaguchi, Takeru Yano, and Shigeo Fujikawa. Molecular dynamics study of vapor-liquid equilibrium state of an argon nanodroplet and its vapor. *Journal of Fluid Science and Technology*, 5(2):180–191, 2010.

[147] DJ Lee, MM Telo da Gama, and KE Gubbins. A microscopic theory for spherical interfaces: liquid drops in the canonical ensemble. *The Journal of Chemical Physics*, 85(1):490–499, 1986.

[148] Marcus G Martin and J Ilja Siepmann. Transferable potentials for phase equilibria. 1. united-atom description of n-alkanes. *The Journal of Physical Chemistry B*, 102(14):2569–2577, 1998.

[149] Bin Chen and J Ilja Siepmann. Transferable potentials for phase equilibria. 3. explicit-hydrogen description of normal alkanes. *The Journal of Physical Chemistry B*, 103(25):5370–5379, 1999.

[150] Neeraj Rai and J Ilja Siepmann. Transferable potentials for phase equilibria. 9. explicit hydrogen description of benzene and five-membered and six-membered heterocyclic aromatic compounds. *The Journal of Physical Chemistry B*, 111(36):10790–10799, 2007.

[151] Bin Chen, Jeffrey J Potoff, and J Ilja Siepmann. Monte carlo calculations for alcohols and their mixtures with alkanes. transferable potentials for phase equilibria. 5. united-atom description of primary, secondary, and tertiary alcohols. *The Journal of Physical Chemistry B*, 105(15):3093–3104, 2001.

[152] Jose LF Abascal and Carlos Vega. A general purpose model for the condensed phases of water: Tip4p/2005. *The Journal of Chemical Physics*, 123(23):234505,

2005.

[153] I Shvab and Richard J Sadus. Atomistic water models: Aqueous thermodynamic properties from ambient to supercritical conditions. *Fluid Phase Equilibria*, 407:7–30, 2016.

[154] Malte Fugel and Volker C Weiss. A corresponding-states analysis of the liquid-vapor equilibrium properties of common water models. *The Journal of Chemical Physics*, 146(6):064505, 2017.

[155] Hans C Andersen. Rattle: A velocity version of the shake algorithm for molecular dynamics calculations. *Journal of Computational Physics*, 52(1):24–34, 1983.

[156] Andrij Trokhymchuk and José Alejandre. Computer simulations of liquid/vapor interface in lennard-jones fluids: Some questions and answers. *The Journal of Chemical Physics*, 111(18):8510–8523, 1999.

[157] Florent Goujon, Patrice Malfreyt, Jean-Marc Simon, Anne Boutin, Bernard Rousseau, and Alain H Fuchs. Monte carlo versus molecular dynamics simulations in heterogeneous systems: An application to the n-pentane liquid-vapor interface. *The Journal of Chemical Physics*, 121(24):12559–12571, 2004.

[158] HA Lorentz. Ueber die anwendung des satzes vom virial in der kinetischen theorie der gase. *Annalen der Physik*, 248(1):127–136, 1881.

[159] Daniel Berthelot. Sur le mélange des gaz. *Compt. Rendus*, 126:1703–1706, 1898.

[160] WL Jorgensen, JD Madura, and CJ Swenson. Free radicals in lipid bilayers: new probes of lipid radical dynamics. *J. Am. Chem. Soc*, 106:813–814, 1984.

[161] D. A. Case, S. R. Brozell, D. S. Cerutti, T. E. Cheatham III, V.W.D. Cruzeiro, T.A. Darden, R.E. Duke, D. Ghoreishi, H. Gohlke, A.W. Goetz, D. Greene, R Harris, N. Homeyer, S. Izadi, A. Kovalenko, T.S. Lee, S. LeGrand, P. Li, C. Lin, J. Liu, T. Luchko, R. Luo, D.J. Mermelstein, K.M. Merz, Y. Miao, G. Monard, H. Nguyen, I. Omelyan, A. Onufriev, F. Pan, R. Qi, D.R. Roe, A. Roitberg, C. Sagui, S. Schott-Verdugo, J. Shen, C.L. Simmerling, J. Smith, J. Swails, R.C. Walker, J. Wang, H. Wei, R.M. Wolf, X. Wu, L. Xiao, D.M. York, and P.A. Kollman. *AMBER*. University of California, San Francisco, CA, 2018.

[162] Hisashi Okumura and Fumiko Yonezawa. Liquid–vapor coexistence curves of several interatomic model potentials. *The Journal of Chemical Physics*, 113(20):9162–9168, 2000.

[163] Jeffrey R Errington and Athanassios Z Panagiotopoulos. Phase equilibria of the modified buckingham exponential-6 potential from hamiltonian scaling grand canonical monte carlo. *The Journal of Chemical Physics*, 109(3):1093–1100, 1998.

[164] Van P Carey. *Liquid-vapor phase-change phenomena*. Hemisphere, New York, NY (United States), 1992.

[165] Michael P Allen and Dominic J Tildesley. *Computer simulation of liquids*. Oxford university press, 1987.

[166] John A Zollweg and George W Mulholland. On the law of the rectilinear diameter. *The Journal of Chemical Physics*, 57(3):1021–1025, 1972.

[167] Michael E Fisher. Correlation functions and the critical region of simple fluids. *Journal of Mathematical Physics*, 5(7):944–962, 1964.

[168] Benjamin Widom. Surface tension and molecular correlations near the critical point. *The Journal of Chemical Physics*, 43(11):3892–3897, 1965.

[169] William H Press. *Numerical recipes 3rd edition: The art of scientific computing.* Cambridge university press, 2007.

[170] Kenji Yasuoka and Mitsuhiro Matsumoto. Molecular dynamics of homogeneous nucleation in the vapor phase. i. lennard-jones fluid. *The Journal of Chemical Physics*, 109(19):8451–8462, 1998.

[171] Kenneth S Pitzer, David Z Lippmann, RF Curl Jr, Charles M Huggins, and Donald E Petersen. The volumetric and thermodynamic properties of fluids. ii. compressibility factor, vapor pressure and entropy of vaporization1. *Journal of the American Chemical Society*, 77(13):3433–3440, 1955.

[172] F. Magaletti, Francesco Picano, M. Chinappi, Luca Marino, and Carlo Massimo Casciola. The sharp-interface limit of the cahn–hilliard/navier–stokes model for binary fluids. *Journal of Fluid Mechanics*, 714:95–126, 2013.

[173] Hadi Mehrabian and James J Feng. Auto-ejection of liquid drops from capillary tubes. *Journal of Fluid Mechanics*, 752:670–692, 2014.

[174] Chun-Xia Zhao. Multiphase flow microfluidics for the production of single or multiple emulsions for drug delivery. *Advanced drug delivery reviews*, 65(11):1420–1446, 2013.

[175] Marilyn Rayner, Diana Marku, Madeleine Eriksson, Malin Sjöö, Petr Dejmek, and Marie Wahlgren. Biomass-based particles for the formulation of pickering type emulsions in food and topical applications. *Colloids and Surfaces A: Physicochemical and Engineering Aspects*, 458:48–62, 2014.

[176] Katrina M Wisdom, Jolanta A Watson, Xiaopeng Qu, Fangjie Liu, Gregory S Watson, and Chuan-Hua Chen. Self-cleaning of superhydrophobic surfaces by self-propelled jumping condensate. *Proceedings of the National Academy of Sciences*, 110(20):7992–7997, 2013.

[177] Robert A Hayes and BJ Feenstra. Video-speed electronic paper based on electrowetting. *Nature*, 425(6956):383, 2003.

[178] Frieder Mugele and Jean-Christophe Baret. Electrowetting: from basics to applications. *Journal of Physics: Condensed Matter*, 17(28):R705, 2005.

[179] Samaneh Farokhirad, Jeffrey F Morris, and Taehun Lee. Coalescence-induced jumping of droplet: Inertia and viscosity effects. *Physics of Fluids*, 27(10):102102, 2015.

[180] David Jacqmin. Contact-line dynamics of a diffuse fluid interface. *Journal of Fluid Mechanics*, 402:57–88, 2000.

[181] J. Lowengrub and L. Truskinovsky. Quasi–incompressible cahn–hilliard fluids and topological transitions. In *Proceedings of the Royal Society of London A: Mathematical, Physical and Engineering Sciences*, volume 454, pages 2617–2654. The Royal Society, 1998.

[182] Fangjie Liu, Giovanni Ghigliotti, James J Feng, and Chuan-Hua Chen. Numerical simulations of self-propelled jumping upon drop coalescence on non-wetting surfaces. *Journal of Fluid Mechanics*, 752:39–65, 2014.

[183] Pengtao Yue, Chunfeng Zhou, and James J Feng. Sharp-interface limit of the cahn–hilliard model for moving contact lines. *Journal of Fluid Mechanics*, 645:279–294, 2010.

[184] Pengtao Yue and James J Feng. Wall energy relaxation in the cahn–hilliard model for moving contact lines. *Physics of Fluids*, 23(1):012106, 2011.

[185] Tiezheng Qian, Xiao-Ping Wang, and Ping Sheng. A variational approach to moving contact line hydrodynamics. *Journal of Fluid Mechanics*, 564:333–360, 2006.

[186] Jörn B Buhn, Philippe A Bopp, and Manfred J Hampe. Structural and dynamical properties of liquid–liquid interfaces: A systematic molecular dynamics study. *Journal of Molecular Liquids*, 125(2):187–196, 2006.

[187] Martin Lísal, Zbyšek Posel, and Pavel Izák. Air–liquid interfaces of imidazolium-based [tf 2 n-] ionic liquids: insight from molecular dynamics simulations. *Physical Chemistry Chemical Physics*, 14(15):5164–5177, 2012.

[188] P Ferraro, S Coppola, S Grilli, M Paturzo, and V Vespini. Dispensing nano-pico droplets and liquid patterning by pyroelectrodynamic shooting. *Nature nanotechnology*, 5(6):429–435, 2010.

[189] Zhi Liang and Pawel Keblinski. Coalescence-induced jumping of nanoscale droplets on super-hydrophobic surfaces. *Applied Physics Letters*, 107(14):143105, 2015.

[190] So/ren Toxvaerd and J Stecki. Density profiles at a planar liquid-liquid interface. *The Journal of Chemical Physics*, 102(18):7163–7168, 1995.

[191] J Stecki and Søren Toxvaerd. The liquid–liquid interface of simple liquids. *The Journal of Chemical Physics*, 103(10):4352–4359, 1995.

[192] Guillaume Galliero. Lennard-jones fluid-fluid interfaces under shear. *Physical Review E*, 81(5):056306, 2010.

172

[193] Mitsuhiro Matsumoto and Yosuke Kataoka. Study on liquid–vapor interface of water. i. simulational results of thermodynamic properties and orientational structure. *The Journal of Chemical Physics*, 88(5):3233–3245, 1988.

[194] MJP Nijmeijer, AF Bakker, C Bruin, and JH Sikkenk. A molecular dynamics simulation of the lennard-jones liquid–vapor interface. *The Journal of Chemical Physics*, 89(6):3789–3792, 1988.

[195] Andrij Trokhymchuk and José Alejandre. Computer simulations of liquid/vapor interface in lennard-jones fluids: Some questions and answers. *The Journal of Chemical Physics*, 111(18):8510–8523, 1999.

[196] VG Baidakov, GG Chernykh, and SP Protsenko. Effect of the cut-off radius of the intermolecular potential on phase equilibrium and surface tension in lennard–jones systems. *Chemical Physics Letters*, 321(3):315–320, 2000.

[197] Mitsuhiro Matsumoto and Kotaro Tanaka. Nano bubblesize dependence of surface tension and inside pressure. *Fluid Dynamics Research*, 40(7):546–553, 2008.

[198] Ian A Cosden and Jennifer R Lukes. Effect of cutoff radius on the surface tension of nanoscale bubbles. *Journal of Heat Transfer*, 133(10):101501, 2011.

[199] Pu Liu, Edward Harder, and BJ Berne. On the calculation of diffusion coefficients in confined fluids and interfaces with an application to the liquid- vapor interface of water. *The Journal of Physical Chemistry B*, 108(21):6595–6602, 2004.

[200] Michael A Wilson and Andrew Pohorille. Interaction of monovalent ions with the water liquid–vapor interface: A molecular dynamics study. *The Journal of Chemical Physics*, 95(8):6005–6013, 1991.

[201] Zachary T Trautt, Moneesh Upmanyu, and Alain Karma. Interface mobility from interface random walk. *Science*, 314(5799):632–635, 2006.

[202] David L Olmsted, Elizabeth A Holm, and Stephen M Foiles. Survey of computed grain boundary properties in face-centered cubic metalsii: Grain boundary mobility. *Acta Materialia*, 57(13):3704–3713, 2009.

[203] JJ Hoyt, ZT Trautt, and M Upmanyu. Fluctuations in molecular dynamics simulations. *Mathematics and Computers in Simulation*, 80(7):1382–1392, 2010.

[204] Steve Plimpton. Fast parallel algorithms for short-range molecular dynamics. *Journal of Computational Physics*, 117(1):1–19, 1995.

[205] LAMMPS. *http://lammps.sandia.gov/*. Sandia Corporation, 2013. Accessed on May 5, 2017.

[206] Thomas Werder, Jens H. Walther, and Petros Koumoutsakos. Hybrid atomistic–continuum method for the simulation of dense fluid flows. *Journal of Computational Physics*, 205(1):373–390, 2005.

[207] EM Kotsalis, Jens Honore Walther, and P Koumoutsakos. Control of density fluctuations in atomistic-continuum simulations of dense liquids. *Physical Review E*, 76(1):016709, 2007.

[208] KM Issa and P Poesio. Algorithm to enforce uniform density in liquid atomistic subdomains with specular boundaries. *Physical Review E*, 89(4):043307, 2014.

[209] John Towns, Timothy Cockerill, Maytal Dahan, Ian Foster, Kelly Gaither, Andrew Grimshaw, Victor Hazlewood, Scott Lathrop, Dave Lifka, Gregory D Peterson, et al. Xsede: accelerating scientific discovery. *Computing in Science & Engineering*, 16(5):62–74, 2014.

[210] In-Chul Yeh and Gerhard Hummer. System-size dependence of diffusion coefficients and viscosities from molecular dynamics simulations with periodic boundary conditions. *The Journal of Physical Chemistry B*, 108(40):15873–15879, 2004.

[211] Gota Kikugawa, Shotaro Ando, Jo Suzuki, Yoichi Naruke, Takeo Nakano, and Taku Ohara. Effect of the computational domain size and shape on the self-diffusion coefficient in a lennard-jones liquid. *The Journal of chemical physics*, 142(2):024503, 2015.

[212] Morton E Gurtin, Debra Polignone, and Jorge Vinals. Two-phase binary fluids and immiscible fluids described by an order parameter. *Mathematical Models and Methods in Applied Sciences*, 6(06):815–831, 1996.

[213] John W. Cahn and John E. Hilliard. Free energy of a nonuniform system. i. interfacial free energy. *The Journal of Chemical physics*, 28(2):258–267, 1958.

[214] JU Brackbill, Douglas B Kothe, and Charles Zemach. A continuum method for modeling surface tension. *Journal of computational physics*, 100(2):335–354, 1992.

[215] J Lowengrub and L Truskinovsky. Quasi–incompressible cahn–hilliard fluids and topological transitions. In *Proceedings of the Royal Society of London A: Mathematical, Physical and Engineering Sciences*, volume 454, pages 2617–2654. The Royal Society, 1998.

[216] David Jacqmin. Calculation of two-phase navier–stokes flows using phase-field modeling. *Journal of Computational Physics*, 155(1):96–127, 1999.

[217] Junseok Kim. A continuous surface tension force formulation for diffuse-interface models. *Journal of Computational Physics*, 204(2):784–804, 2005.

[218] Yavuz Ugurlu and Doğan Kaya. Solutions of the cahn–hilliard equation. *Computers & Mathematics with Applications*, 56(12):3038–3045, 2008.

[219] Wei Li, Huizhang Yang, and Bin He. Exact solutions of fractional burgers and cahn-hilliard equations using extended fractional riccati expansion method. *Mathematical Problems in Engineering*, 2014, 2014.

[220] J Karl Johnson, John A Zollweg, and Keith E Gubbins. The lennard-jones equation of state revisited. *Molecular Physics*, 78(3):591–618, 1993.

[221] JJ Nicolas, KE Gubbins, WB Streett, and DJ Tildesley. Equation of state for the lennard-jones fluid. *Molecular Physics*, 37(5):1429–1454, 1979.

[222] Florian Müller-Plathe. Reversing the perturbation in nonequilibrium molecular dynamics: An easy way to calculate the shear viscosity of fluids. *Physical Review E*, 59(5):4894, 1999.

[223] Peter Wirnsberger, Daniel Frenkel, and C Dellago. An enhanced version of the heat exchange algorithm with excellent energy conservation properties. *The Journal of chemical physics*, 143(12):124104, 2015.

[224] Jennifer R Lukes, DY Li, X-G Liang, and C-L Tien. Molecular dynamics study of solid thin-film thermal conductivity. *Journal of Heat Transfer*, 122(3):536–543, 2000.

[225] Henry G Weller, Gavin Tabor, Hrvoje Jasak, and Christer Fureby. A tensorial approach to computational continuum mechanics using object-oriented techniques. *Computers in physics*, 12(6):620–631, 1998.

[226] Henry G Weller, Chris Greenshields, and Cristel de Rouvray. Openfoam: The openfoam foundation, 2018.

[227] Wolfram Research, Inc. Mathematica, Version 11.3. Champaign, IL, 2018.

[228] S Kjelstrup, T Tsuruta, and D Bedeaux. The inverted temperature profile across a vapor/liquid surface analyzed by molecular computer simulations. *Journal of colloid and interface science*, 256(2):451–461, 2002.

[229] J Xu, S Kjelstrup, D Bedeaux, A Røsjorde, and L Rekvig. Verification of onsager's reciprocal relations for evaporation and condensation using non-equilibrium molecular dynamics. *Journal of colloid and interface science*, 299(1):452–463, 2006.

[230] Patrick Varilly and David Chandler. Water evaporation: A transition path sampling study. *The Journal of Physical Chemistry B*, 117(5):1419–1428, 2013.

[231] Dick Bedeaux, Signe Kjelstrup, and Hans Christian Öttinger. On a possible difference between the barycentric velocity and the velocity that gives translational momentum in fluids. *Physica A: Statistical Mechanics and its Applications*, 371(2):177–187, 2006.

[232] KS Glavatskiy and Dick Bedeaux. Resistances for heat and mass transfer through a liquid–vapor interface in a binary mixture. *The Journal of chemical physics*, 133(23):234501, 2010.

[233] JW Cipolla Jr, H Lang, and SK Loyalka. Kinetic theory of condensation and evaporation. ii. *The Journal of Chemical Physics*, 61(1):69–77, 1974.

[234] D Bedeaux, LJF Hermans, and T Ytrehus. Slow evaporation and condensation. *Physica A: Statistical Mechanics and its Applications*, 169(2):263–280, 1990.

[235] D Bedeaux and S Kjelstrup. Transfer coefficients for evaporation. *Physica A: Statistical Mechanics and its Applications*, 270(3-4):413–426, 1999.

[236] Luis G MacDowell, Peter Virnau, Marcus Müller, and Kurt Binder. The evaporation/condensation transition of liquid droplets. *The Journal of chemical physics*, 120(11):5293–5308, 2004.

[237] Benjamin J Block, Subir K Das, Martin Oettel, Peter Virnau, and Kurt Binder. Curvature dependence of surface free energy of liquid drops and bubbles: A simulation study. *The Journal of chemical physics*, 133(15):154702, 2010.

[238] Kurt Binder, Benjamin J Block, Peter Virnau, and Andreas Tröster. Beyond the van der waals loop: What can be learned from simulating lennard-jones fluids inside the region of phase coexistence. *American Journal of Physics*, 80(12):1099–1109, 2012.

[239] A Tröster, M Oettel, B Block, P Virnau, and K Binder. Numerical approaches to determine the interface tension of curved interfaces from free energy calculations. *The Journal of Chemical Physics*, 136(6):064709, 2012.

[240] Jelan Kuhn, Robert Stemmer, Freek Kapteijn, Signe Kjelstrup, and Joachim Gross. A non-equilibrium thermodynamics approach to model mass and heat transport for water pervaporation through a zeolite membrane. *Journal of Membrane Science*, 330(1-2):388–398, 2009.

[241] R Delgado-Buscalioni and PV Coveney. Usher: an algorithm for particle insertion in dense fluids. *The Journal of chemical physics*, 119(2):978–987, 2003.

[242] Matthew K Borg, Duncan A Lockerby, and Jason M Reese. The fade mass-stat: a technique for inserting or deleting particles in molecular dynamics simulations. *The Journal of chemical physics*, 140(7):074110, 2014.

[243] Yixiang Liao and Dirk Lucas. Possibilities and limitations of cfd simulation for flashing flow scenarios in nuclear applications. *Energies*, 10(1):139, 2017.

[244] Dalton Bertoldi, Caio CS Dallalba, and Jader R Barbosa Jr. Experimental investigation of two-phase flashing flows of a binary mixture of infinite relative volatility in a venturi tube. *Experimental Thermal and Fluid Science*, 64:152–163, 2015.

[245] Takashi Furusawa and Satoru Yamamoto. Mathematical modeling and computation of high-pressure steam condensation in a transonic flow. *Journal of Fluid Science and Technology*, 12(1):JFST0002–JFST0002, 2017.

[246] Ki-Hyun Kim, Ehsanul Kabir, and Shamin Kabir. A review on the human health impact of airborne particulate matter. *Environment international*, 74:136–143, 2015.

[247] PK Bansal and C Yang. Reverse heat transfer and re-condensation phenomena in non-adiabatic capillary tubes. *Applied Thermal Engineering*, 25(17-18):3187–3202, 2005.

[248] Barbara E Wyslouzil and Judith Wölk. Overview: Homogeneous nucleation from the vapor phasethe experimental science. *The Journal of Chemical Physics*, 145(21):211702, 2016.

[249] Markku Kulmala, Ilona Riipinen, Mikko Sipilä, Hanna E Manninen, Tuukka Petäjä, Heikki Junninen, Miikka Dal Maso, Genrik Mordas, Aadu Mirme, Marko Vana, et al. Toward direct measurement of atmospheric nucleation. *Science*, 318(5847):89–92, 2007.

[250] Md Sarwar Alam and Ji Hwan Jeong. Molecular dynamics simulations on homogeneous condensation of r600a refrigerant. *Journal of Molecular Liquids*, 261:492–502, 2018.

[251] Jung-In Yoon, Ho-Saeng Lee, Kwang-Bae Lee, Jae-Dol Kim, and Pradeep Bansal. Condensing heat transfer characteristics of hydrocarbon refrigerants in 9.52 and 12.7 mm smooth tube. *Heat and mass transfer*, 42(2):144–149, 2005.

[252] Nae-Hyun Kim. Application of the natural refrigerant mixture r-290/dme to a soft ice cream refrigerator. *International Journal of Air-Conditioning and Refrigeration*, 24(04):1650027, 2016.

[253] Mohammad Sultan Mahmud, Keishi Kariya, and Akio Miyara. Local condensation heat transfer characteristics of refrigerant r1234ze (e) flow inside a plate heat exchanger. *International Journal of Air-Conditioning and Refrigeration*, 25(01):1750004, 2017.

[254] Ho-Saeng Lee, Jung-In Yoon, Jae-Dol Kim, and PK Bansal. Characteristics of condensing and evaporating heat transfer using hydrocarbon refrigerants. *Applied thermal engineering*, 26(10):1054–1062, 2006.

[255] Claudio Lettieri, Derek Paxson, Zoltan Spakovszky, and Peter Bryanston-Cross. Characterization of nonequilibrium condensation of supercritical carbon dioxide in a de laval nozzle. *Journal of Engineering for Gas Turbines and Power*, 140(4):041701, 2018.